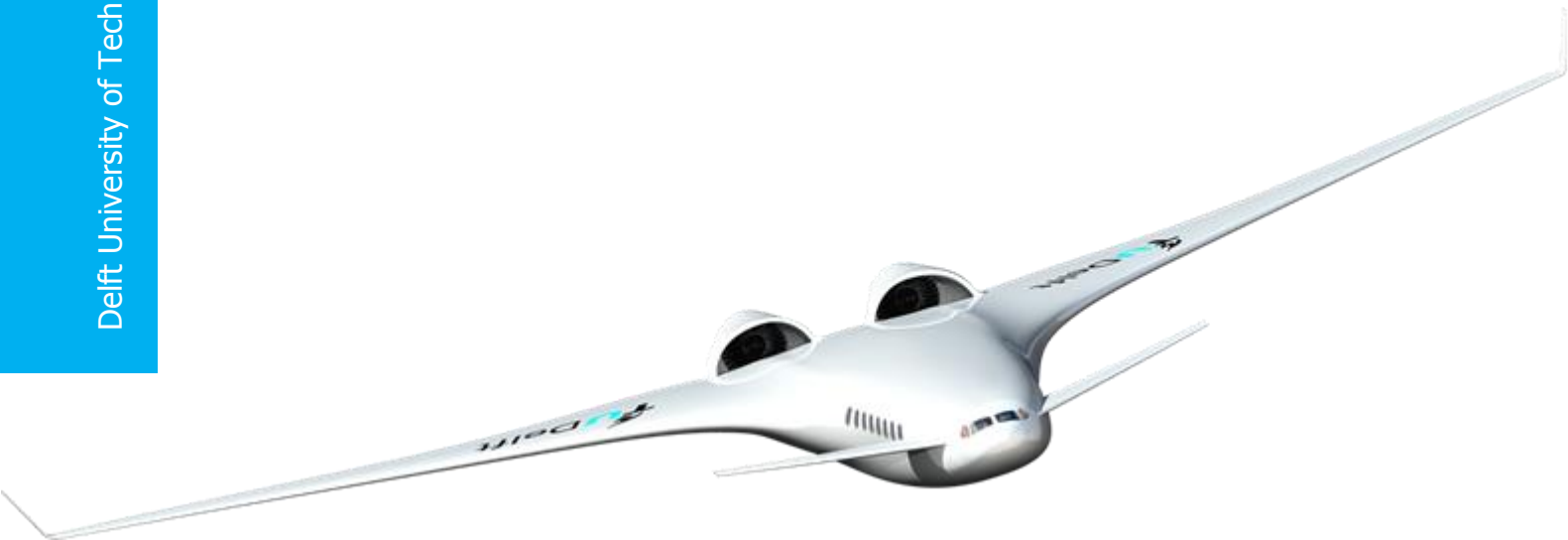


Design of Inlet for Boundary Layer Ingestion in a Blended Wing Body Aircraft

Design and computational analysis of a boundary layer ingesting inlet configuration for an embedded engine on a blended wing body aircraft

Abhishek Sharma

Delft University of Technology



Design of Inlet for Boundary Layer Ingestion in a Blended Wing Body Aircraft

By

Abhishek Sharma

in partial fulfilment of the requirements for the degree of

Master of Science
in Aerospace Engineering

at the Delft University of Technology,
to be defended publicly on Thursday January 29, 2015 at 14:00 PM.

Supervisor:	Dr. Arvind G. Rao	TU Delft
Thesis committee:	Prof. Dr. Ir. Leo Veldhuis,	TU Delft
	Dr. Daniele Ragini,	TU Delft
	Dr. Abhishek Bhat,	TU Delft

This thesis is confidential and cannot be made public until January 29, 2015.

Thesis Registration Number: 020#15#MT#FPP

An electronic version of this thesis is available at <http://repository.tudelft.nl/>.



Summary

Boundary Layer Ingestion (BLI) is a concept in which the fuselage boundary layer is ingested by the engine to produce benefits like improved fuel efficiency, reduction of ram drag and lower structural weight of the configuration. Blended Wing Body (BWB) concept has been researched on and studied in various forms over the years as an efficient alternative to the conventional transport configurations. Past studies have concluded that of the podded and embedded engine configurations, the BWB architecture is particularly suited to flush mounted embedded engines, as the balance requirements already place them near the aft of the airframe. Despite the benefits, effect of BLI on engine performance is also known to be detrimental because BLI increases pressure distortion and reduces total pressure recovery at the engine fan face. Most of these drawbacks are caused by secondary flow losses (vortices created due to boundary layer separation) due to an adverse pressure gradient in the S-Duct and a non-uniform mass flow ratio. An improved inlet design becomes necessary to reduce these limitations.

The aim of this research is to design an inlet embedded on a BWB that ingests significant amount of fuselage boundary layer and produces minimum pressure loss and distortion in the process. Two major consequences of BLI are vital in this regard namely, loss of total pressure recovery and increased total pressure distortion at the Aerodynamic Interface Plane (AIP) or the engine fan-face. Hence the inlet performance is measured by the total Pressure Recovery Factor (PRF) and Distortion Coefficient (DC_{60}). Therefore, this research work aims to design an embedded inlet on a BWB that produces maximum value of PRF and minimum DC_{60} .

An extensive literature study was carried out in order to understand the effects of BLI on inlet performance and research work conducted in the past to minimize the losses associated with BLI. Many of these studies focus on S-Ducts ingesting boundary layer and minimization of the losses using flow control techniques. Few studies have focussed on design of a novel inlet configuration that produces best results in terms of PRF and DC_{60} . This thesis has focussed on the design of the inlet based on computational analysis of different inlet configurations to achieve an optimum design.

The framework of this report first follows description of criteria and parameters for embedded inlet design. This is followed by an elaboration on the numerical methodology and approach to be used for the Computational Fluid Dynamics (CFD) simulations. The CFD simulations and analyses conducted in this thesis are divided into 2 main stages. The first stage deals with the computational analysis of a BWB in clean configuration (without engines) to obtain velocity profiles over aft fuselage, where the inlets will be embedded. The second stage comprises of the main inlet design. Three main geometrical parameters are chosen for the geometrical design of the inlet, namely inlet aspect ratio (ratio of inlet ellipse major axis length and semi-minor axis length), duct length and duct height. A number of tests are conducted to find out the influence of these parameters on the inlet performance. Few other inlet configurations are investigated, which can produce improved results and finally the design of the internal nacelle lip concludes the design of the inlet.

Since the BWB in this research operates at cruise conditions (at $M=0.82$), initially pressure losses were high. Testing of different inlet aspect ratios with constant length and height of

duct showed that an aspect ratio of 1.75 performs best with a PRF of 97.01% and a DC_{60} value of 41.59%, which was quite high. Further tests regarding variation in duct height showed most optimum results for the lowest height of duct due to reduced secondary flow losses. The duct with a height of 0.3m performed best with PRF=97.7% and DC_{60} =28.45%. Finally length of duct was varied keeping previously obtained aspect ratio and height and the shortest duct length (4.85m) performed best with PRF=97.7% and DC_{60} =28.45% (previous variations in duct height and aspect ratios were conducted using the same length value, hence the results for duct height are similar).

Therefore, the inlet obtained from the testing concluded the design as an S-Duct inlet with AR=1.75, L=4.85m and H=0.3m with PRF=97.7%, DC_{60} =28.45% and Mach number at the AIP as 0.6. After investigating other configurations like the reverse s-duct, double gradient duct, zero-gradient duct and zero-height duct, the zero-gradient duct (duct with flat bottom wall for boundary layer and no separation inside the inlet, L=4.85m, AR=1.75, H=1.615m) showed best results with PRF=98.04% and DC_{60} =20.55%. The internal nacelle was designed using a contraction ratio of 1.04 and a lip major-to-minor axis ratio (m/n) of 2. The final design of inlet was a zero-gradient duct with L=4.85m, AR=1.75, H=1.615m, CR=1.04, m/n=2, PRF=98.04%, DC_{60} =20.55% and Mach number at the AIP = 0.538. The same final design model was also tested using ParaPy (a high level Python language) and results showed a zero-gradient duct with L=4.85m, AR=1.75, H=1.615m, CR=1.04, m/n=2, PRF=98.3%, DC_{60} =20.14% and Mach number at the AIP = 0.539. A podded inlet configuration of L=6.46m and area-ratio=1.37 with same mass flow rate and fan-face Mach number as that of the embedded engine was also analysed to compare BLI case with no-BLI. The results showed a pressure loss of nearly 10% for the podded case and a larger wetted area. But the DC_{60} value was significantly lower (2.6%) in comparison to embedded inlet. Follow up studies can be conducted to improve the results using flow control techniques.

Acknowledgements

The thesis work presented in this report could not have been possible without the help of a number of people.

Firstly, I would like to extend my deepest gratitude to my thesis supervisor, Assistant Professor Dr. Arvind G. Rao, who helped me formulate the structure and plan of the thesis. In addition to this, he was instrumental in constantly motivating me and providing valuable feedback on my work and challenged me to pursue additional objectives, which backed the primary goals set up in this thesis.

I would like to thank Dr. Dipanjay Dewanji, my daily supervisor, who always helped and provided feedback on the smallest of issues regarding my thesis work. He played a vital role in helping me understand the techniques used in computational fluid dynamics (CFD) to obtain a variety of results. In the initial phase of the thesis when I was still learning about CFD concepts, he was supportive in sharing his knowledge about meshing and how to perform analysis of results.

Reinier Van Dijk played one of the most crucial roles in helping me in the first phase of the thesis. This phase required generation of several S-duct geometries and grids in order to understand the flow physics inside the ducts and the effects of grid and various geometrical parameters that affect duct design. It was not possible to create so many geometries individually in CATIA. A number of duct geometries and grids were constructed using his code written in ParaPy, a high level Python language developed by him for his PhD. Reinier was also very helpful in sharing his knowledge about the factors that affect mesh topology. I am grateful to him for his relentless support and time invested for my thesis work.

Finally, I would like to thank all my fellow master students, friends and my family for their unconditional support, motivation and encouragement, which kept me going and helped me remain patient and motivated.

*Abhishek Sharma
Delft, January 2015*

Contents

Summary	v
Acknowledgements	vii
Contents	ix
List of Figures	xiii
List of Tables	xvii
Nomenclature	xix
1. Introduction	1
1.1 Propulsion Airframe Integration (PAI)	2
1.2 Challenges in Embedded Engine Configuration	7
1.2.1 Distortion at Aerodynamic Interface Plane (AIP)	7
1.2.2 Secondary Flow in the S-Duct	8
1.2.3 Loss of Total Pressure Recovery	10
2. Research Goals and Objective	13
2.1 Research Question and Objective	13
2.2 Motivation	14
2.3 Scope	14
3. Background	15
3.1 Distributed Propulsion System	15
3.2 Studies Featuring Flow Control	17
3.2.1 Active Flow Control (AFC)	17
3.2.2 Passive Flow Control (PFC)	20
3.2.3 Hybrid Flow Control (HFC)	23
3.3 Other Research Work Concerning BLI	23
4. Existing Inlet Parameterization Examples	33
4.1 Nacelle Geometry Definition	33
4.2 Inlet Design Parameters	35
4.3 Design of Engine Inlet for JI5D-1	37
5. Parameterization, Numerical Modelling and Approach	39
5.1 Criteria for S-Duct Design	39
5.2 Parameters Affecting Duct Design	40
5.3 Parameterization of S-Duct	40
5.3.1 Main Geometrical Parameters for Inlet Design	40

5.3.2 Calculation of Area Ratio.....	44
5.4 Operating Conditions.....	45
5.5 Numerical Modelling: Governing Equations	46
5.5.1 Reynolds Averaged Navier-Stokes (RANS) equations.....	46
5.5.2 Turbulence Modelling	47
5.6 Mesh Topology.....	47
5.6.1 Factors Affecting Mesh Topology.....	47
5.6.2 Mesh Topology of the Tested Inlet Configurations	49
5.6.3 Boundary Conditions.....	51
5.6.4 Geometry and Mesh Generation using ParaPy.....	51
5.7 Testing Procedure	52
5.7.1 First Stage.....	53
5.7.2 Second Stage	54
5.7.3 Other Configurations Used For Testing	54
5.8 Validation	57
6. Results	61
6.1 Clean Blended Wing Body.....	61
6.2 Influence of Inlet Aspect Ratio and BLI	64
6.2.1 Total pressure and x-Velocity Results at AIP.....	66
6.2.2 Total Pressure Recovery at AIP	71
6.2.3 Distortion at AIP.....	72
6.3 Influence of Duct Height	73
6.4 Influence of Duct Length.....	75
6.5 Influence of Other Configurations.....	80
6.6 Results for Nacelle Lip.....	85
6.6.1 Final Inlet Design	87
6.6.2 Final Inlet Design using ParaPy	87
6.7 Results for Podded Inlet Configuration	89
6.8 Effect of BLI on Engine Performance.....	91
7. Conclusions and Recommendations	95
7.1 BLI Effect on Inlet Performance	95
7.2 Duct Height Effect on Inlet Performance	96
7.3 Duct Length Effect on Inlet Performance.....	96
7.4 Effect of Other Configurations and Internal Nacelle Lip.....	96

7.5 Podded Inlet Configuration	97
7.6 Limitations and Future Scope.....	97
References	99
APPENDIX – A	I
APPENDIX – B.....	III
APPENDIX – C	V
APPENDIX – D	VII
APPENDIX – E.....	IX
APPENDIX – F.....	XI
APPENDIX – G	XV

List of Figures

FIGURE 1: BWB WITH PYLON MOUNTED ENGINES [5]	2
FIGURE 2: INLET VELOCITY PROFILE IN AN EMBEDDED ENGINE CONFIGURATION [8].....	3
FIGURE 3: BENEFIT OF BLI: PODDED CASE V/s 100% BLI [8]	4
FIGURE 4: INLET VELOCITY PROFILE COMPARISON BETWEEN PODDED AND EMBEDDED ENGINES [5]	6
FIGURE 5: ADVANTAGES AND DISADVANTAGES OF EMBEDDED AND PODDED ENGINE PROPULSION SYSTEMS [8]	6
FIGURE 6: TOTAL PRESSURE DISTORTION AT THE ENGINE FAN FACE WITH ROTATING 60 DEG PART OF THE FAN FACE USED TO FIND DC ₆₀ [7] [12] 7	7
FIGURE 7: TYPICAL TOTAL PRESSURE CONTOURS AT AIP FOR S-DUCTS [13] [15]	8
FIGURE 8: PRESSURE CONTOURS AT AIP (LEFT) CAUSED DUE TO SECONDARY FLOW FORMATION (RIGHT) INSIDE THE S-DUCT [21] [22].....	9
FIGURE 9: SECONDARY FLOW VORTICES AT INLET AIRFRAME INTERSECTION [21].....	9
FIGURE 10: EFFECTS OF BLI AND PRESSURE RECOVERY ON NET THRUST [5]	11
FIGURE 11: BWB USING DISTRIBUTED PROPULSION WITH BLI [24]	15
FIGURE 12: EVALUATED PROPULSION SYSTEMS [24]	16
FIGURE 13: RESULTS OF OPTIMIZATION AS A FRACTION OF NON-BLI CONFIGURATION [24]	16
FIGURE 14: TOTAL PRESSURE RATIO CONTOUR PLOT WITHOUT FLOW CONTROL, DC ₆₀ = 29% [26]	17
FIGURE 15: TOTAL PRESSURE RATIO CONTOUR PLOT WITH AFC, DC ₆₀ = 4.6% [26].....	18
FIGURE 16: VARIATION OF CIRCUMFERENTIAL DISTORTION WITH CONTROL JET MASS FLOW RATIO USING AFC [13]	19
FIGURE 17: VARIATION OF TOTAL PRESSURE RECOVERY WITH CONTROL JET MASS FLOW RATIO USING AFC [13]	19
FIGURE 18: POTENTIAL FUEL SAVING BENEFIT OF BLI WITH AFC [5]	20
FIGURE 19: VG EFFECT ON INLET PERFORMANCE [11]	21
FIGURE 20: GRID SYSTEM FOR BLI AND VG'S [32].....	22
FIGURE 21: COMPARISON OF BASELINE AND PFC CASES [32]	22
FIGURE 22: TSFC BENEFIT FOR SEVERAL ARCHITECTURES COMPARED TO THEORETICAL LIMITS [4]	24
FIGURE 23: MESH AROUND THE AIRFOIL AND ENGINE [36]	24
FIGURE 24: MFR INFLUENCE ON LIFT COEFFICIENT [36]	25
FIGURE 25: BOUNDARY LAYER VELOCITY AND MACH NUMBER PROFILES AT INTAKE THROAT FOR DIFFERENT MFRs, M=0.73 [36]	25
FIGURE 26: MFR INFLUENCE ON TOTAL PRESSURE RECOVERY [36].....	26
FIGURE 27: MFR INFLUENCE ON DISTORTION COEFFICIENT [36].....	26
FIGURE 28: SETUP OF THE INLET DESIGN TOOL [14].....	28
FIGURE 29: DESIGN VARIABLES USED IN THE OPTIMIZATION FOR BWB [14]	28
FIGURE 30: PERFORMANCE RESULTS OF OPTIMIZATION [14]	29
FIGURE 31: COMPARISON OF PERFORMANCE PARAMETERS FOR BASELINE AND OPTIMIZED BWB CONFIGURATIONS [14]	30
FIGURE 32: COMPARISON OF PRESSURE CONTOURS FOR BWB NACELLES; BASELINE AND OPTIMIZED [14].....	30
FIGURE 33: PRESSURE CONTOURS AT AIP FOR BASELINE AND OPTIMIZED BWB CONFIGURATIONS [14]	30
FIGURE 34: NACELLE GEOMETRY DEFINITION [36].....	33
FIGURE 35: INLET AND DUCT DESIGN PARAMETERS [7]	35
FIGURE 35a: INLET SHAPES WITH VARYING Φ [7].....	36
FIGURE 36: MAJOR AXIS LENGTH ('A') AND SEMI-MINOR AXIS LENGTH ('B') FOR INLET FACE	41
FIGURE 37: DEFINITION OF LENGTH AND HEIGHT OF AN INLET CONFIGURATION	42
FIGURE 38: HIGHLIGHT AREA AND THROAT AREA AT UPSTREAM INLET	43
FIGURE 39: NACELLE LIP CONSTRUCTION	43
FIGURE 40: MESH TOPOLOGY AT THE INLET FACE	48
FIGURE 41: LAYERS IN THE STRUCTURED WALL REGION AT THE BOTTOM PART OF THE INLET FACE.....	49
FIGURE 42: MESH TOPOLOGY FOR AN INLET CONFIGURATION	49
FIGURE 43: FACTORS DEFINING MESH QUALITY [47]	50
FIGURE A: S-DUCT MODEL GENERATED USING PARAPY [50].....	49
FIGURE B: GRID GENERATED USING PARAPY [50].....	49
FIGURE 44: BWB IN CLEAN CONFIGURATION (WITHOUT ENGINES)	53
FIGURE 45: VELOCITY PROFILE APPLIED AS INLET TO S-DUCT.....	53
FIGURE 46: DIFFERENT CONFIGURATIONS USED FOR TESTING.....	55
FIGURE 47(A): FRAMEWORK FOR TESTING	56
FIGURE 47b: EFFECT OF %BLI ON PR AND DC(60) [8].....	57
FIGURE 47c: FLOW DEVELOPMENT INSIDE THE S-DUCT [8].....	58
FIGURE 47d: VARIATION OF PRESSURE RECOVERY WITH M [17].....	59

FIGURE 47e: VARIATION OF CIRCUMFERENTIAL DISTORTION DESCRIPTOR WITH M [17].....	59
FIGURE 47f: VARIATION OF DC(60) WITH ANGLE OF INCIDENCE [49]	59
FIGURE 47g: VARIATION OF DC(60) WITH THROAT M [49].....	60
FIGURE 48: 3D COMPUTATIONAL DOMAIN AROUND THE BWB WITH UNSTRUCTURED MESH	62
FIGURE 49: MESHED BWB AT THE SYMMETRY PLANE	62
FIGURE 50: MASS AND MOMENTUM RESIDUAL HISTORY FOR CLEAN BWB	63
FIGURE 51: VELOCITY DISTRIBUTION OVER BWB	63
FIGURE 52: VELOCITY PROFILE OVER AFT FUSELAGE OF CLEAN BWB	64
FIGURE 53: S-DUCT INLET FACES FOR DIFFERENT ASPECT RATIOS SHOWING BLI.....	65
FIGURE 54: VARIATION OF %BLI WITH INCREASING AR.....	65
FIGURE 55: TOTAL PRESSURE AND X-VELOCITY CONTOURS AT AIP FOR AR=1	66
FIGURE 56: TANGENTIAL FLOW AT THE AIP.....	66
FIGURE 57: STREAMLINES AT THE MID-PLANE FOR AR=1.....	67
FIGURE 58: MID-PLANE VIEW OF S-DUCT (AR=1) SHOWING RECIRCULATION REGION.....	68
FIGURE 59: MID-PLANE VIEW OF S-DUCT WITH AR=2.5 SHOWING RECIRCULATION REGION	68
FIGURE 60(A): TOTAL PRESSURE AND X-VELOCITY CONTOURS AT AIP FOR DIFFERENT INLET ASPECT RATIOS.....	70
FIGURE 60(B): VARIATION OF MACH NUMBER AT AIP FOR DIFFERENT ASPECT RATIOS.....	70
FIGURE 61: VARIATION OF PRESSURE RECOVERY WITH %BLI	71
FIGURE 62: VARIATION OF DC(60) WITH ASPECT RATIO	72
FIGURE 63: TOTAL PRESSURE AND X-VELOCITY CONTOURS AT AIP FOR VARIATION ON DUCT HEIGHT.....	74
FIGURE 64: VARIATION OF PRESSURE RECOVERY WITH DUCT HEIGHT	74
FIGURE 65: VARIATION OF DC(60) WITH DUCT HEIGHT.....	75
FIGURE 66: TOTAL PRESSURE AND X-VELOCITY CONTOURS AT AIP FOR VARIATION IN DUCT LENGTH	77
FIGURE 67: VARIATION OF DUCT WETTED AREA WITH DUCT LENGTH.....	77
FIGURE 68: VARIATION OF PRESSURE RECOVERY WITH DUCT LENGTH.....	78
FIGURE 69: MID PLANE VIEWS FOR INCREASING DUCT LENGTHS	78
FIGURE 70(A): VARIATION OF DC(60) WITH DUCT LENGTH	79
FIGURE 70(B): FLOW DEVELOPMENT INSIDE THE S-DUCT OBTAINED FROM TESTING GEOMETRICAL PARAMETERS.....	80
FIGURE 70(C): STREAMLINES INSIDE THE S-DUCT OBTAINED FROM TESTING GEOMETRICAL PARAMETERS.....	80
FIGURE 71: TOTAL PRESSURE AND X-VELOCITY CONTOURS AT AIP FOR DIFFERENT CONFIGURATIONS	82
FIGURE 72: PRESSURE RECOVERY FOR DIFFERENT INLET CONFIGURATIONS	82
FIGURE 73: DC(60) FOR DIFFERENT INLET CONFIGURATIONS	83
FIGURE 74: MID-PLANE VIEWS FOR DIFFERENT CONFIGURATIONS TO SHOW SEPARATION REGIONS.....	84
FIGURE 75: MACH NUMBER AT THE AIP FOR DIFFERENT CONFIGURATIONS	85
FIGURE 76: TOTAL PRESSURE AND X-VELOCITY CONTOURS AT AIP FOR CR=1.04, M/N=2 AND L=4.03M AND 4.85M.....	86
FIGURE 77: FINAL INLET DESIGN AR=1.75, L=4.85M, H=1.615M, CR=1.04, M/N=2, ZERO-PRESSURE GRADIENT FOR BOUNDARY LAYER, PR=98.04%, DC ₆₀ =20.55%	87
FIGURE C: FINAL DESIGN GRID GENERATED USING PARAPY.....	88
FIGURE D: COMPARISON OF INLET FACE MESH; PARAPY AND ICEM CFD.....	88
FIGURE E: TOTAL PRESSURE AND X-VELOCITY CONTOURS AT THE AIP FOR THE PARAPY MODEL (PR=98.3% AND DC ₆₀ =20.14%.....	88
FIGURE F: PODDED INLET CONFIGURATION (L=6.46M, AREA-RATIO = 1.37).....	89
FIGURE G: TOTAL PRESSURE AND X-VELOCITY CONTOURS AT AIP FOR PODDED INLET WITH L=6.46M, AREA-RATIO=1.37.....	90
FIGURE H: VARIATION OF SPECIFIC THRUST WITH INLET MACH NUMBER.....	91
FIGURE I: VARIATION OF SPECIFIC THRUST WITH PRESSURE RECOVERY FOR AN EMBEDDED ENGINE.....	92
FIGURE J: VARIATION OF SPECIFIC THRUST WITH PRESSURE RECOVERY FOR A PODDED ENGINE.....	92
FIGURE K: VARIATION OF TSFC WITH INLET MACH NUMBER.....	93
FIGURE L: VARIATION OF TSFC WITH PRESSURE RECOVERY FOR AN EMBEDDED ENGINE	93
FIGURE M: VARIATION OF TSFC WITH PRESSURE RECOVERY FOR A PODDED ENGINE.....	93
FIGURE 78: SEMI-ELLIPTICAL INLET FACE DIMENSIONS	III
FIGURE 79: SEPARATION AREAS INSIDE S-DUCTS WITH VARYING INLET ASPECT RATIO	V
FIGURE 80: SEPARATION AREAS INSIDE S-DUCTS WITH VARYING HEIGHT.....	VI
FIGURE 81: TOTAL PRESSURE CONTOURS AND THE 60 DEGREE SECTOR WITH LINES AT AIP	VII
FIGURE 82: GENERAL APPROACH FOR MODELLING OF A CFD CASE.....	IX
FIGURE 83: HISTOGRAM SHOWING MAX DIHEDRAL ANGLE VALUES FOR PARAPY GRID	XV
FIGURE 84: HISTOGRAM SHOWING MAX DIHEDRAL ANGLE VALUES FOR ICEM GRID.....	XV
FIGURE 85: HISTOGRAM SHOWING ASPECT RATIO VALUES FOR PARAPY GRID	XVI
FIGURE 86: HISTOGRAM SHOWING ASPECT RATIO VALUES FOR ICEM GRID.....	XVI
FIGURE 87: MINIMUM ANGLE DETERMINATION	XVII
FIGURE 88: HISTOGRAM SHOWING MINIMUM ANGLE VALUES FOR PARAPY GRID	XVII

FIGURE 89: HISTOGRAM SHOWING MINIMUM ANGLE VALUES FOR ICEM GRID XVII
FIGURE 90: PRISM THICKNESS DISTRIBUTION FOR PARAPY GRID XVIII
FIGURE 91: PRISM THICKNESS DISTRIBUTION FOR ICEM GRID XVIII
FIGURE 92: Y-PLUS DISTRIBUTION ON THE WALLS (PARAPY) XIX
FIGURE 93: Y-PLUS DISTRIBUTION ON THE WALLS (ICEM) XIX

List of Tables

TABLE 1: 'A' AND 'B' VALUES FOR DIFFERENT ASPECT RATIOS FOR AREA RATIO = 1.1.....	45
TABLE 2: VALUES OF GEOMETRICAL PARAMETERS FOR TESTING.....	45
TABLE 3: OPERATING CONDITIONS	45
TABLE 4: PRESSURE RECOVERY RESULTS FOR DIFFERENT CONTRACTION RATIOS FOR DOUBLE GRADIENT CASE.....	85
TABLE 5: PRESSURE RECOVERY AND MACH NUMBER RESULTS FOR ZERO-GRADIENT DUCT WITH LIP CR=1.04, L=4.03M AND 4.85M	86
TABLE 6: COMPARISON OF EMBEDDED AND PODDED INLETS.....	90
TABLE 7: OPERATING CONDITIONS	I

Nomenclature

Symbols	Description	Unit
DC_{60}	Distortion Coefficient	[-]
PRF (or PR)	Pressure Recovery Factor	[-]
M	Mach Number	[-]
AR	Inlet Aspect Ratio	[-]
L	Length of Duct	[m]
H	Height of Duct	[m]
CR	Contraction Ratio	[-]
Re	Reynold's Number	[-]
m	Semi-major axis length of lip ellipse	[m]
n	Semi-minor axis length of lip ellipse	[m]
a	Major axis length of elliptical inlet face	[m]
b	Semi-minor axis length of elliptical inlet face	[m]
F_{engine}	Engine Thrust	[N]
u_{∞}	Freestream Velocity	[m/s]
\dot{m}	Mass Flow Rate	[kg/s]
D_A	Airframe Drag	[N]
P	Power	[J]
u_j	Jet Velocity	[m/s]
u_w	Wake Velocity	[m/s]
q	Dynamic Pressure	[Pa]
P_m	Area averaged total pressure over entire fan face	[Pa]
$P_{t60\text{min}}$	Minimum area averaged total pressure over any 60 degree sector of the fan face	[Pa]
$C_{Pt,\text{loss}}$	Total pressure loss coefficient	[-]
D_{ing}	Drag Ingested	[N]
A_{th}	Throat Area	[m ²]
A_{hl}	Highlight Area	[m ²]
ρ	Density	[kg/m ³]
C_L	Lift Coefficient	[-]
C_m	Moment Coefficient	[-]
T	Thrust	[N]
MFR_{crit}	Critical Mass Flow Ratio	[-]
M_D	Drag Rise Mach Number	[-]
γ	Specific Heat Ratio	[-]
D_{fan}	Diameter of Engine Fan	[m]
A_F	Fan Area	[m ²]
k	Turbulent Kinetic Energy	[J/kg]
ε	Turbulent Dissipation Rate	[J/kgs]
μ	Dynamic Viscosity of Air	[Pa-s]
τ_w	Shear Stress	[N/m ²]
y^+	Non-dimensional Wall Distance	[-]

Abbreviations	Description
BLI	Boundary Layer Ingestion
BWB	Blended Wing Body
AIP	Aerodynamic Interface Plane
CFD	Computational Fluid Dynamics
PAI	Propulsion Airframe Integration
AFC	Active Flow Control
PFC	Passive Flow Control
HFC	Hybrid Flow Control
RANS	Reynold's Averaged Navier Stokes
MFR	Mass Flow Ratio
MDO	Multidisciplinary Design Optimization
TSFC	Thrust Specific Fuel Consumption
DPCP	Circumferential Distortion Descriptor
SST	Shear Stress Transport
AOA	Angle of Attack
NACA	National Advisory Committee for Aeronautics
VG	Vortex Generator
PR	Pressure Recovery
PRF	Pressure Recovery Factor
TSFC	Thrust Specific Fuel Consumption

1

Introduction

Energy efficiency and environmental compatibility are an important part of the modern aviation requirements. These requirements demand a novel configuration for air vehicles, which suggest highly integrated components for optimum overall performance. Improved propulsion system architectures are of primary importance in achieving these goals [1].

The life cycle cost of any vehicle depends on a number of factors of which fuel consumption is an important part. According to recent estimates, a 1% reduction in fuel burn can result in savings of \$1 million per engine per year. Apart from fuel consumption, noise plays an important role in the commercial engine business with growing tighter regulations. This causes curfews at airports, which increases the operational costs because of reduced capacity of airlines. Moreover, increment in harmful emissions has developed concerns over local air quality and global climate change, which give rise to stringent regulations [1] [2]. With regard to engines, fuel consumption, emissions, noise, drag and weight play vital roles in the overall aircraft performance. In addition to these, Propulsion Airframe Integration (PAI) is critical when it comes to meeting future aviation goals [1].

Hybrid wing-body has become increasingly popular according to recent airframe configuration studies. It suggests a highly integrated airframe configuration, which blurs the division between fuselage and wings. Blended Wing Body (BWB) is one such configuration, where mounting the propulsion system on the upper aft surface of the fuselage has the potential of producing significant benefits [1]. PAI on a BWB can be achieved either by podding the engines or embedding them on the fuselage. Podded engines ingest clean airflow, but have the disadvantages of increased weight, fuel burn and drag. This will be discussed later in detail. Embedding the engines on the fuselage implies ingestion of boundary layer. According to studies conducted in the domain of Boundary Layer Ingestion (BLI), it is well known that propulsive efficiency increases, if part or all of the propulsive fluid comes from the wake of the aircraft [3].

Boundary layer, which is ingested into the engines, consists of viscous losses which are developed as the boundary layer travels over the fuselage surface. Due to these losses, the inlet suffers a lower mass averaged stagnation pressure at the lip. Moreover, the ingestion of this wake momentum deficit also implies lower fuel burn rates [2] [4]. Therefore, BLI offers a way to achieve future commercial aviation goals, while promoting advancements in innovative engine technology. Chapter 1 focuses on the embedded and podded engine configurations with special emphasis on challenges faced when employing embedded engines. Chapter 2 presents an insight into past research on BLI and S-Duct performance. Chapter 3 looks into inlet and duct design and chapter 4 presents the current project's research plan, objective and timeline.

1.1 Propulsion Airframe Integration (PAI)

PAI is significant in achieving reduced emissions, noise and fuel burn, which are essential goals to meet future aviation demands. These demands can be met most effectively by a highly integrated vehicle of which PAI is a key factor for modern airplane design.

PAI on a BWB can be achieved in 2 ways, which are described in the following sub-sections:

a) *Podded engine configuration*

Podding the engines on aft fuselage is a well understood installation, airplane/engine performance for this type is proven and can be implemented using today's technology [5]. Fig 1 shows a typical podded engine configuration on a BWB with its advantages.

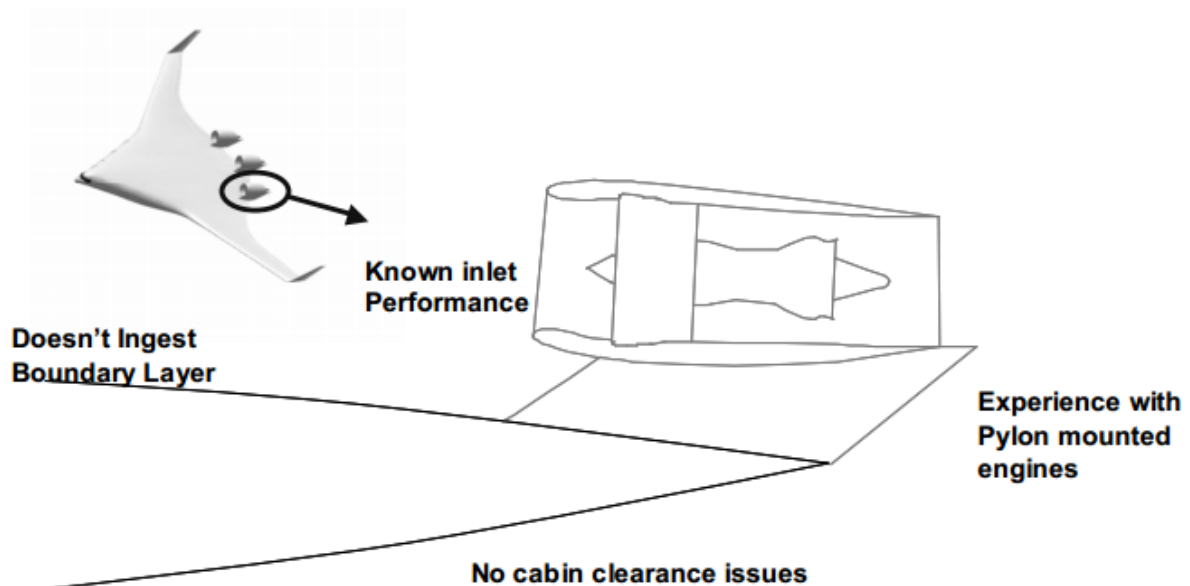


Figure 1: BWB with pylon mounted engines [5]

In this configuration, the engine ingests undisturbed airflow with high total pressure recovery and low distortion due to high uniformity in Mass Flow Ratio (MFR) and also because of the fact that there are no viscous losses like in the boundary layer. Pylon mounted engine configuration over the aft fuselage of a BWB shows the possibility of 32% fuel burn reduction compared to the conventional configurations (non-BWB aircrafts) [6].

However, due to higher momentum of the ingested flow, the ram drag is high in this configuration, which also increases the fuel burn. The use of pylon increases the structural weight and the wetted surface area thereby increasing profile drag. Furthermore, high noise due to unshielded intakes is also a major issue with pylon-mounted engines [7].

b) *Embedded engine configuration*

This configuration is ideally suited for a BWB due to balance requirements as described in the 'Introduction' section of this chapter. BLI can be achieved on a BWB only when the engines are buried on the fuselage surface. Because of the absence of pylons, this accounts for a reduced wetted surface area as well as structural weight. Furthermore, the thrust line is closer to the centreline in embedded engine configuration. This reduces nose down pitching moment, which is usually high in the podded engine configuration. This results in a direct trim drag benefit. In addition to this, embedded engines feature shielded intakes, which reduce overall noise production of the aircraft [8] [9].

Fig 2 shows the inlet velocity profile for an embedded engine configuration.

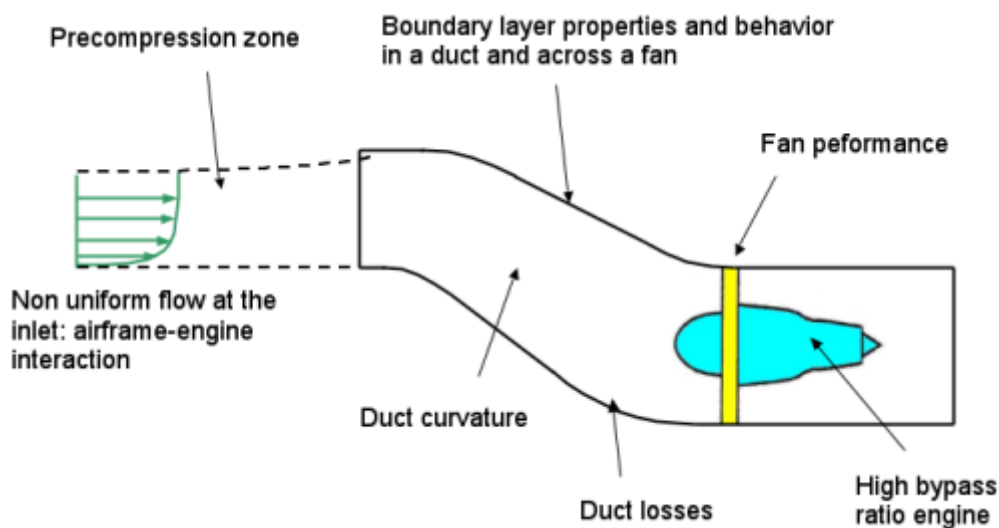


Figure 2: Inlet velocity profile in an embedded engine configuration [8]

One of the studies concerning the integration of embedded engines on BWB showed that using embedded inlets can increase the stall angle of BWB by about 2 degrees, so the curve of pitching moment coefficient can last long linearity region [10].

It has been shown by A. Plas [8] that power required to sustain the same drag force on the airframe with boundary layer ingestion is lesser than that with the podded engine configuration.

Fig 3 shows the power saving achieved through 100% BLI case as compared to the no-BLI one.

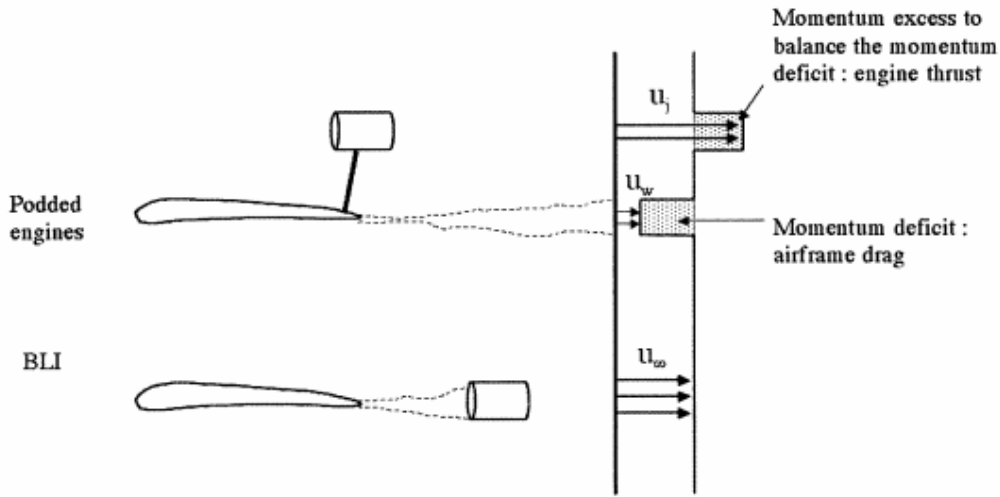


Figure 3: Benefit of BLI: Podded case V/s 100% BLI [8]

A. Plas [8] reasons that the benefit from BLI arises from re-energizing aircraft wake, thereby allowing lower energy waste. He shows this benefit mathematically using Fig 3. Free stream flow enters the inlet in the podded case with velocity, u_∞ . This velocity is accelerated by the engine to velocity, u_j . The resulting excess momentum created by podded engine balances the momentum deficit (due to airframe drag, D_A).

$$F_{engine} = \dot{m}(u_j - u_\infty) = \dot{m}(u_\infty - u_w) = D_A \quad (1.1)$$

Rate of mechanical energy, $P_{added, no-BLI}$ given by the engine to the flow is:

$$P_{added, no-BLI} = \frac{\dot{m}}{2}(u_j^2 - u_\infty^2) = \frac{F}{2}(u_j + u_\infty) \quad (1.2)$$

Useful power (power required for flight) is given as:

$$P_{useful} = D_A u_\infty = \dot{m}(u_j - u_\infty)u_\infty \quad (1.3)$$

Now, assume all of the boundary layer is ingested by the engine and the engine accelerates the wake back to free stream, the force provided by the engine is:

$$F_{engine} = \dot{m}(u_j - u_w) = \dot{m}(u_\infty - u_w) = D_A \quad (1.4)$$

So, for the 100% BLI case, the rate of energy $P_{added,BLI}$ given by the engine to the flow is given as:

$$P_{added,BLI} = \frac{\dot{m}}{2}(u_j^2 - u_w^2) = \frac{\dot{m}}{2}(u_\infty^2 - u_w^2) = \frac{F}{2}(u_w + u_\infty) \quad (1.5)$$

Useful power for 100% BLI case is same as that of podded engines:

$$P_{useful} = D_A u_\infty = \dot{m}(u_j - u_\infty)u_\infty \quad (1.6)$$

Since $u_j > u_w$, comparing equations (1.2) and (1.5) shows:

$$P_{added,no-BLI} > P_{added,BLI} \quad (1.7)$$

Equation (1.7) shows the power saving benefit of embedded engines with BLI.

However, there are several drawbacks for embedded engines. Firstly, the coupling between the airframe and the engines increases significantly, leading to a complex design process. Secondly, as seen in Fig 2, ingested airflow is non-uniform in embedded engines, which decreases engine performance. This non-uniformity is exaggerated by the S-Duct curvature, which has a pressure gradient. This pressure gradient produces secondary flow, which causes boundary layer separation. This ultimately leads to alternating pressure fields at the engine fan face, called the Aerodynamic Interface Plane (AIP), causing high distortion. Distortion at the AIP further leads to additional vibration and noise.

The non-uniformity of flow also leads to reduced total pressure recovery [8] [9]. Fig 4 shows both the podded and embedded engine configuration velocity profiles for a better understanding.

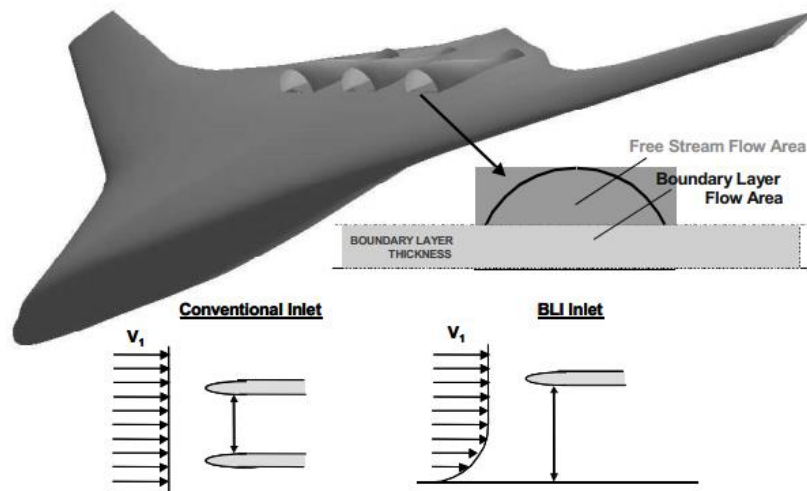


Figure 4: Inlet velocity profile comparison between podded and embedded engines [5]

A P. Plas [8] tabulated the advantages and disadvantages of the podded and embedded engine configurations to provide a clear view of the effects of these propulsion systems, which is shown in Fig 5.

	Podded engines	Embedded engines with BLI
Advantages	<ul style="list-style-type: none"> • Proven technology • Captures uniform flow 	<ul style="list-style-type: none"> • BLI → Fuel burn benefits • Liners and high BPR fans can be packaged more easily → Noise benefits • Nacelle wetted area savings • Weight savings • Lower thrust line
Drawbacks	<ul style="list-style-type: none"> • Larger wetted area • Larger structural weight (pylons and nacelles) • Pylon-airframe interference • High thrust line gives nose-down pitching moment 	<ul style="list-style-type: none"> • Non-uniform flow and S-duct → Possible degradation of inlet performance (separation, secondary flows) • Distortion at the fan face → vibration, noise? • Operability issues • More integrated design necessary • Unproven technology

Figure 5: Advantages and disadvantages of embedded and podded engine propulsion systems [8]

1.2 Challenges in Embedded Engine Configuration

The previous section presented a brief comparison between podded and embedded engines. As the present study focuses on the design of embedded engine inlets, this section presents a detailed study into the challenges faced when employing this particular configuration and the consequent BLI on a BWB.

There are 3 major problems that arise due to BLI on a BWB:

1. Distortion at AIP
2. Secondary flow in the S-Duct
3. Loss of total pressure recovery

1.2.1 Distortion at Aerodynamic Interface Plane (AIP)

Distortion at the engine fan face is one of the major causes of loss of engine efficiency on a BWB. The efficiency of a turbofan engine depends largely on clean and uniform airflow conditions. Due to BLI, there are several non-uniformities in pressure and inlet flow in the duct that affect engine performance. These flow and pressure non-uniformities lead to alternating pressure fields at the AIP. Consequently, the loading cycles of fan and compressor blades are more intense, which reduces the life cycle of engine components [7] [11].

The industry has set certain standards to keep the distortion levels within limits. Distortion Coefficient DC_{60} is one such standard and is defined as shown in Fig 6.

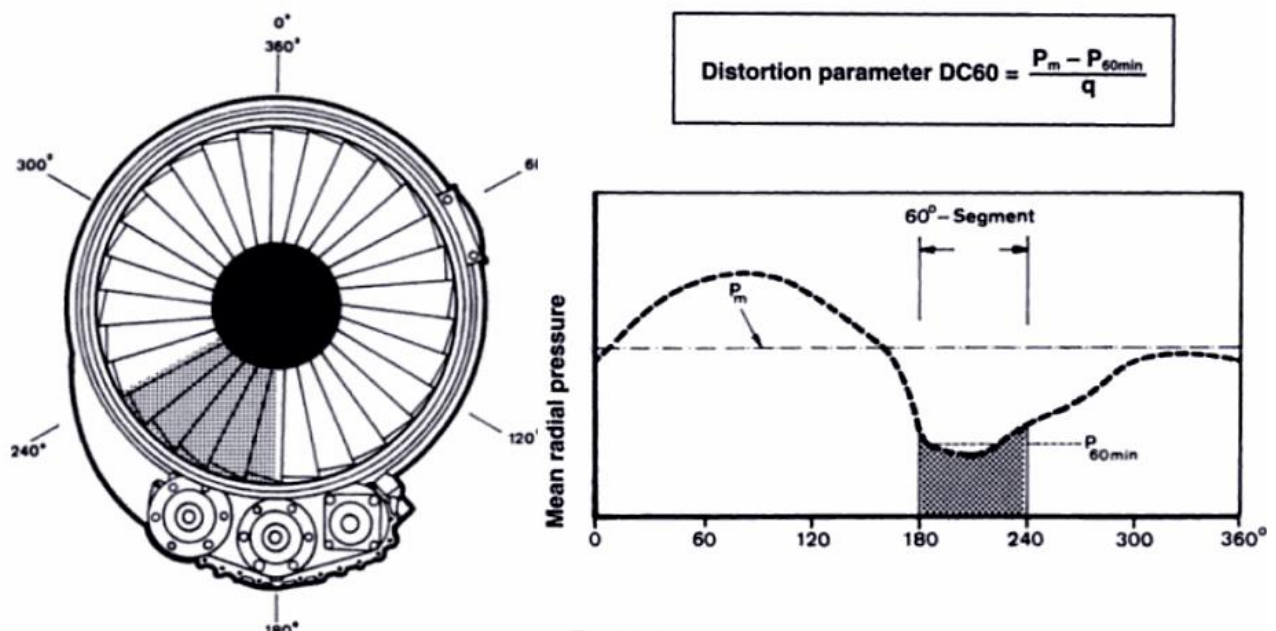


Figure 6: Total pressure distortion at the engine fan face with rotating 60 deg part of the fan face used to find DC_{60} [7] [12]

Here, Pd is the dynamic pressure (also written as q), Pm is the average total pressure over the fan face area and $P60min$ is the minimum area-averaged total pressure on any 60 deg sector of the fan face.

For civilian applications, acceptable levels of DC_{ϵ_0} occur below 0.1 and for military applications, it occurs below 0.2 [13].

Without Active Flow Control (AFC), DC_{ϵ_0} values of around 10% are possible to be obtained as demonstrated in some studies [11] [14]. However, further reduction of the distortion coefficient usually requires the use of flow control.

There are 2 categories of inlet distortion namely radial and circumferential distortion. Radial distortion signifies variations in total pressure across the blade span from root to tip. Circumferential distortion represents the variation of total pressure in the circumferential or angular direction. In a typical S-Duct, there are high and low total pressure regions that are distributed circumferentially about the AIP. This is shown in Fig 7, which presents typical total pressures at AIP for S-Ducts due to circumferential and radial distortion. Upper half of AIP shows high pressure regions due to uniform and undistorted flow. The lower half shows low pressure regions due to BLI [13] [15].

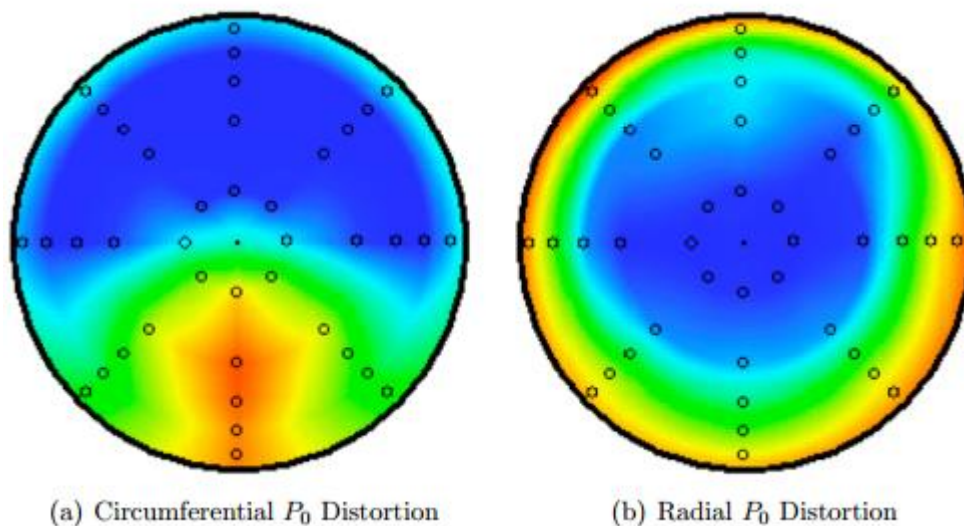


Figure 7: Typical total pressure contours at AIP for S-Ducts [13] [15]

1.2.2 Secondary Flow in the S-Duct

Due to the shape of the S-Duct, the flow entering the duct is highly distorted due to large vortex pair formation inside the duct. At the first bend, the flow accelerates, since the bottom part is turned away from the flow, which creates a local static pressure drop [16]. The boundary layer then becomes more prone to separation due to the resulting adverse pressure gradient.

After the flow exits the first bend, the pressure outside becomes higher than the pressure inside of the bend, hence the flow experiences a transverse pressure gradient. As a result of

this transverse pressure gradient, large accumulation of boundary layer takes places and the boundary layer is pulled towards the core flow. This large accumulation of boundary layer causes a lift-off effect and boundary layer separates forming 2 counter rotating vortices, which are pulled towards the core flow [17]. About 2% penalty in pressure recovery is demonstrated to be incurred because of this flow separation [17] [18] [19] [20]. Fig 8 shows the secondary flows inside the S-Duct and consequent pressure contours on the AIP.

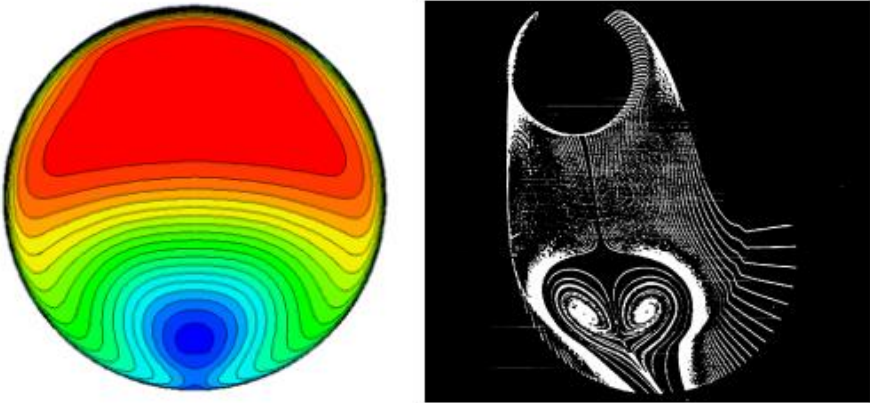


Figure 8: Pressure contours at AIP (left) caused due to secondary flow formation (right) inside the S-Duct [21] [22]

There are other causes of secondary flow formation within an S-Duct. The corners of the inlet face along the duct, where the duct lip meets the airframe surface, also experience secondary flow formation. The flow around the corners accelerates around the inlet lip, creating a horseshoe vortex [15]. This is shown in Fig 9.

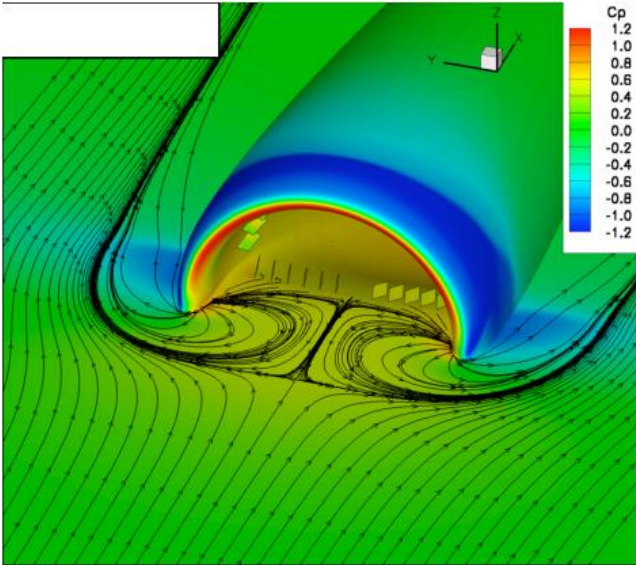


Figure 9: Secondary flow vortices at inlet airframe intersection [21]

1.2.3 Loss of Total Pressure Recovery

Another factor, which contributes largely to intake efficiency, is the Pressure Recovery Factor (PRF). This is defined by equation (1.8):

$$PRF = \frac{P_{t2}}{P_{t0}} \quad (1.8)$$

Here, P_{t2} represents total pressure at the AIP and P_{t0} is total pressure at the inlet.

The sum of dynamic pressure and static pressure gives total pressure. Intake ducts are designed in such a way so as to decrease the incoming velocity so that the fan experiences acceptable velocity value, otherwise flow separation can occur over the fan blades at high Mach numbers. Therefore, PRF is a measure of efficiency at which kinetic energy of the incoming flow is converted into pressure energy [12]. It is required to minimize losses and obtain a PRF as close to unity as possible by duct shaping.

Two major causes of losses are turbulent flow and skin friction. Hence, a short inlet duct is preferred, which provides smooth laminar boundary layer with minimum losses. In longer ducts, losses can be minimized by using flow control techniques. Vortex Generators (VG) are often used to minimize distortion levels, but does not really affect the pressure losses [19].

It is found that based on flight conditions and intake design, typically PRF is on the order of 90% to 98% [23]. However, current improved inlet designs have successfully achieved 99% PRF value.

However, it is known that ingesting airframe boundary layer results in average total pressure loss at the AIP [1]. At low Mach numbers, it is difficult to detect changes in total pressure loss for different flow conditions. Therefore, sometimes a non-dimensional total pressure loss coefficient is used to measure the pressure recovery performance at the fan. The more widely used PRF cancels out effect of small total pressure losses and low dynamic pressure at low speeds [11]. The total pressure loss coefficient is defined by equation (1.9):

$$C_{PtLoss} = \frac{P_{t\infty} - P_{tAvg}}{q_{\infty}} \quad (1.9)$$

Here, ∞ denotes wind tunnel free stream conditions and P_{tAvg} is area averaged total pressure at the fan face.

This pressure loss coefficient can also be converted to PRF corrected to $M=0.85$ using equation (2.0) [11]:

$$C_{PtLoss} \times \left(\frac{q_\infty}{P_{t\infty}}\right)_{M=0.85} = 1 - \left(\frac{P_{tAvg}}{P_{t\infty}}\right)_{M=0.85} \quad (2.0)$$

R. Kawai [5] showed the variation of pressure recovery with net thrust with BLI and a pressure loss coefficient value of 0.9981 using Active Flow Control (AFC) in Fig 10.

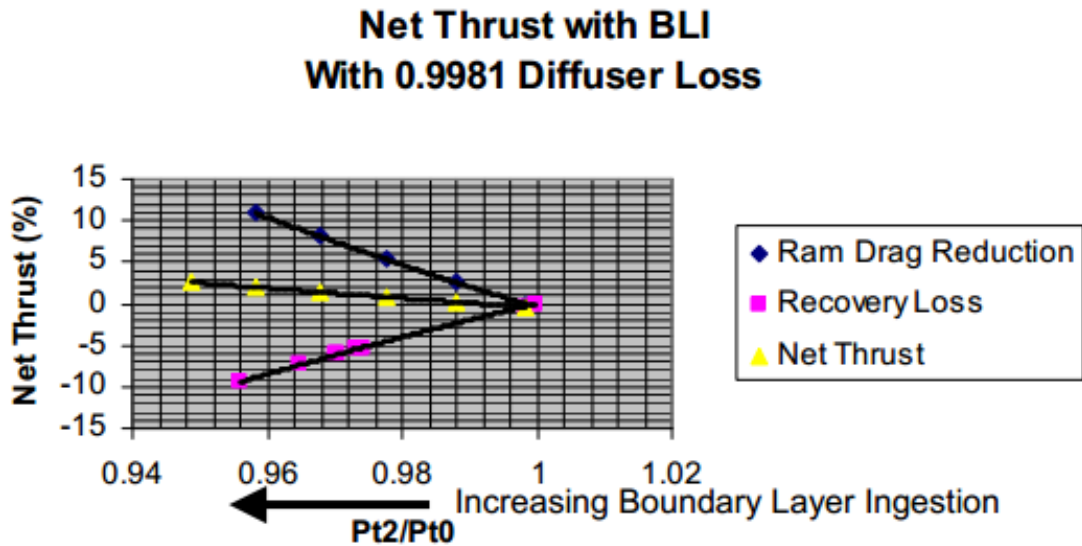


Figure 10: Effects of BLI and pressure recovery on net thrust [5]

R. Kawai shows that the total pressure recovery decreases with increasing BLI, whereas the distortion increases at the same time. Loss of total pressure recovery results in a loss of thrust. However, the decrease in ram drag reduction is greater than the loss in total pressure recovery, which shows the benefit of BLI (AFC was used in this case to minimize distortion).

2

Research Goals and Objective

This chapter explores the research objective, goals, motivation and scope of the thesis along with the success criteria.

2.1 Research Question and Objective

The main research question is twofold:

- How does BLI affect inlet performance on a BWB and which parameters are most significant in this regard?
- With BLI, which embedded inlet configuration/shape best minimizes total pressure distortion and maximizes total pressure recovery at the AIP?

The objective of the current thesis is “*to find an optimum inlet configuration embedded on a BWB, which produces minimum secondary flow losses and total pressure distortion at the AIP and maximum total pressure recovery*” using Computational Fluid Dynamics (CFD) as a tool.

The objective clearly signifies the **success criteria for this research as minimum total pressure distortion and maximum total pressure recovery**. To achieve this objective, there are a number of preliminary goals that need to be accomplished:

- Study how the inlet design parameters influence total pressure distortion and total pressure recovery at the AIP
- Study the flow physics inside the inlet with and without BLI
- Based on literature review, find out which inlet configurations meet the desired objective
- Obtain a novel inlet configuration that minimizes the losses associated with BLI

There are a number of sub-goals to achieve the aforementioned goals:

- Perform flow analysis on the given 3D BWB geometry
- Obtain inlet velocity profile over aft fuselage based on CFD analysis of clean configuration (without engines) of BWB
- Parameterize inlet configuration
- Create inlet geometries of varying shapes (different lengths, diameters, aspect ratios, etc.)
- Construct meshes for these geometries

- Perform CFD analyses on these inlet configurations using ANSYS CFX and obtain final results
- Select the geometry that achieves the research objective

These are just few of the many important questions that need to be addressed while pursuing the aforementioned objective. In addition to these questions, there are CFD related questions that need to be answered, for instance, the mesh configuration, size of domain, solver settings, etc.

2.2 Motivation

Based on the existing literature methods and results for embedded engine inlet performance and design, there are large number of developments in the domain of BLI on a BWB. The comparison of podded and embedded engine configurations still pose some questions regarding which configuration produces better results, but embedded engines with BLI still manage to show promising results for feasibility of this configuration.

However, tremendous improvements are required in the design for the inlets used in the embedded engines. An improved design can always be achieved so long as it is capable of achieving the desired research goals. In this case, these goals are simply to minimize losses like distortion and loss of pressure recovery in the engine. Most of the literature that exists sheds light on the effects of BLI, its feasibility and flow control techniques to improve performance; however few researchers have dedicated their research towards the design of inlets for embedded engine configuration on a BWB in order to minimize losses and strengthen PAI. With growing innovation in engine technology, improved designs are desired for maximizing performance and efficiency and for this purpose; the current thesis focuses on finding an optimum solution for the inlet design.

2.3 Scope

The current thesis work focuses only on the results obtained from the computational analysis of the inlet configurations ingesting fuselage boundary layer. No use of any kind of flow control is implemented in this project. The criteria and parameters affecting duct design are listed in the following chapters and only the most important and relevant criteria are chosen keeping in mind the timeframe within which the thesis had to be completed. Furthermore, the fan (AIP) is not modelled with a negative static pressure for suction, but is modelled as a circular plane with 0 Pa pressure using the pressure outlet boundary condition.

3

Background

This section consists of research work conducted in the past in the domain of embedded S-Duct engines and BWB performance and design. Many researchers have tested embedded engines on a BWB, both experimentally and computationally, to study their performance characteristics. These studies give a detailed insight into the benefits and shortcomings of BLI. Some of these studies also present different flow control techniques to minimize losses incurred to the engine performance due to BLI.

3.1 Distributed Propulsion System

H.J.M Kok et al [24] conducted a study to test the effect of incorporating different number of engines on a BWB on engine performance using numerical optimisation and a commercial software to test gas turbine performance, GSP. Fig 11 shows an example of a BWB featuring distributed propulsion system with BLI.



Figure 11: BWB using distributed propulsion with BLI [24]

This study was conducted for 2 values of pressure recovery, $\pi_{1-2} = 0.95$ and 0.97 , for incorporating 2% pressure loss resulting from S-Duct and increased pressure losses due to flattening of the intake in the other case, respectively.

Another important parameter for engine cycle calculations is the ingested drag, D_{ing} . This is explained by Lundbladh and Grondstedt [25] as “the momentum deficit in the air ingested by the propulsion system corresponding to part of the viscous drag of the aircraft.” Smith [5] proposed a parameter called the ingested drag fraction, $\frac{D_{ing}}{T}$, which is “a measure of the amount of ingested drag as a fraction of the net propulsive force.”

H.J.M Kok et al, from this study, obtained the following results, which are shown in Fig 12 and Fig 13:

Engines	3	3	4	4	8	8	12	12
D_{ing} / T	-	0.03	0.05	0.05	0.15	0.15	0.20	0.20
$\pi_{1,2}$	0.99	0.97	0.95	0.97	0.95	0.97	0.95	0.97

Figure 12: Evaluated propulsion systems [24]

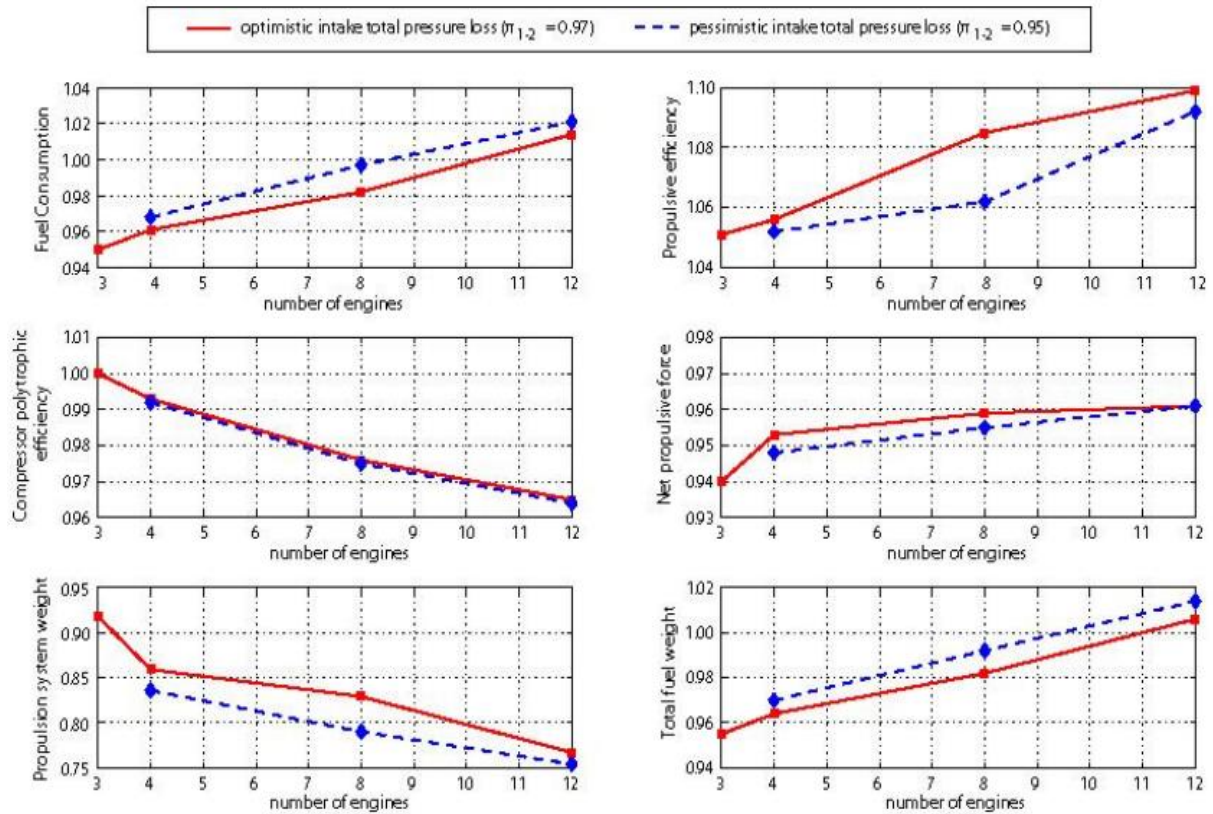


Figure 13: Results of optimization as a fraction of non-BLI configuration [24]

H.J.M Kok et al concluded that the distributed propulsion system configuration with larger number of engines (like 8 engines) shows around 2% benefit in fuel consumption over the conventional configuration, but this benefit is cancelled by the associated increase pressure loss. The 12 engine configuration did not show any fuel consumption benefit at all. The 3 engine configuration however, showed a 5% reduction in fuel consumption for a 2% increase in pressure loss.

It was concluded that the potential of BLI is better for larger engines than for smaller engines as the latter incur high losses in efficiency due to scale effects, which are larger when compared to the benefits of BLI. Furthermore, it was also concluded that distributed propulsion systems must be avoided and that the 3 engine embedded configuration shows the most promising results for overall performance.

3.2 Studies Featuring Flow Control

As described in Section 1.2, S-Duct embedded engine configuration on BWB faces 3 major challenges, namely distortion at AIP, loss of pressure recovery and secondary flow formation. These challenges must be overcome if the feasibility of embedded S-Duct engines has to be established. To achieve the goal of minimizing these losses, a number of studies in the past have focused on flow control techniques. These techniques employ flow control devices like Vortex Generators (VG), gas jets, fences, etc. in the inlet duct to manipulate the flow in a way so as to obtain acceptable flow characteristics at the AIP. This section focuses on such studies and their corresponding results.

3.2.1 Active Flow Control (AFC)

A large amount of literature exists on the feasibility of AFC in embedded S-Duct engines on a BWB and their use in minimizing secondary flow losses and distortion at the engine fan face.

One such study was carried out by Brian G. Allan et al [26]. This study assumes that employment of AFC can reduce the distortion level of the inlet to a level that allows acceptable engine operation. This embedded S-Duct engine with 30% BLI was tested in a wind tunnel at Nasa Langley. High mass flow pulsing actuators were used as the AFC device, which consisted of an electronically-controlled needle valve and the frequency could be controlled from 20Hz to 200 Hz. This study compared the results of flow distortion and pressure recovery for the baseline, passive flow control and AFC configurations.

For the baseline configuration without flow control, following result was obtained shown in Fig 14:

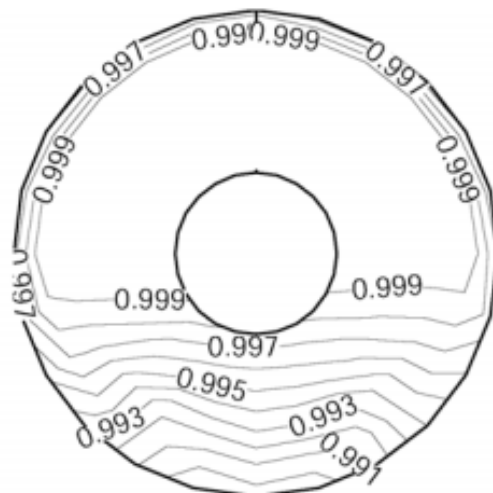


Figure 14: Total pressure ratio contour plot without flow control, DC60 = 29% [26]

Pressure recovery calculated for this case was 0.997. It can be seen from Fig 14 that the bottom part of the inlet experiences lower pressure ratios due to BLI. However, no flow separation occurred inside the inlet as the S-Duct geometry considered in this study has a low pressure gradient and Mach numbers are low.

For the configuration with AFC, following result was obtained shown in Fig 15:



Figure 15: Total pressure ratio contour plot with AFC, DC60 = 4.6% [26]

Pressure recovery for the case with AFC was also 0.997. The pressure recovery remained unchanged, but the distortion levels were significantly reduced due to the application of AFC. This improvement in flow distortion demonstrates the benefit of using AFC for engines ingesting a significant amount of boundary layer.

Another study by Brian G. Allan et al [13] shows the effects of AFC using control jets on circumferential distortion and pressure recovery in an embedded S-Duct inlet. These two results are shown in Fig 16 and 17. It can be seen in Fig 16 that the distortion values are high till a control jet mass flow ratio (MFR) of 0.75%. Above this level, the distortion begins to decrease finally reaching a minimum distortion level at a control jet MFR of 2.6%. For lower values of jet MFR, the bottom part of the AIP shows low total pressure regions, which are a characteristic of highly distorted flow due to ingested low momentum boundary layer. Whereas, the upper half of the AIP has high total pressure levels due to undistorted flow. With increasing jet MFR, the secondary flow formation inside the S-Duct reduces and distortion at AIP decreases.

Fig 17 shows that the pressure recovery reduces with increasing flow control. Generally, pressure recovery is expected to increase as deficits of the flow are reduced. According to Brian G. Allan et al, this unexpected decrease in pressure recovery is due to viscous flow interactions between control jets and the oncoming flow causing loss of energy. It is proposed that varying jet orientation might reduce these losses.

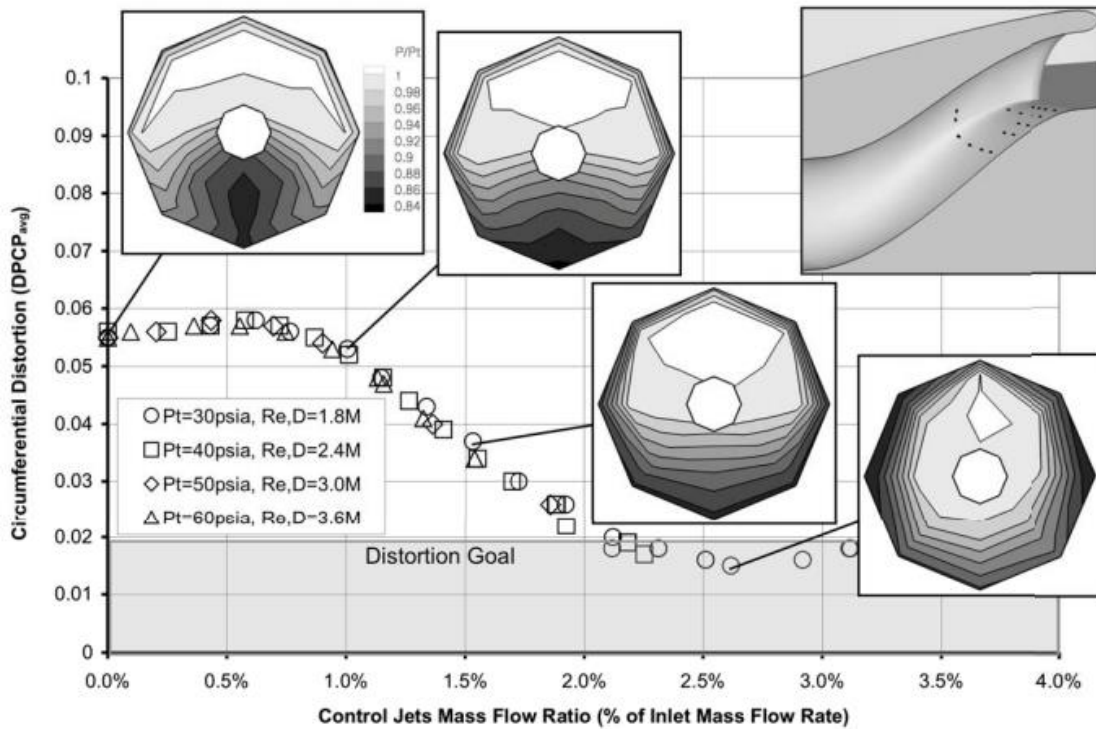


Figure 16: Variation of circumferential distortion with control jet mass flow ratio using AFC [13]

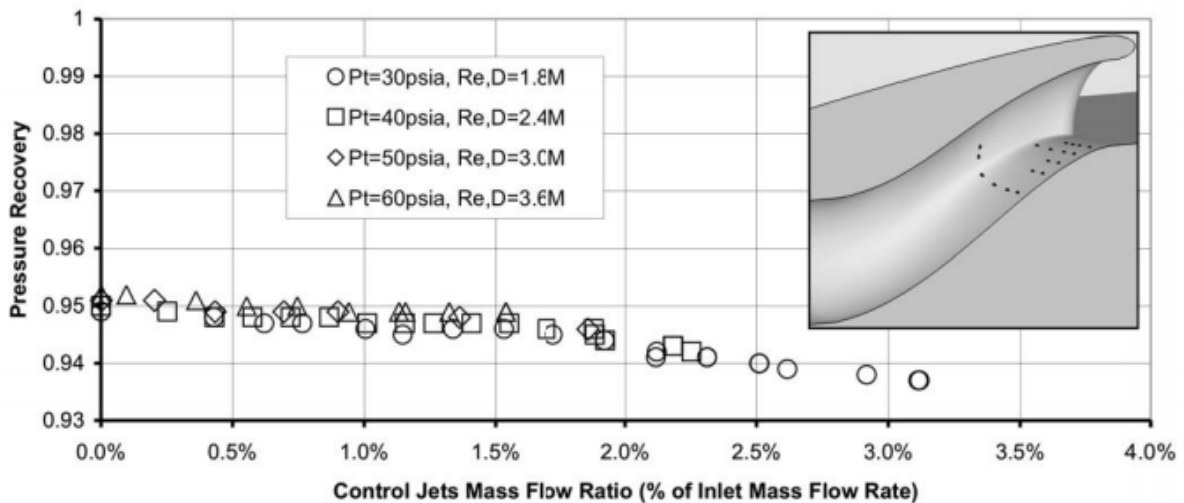


Figure 17: Variation of total pressure recovery with control jet mass flow ratio using AFC [13]

Ronald T. Kawai et al [5] demonstrated the benefit of AFC for BLI inlets. He also reasoned that elimination of separation due to AFC could enable shorter diffusers, which would result in less weight and wetted area and hence lesser drag. Lesser drag results in lower fuel consumption to generate equivalent thrust. This is shown in Fig 18.

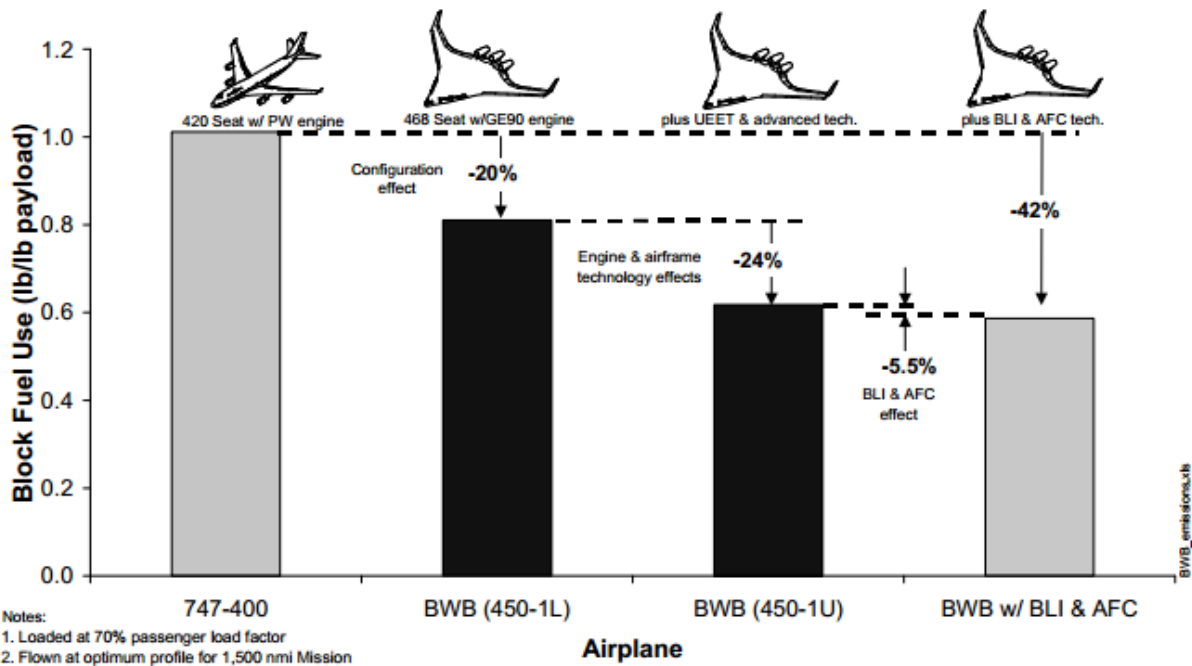


Figure 18: Potential fuel saving benefit of BLI with AFC [5]

3.2.2 Passive Flow Control (PFC)

Another widely used flow control technique to minimize losses associated with BLI in S-Duct embedded engines is the PFC. PFC can be implemented using various devices like VG's, fences, diverters, diverter bumps, etc.

Amer J. Anabtawi et al [11] conducted a research on semi-circular ducts ingesting thick boundary layers. To improve inlet performance, PFC was employed using VG's of different height, aspect ratio and shapes. Co-rotating VG's were used for PFC as a number of previous studies regarding VG pitch orientation [27] [28] [29] [30] have suggested that vortices shed by co-rotating array of VG's tend to have better wall attachment properties.

Anabtawi et al concluded that larger VG's (larger height) resulted in a lower distortion level than the base case (48.78% compared to 63.1% for base case). However, the pressure loss coefficient, C_{PtLoss} , increased when VG's were used (19.82% compared to 18.73% for base case) meaning the pressure recovery for the PFC case was lower than for the base case.

Fig 19 shows the variation of C_{PtLoss} with DC60 when VG's of varying heights are used for PFC.

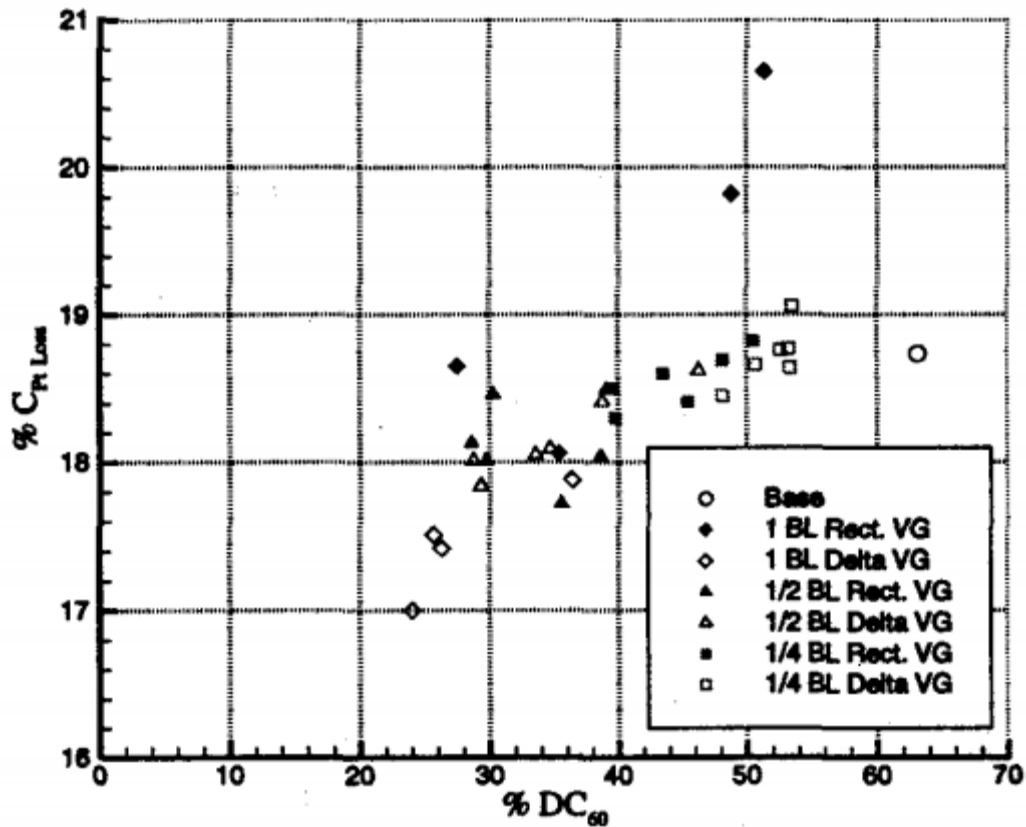


Figure 19: VG effect on inlet performance [11]

Although VG's tend to create additional pressure loss, studies have shown that VG's are able to decrease the loss in energy by changing the swirling direction thereby eliminating separation while reducing the total distortion [30] [31].

Lee and Liou [32] conducted a study to re-design a flush mounted inlet with BLI using a CFD based automated design process. This study also demonstrated the efficacy VG's as a PFC device. Boundary layer thickness of 30% of inlet height was assumed at a free stream Mach number of 0.85 and a Reynold's number of 3.8 million. For the CFD analysis, 3D Navier Stokes RANS solver was used with $k-\omega$ SST turbulence model. This study incorporated two design approaches. The first one was a shape design of the bottom surface near the inlet entrance in order to prevent additional BLI. The second one used VGs to reduce secondary flow formation inside the inlet duct. For the scope of this thesis, only the second approach is useful since the current thesis does not focus on non-BLI cases. Fig 20 shows the mesh system used for analysis for BLI and VGs. Fig 21 shows the results of the analysis comparing the inlet configurations with and without VG's and with and without surface design.

It is evident from Fig 21 that PFC through VGs reduces distortion as compared to non-PFC configurations.

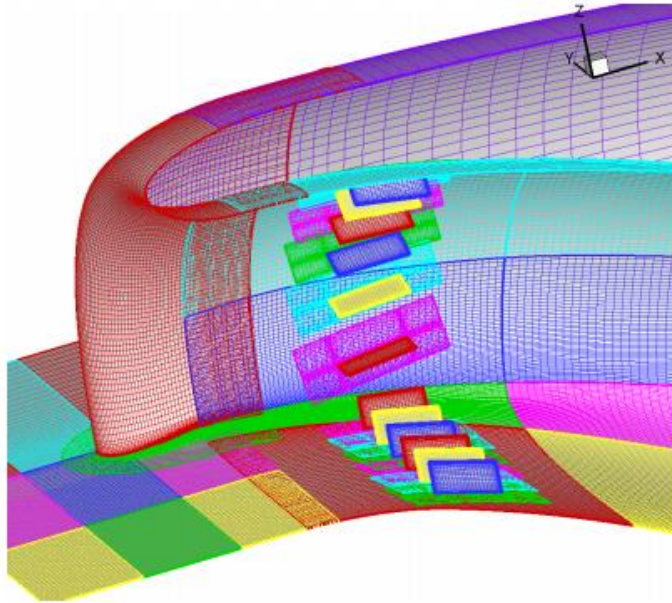


Figure 20: Grid system for BLI and VG's [32]

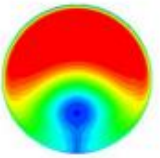
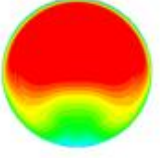
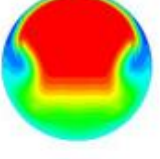
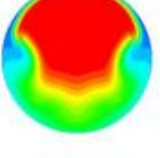
	Total Pressure Contour at AIP	PR	DPCP	MFR
Baseline w/o VG		0.5329	0.0596	0.9561
Surface Design		0.5578	0.0298	0.9872
Baseline w/VG		0.5016	0.0286	0.9617
VG Design		0.5081	0.0259	0.9672

Figure 21: Comparison of baseline and PFC cases [32]

3.2.3 Hybrid Flow Control (HFC)

HFC is a novel flow control technique that uses a combination of AFC and PFC devices to alter the inlet flow field in order to minimize losses associated with BLI.

A.N. Gissen et al [33] experimentally investigated the effectiveness of HFC as a means to reduce fan-face total pressure distortion at $M=0.55$. The HFC comprised of tandem arrays of passive (vanes) and active (synthetic) jets. Vane type VG's are instrumental in controlling separation in adverse pressure gradients [34]. This study selected synthetic jets for AFC since they are easier to manufacture and eliminate the requirement for engine bleed. It was concluded that HFC, AFC and PFC produce comparable results when distortion and pressure recovery are considered.

A similar study [35] concluded that, although nearly similar, HFC produces higher reduction in distortion as compared to AFC and PFC (an overall reduction of 35% at $M=0.55$).

3.3 Other Research Work Concerning BLI

Apart from studies regarding distributed propulsion systems and flow control, extensive literature exists on the experimental, theoretical and computational analysis of simple embedded S-Duct engine on a BWB without flow control, ingesting significant amount of the fuselage boundary layer.

Larry W. Hardin et al [4] conducted a trade factor-based system study to identify the benefits of BLI in fuel burn for generation-after-next (N+2) aircraft and propulsion system concepts. Numerical Propulsion System Simulation (NPSS) computational model was used for detailed engine cycle modelling. The results of this study are shown in Fig 22, which shows the benefit in thrust specific fuel consumption (TSFC) for several architectures (different aspect ratios, wake recovery parameter, R, percent of BLI, number of engines) compared to theoretical limits.

Fig 22 shows that two of the configurations are capable of ingesting 11% of the total aircraft drag and still show different TSFC benefits. Hardin et al reasoned that it has to do with the axial position of the intake. Less drag was incurred by the forward positioned 3-engine configuration. Hence it is a more desirable configuration than the 5 engine case from the drag standpoint. The major goal of next generation propulsion systems is to provide continued reductions in fuel burn. BLI provides significant improvements in propulsive efficiency for these propulsion systems. Hardin et al also showed benefits on the order of 10% for N+3 configurations in their study.

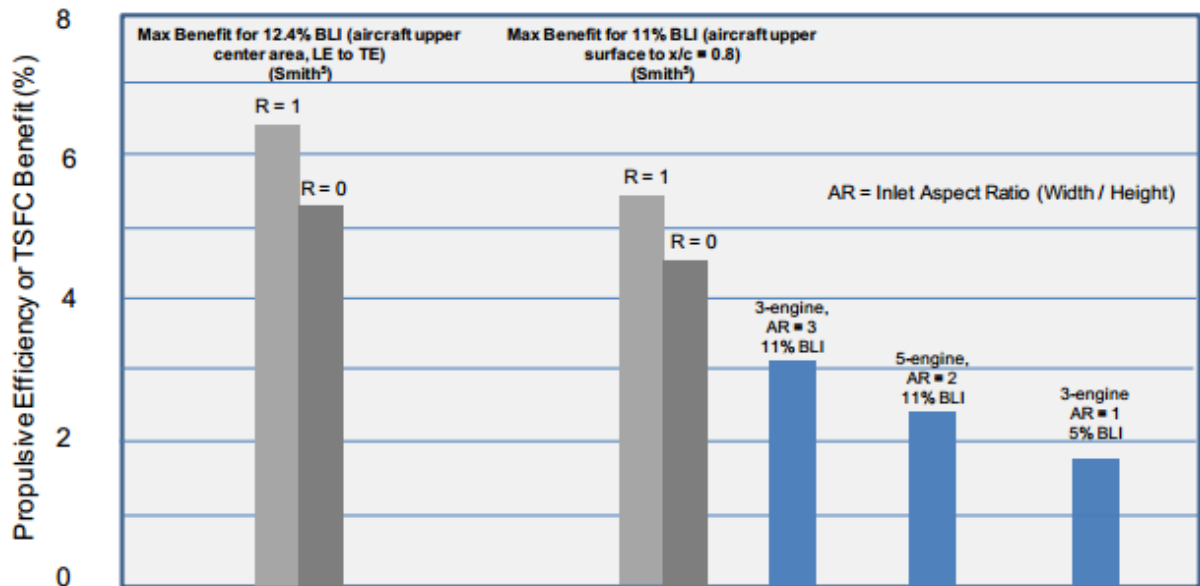


Figure 22: TSFC benefit for several architectures compared to theoretical limits [4]

Generally, BLI is associated with two opposite trends; first is an increase in propulsive efficiency due to lower inlet velocity and reduced ram drag and the second is a decrease in cycle efficiency due to inlet distortion. Nevertheless, a good potential for fuel savings is always evident [36].

A 2D computational analysis was conducted by Riti Singh et al [36] to identify the effects of BLI propulsion system in transonic flow. This study investigates the effects of BLI on a number of propulsion system design parameters like mass flow ratio (MFR), Mach number, angle of attack (AOA), flow distortion, pressure recovery, etc. A distributed propulsion system under a common nacelle over a BWB was considered for analysis and a structured mesh was created in ANSYS ICEM CFD using RANS equations and $k-\omega$ SST as the turbulence model. Fig 23 shows the structured mesh of the model.

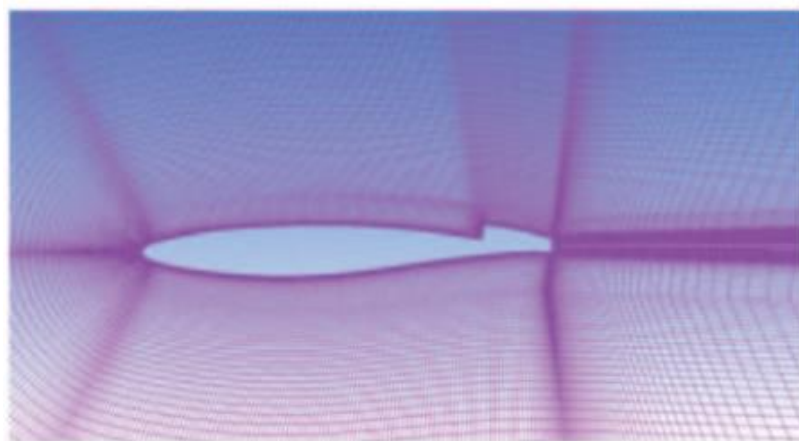


Figure 23: Mesh around the airfoil and engine [36]

The solution led to the following results, which are shown in Fig 24, 25, 26 and 27:

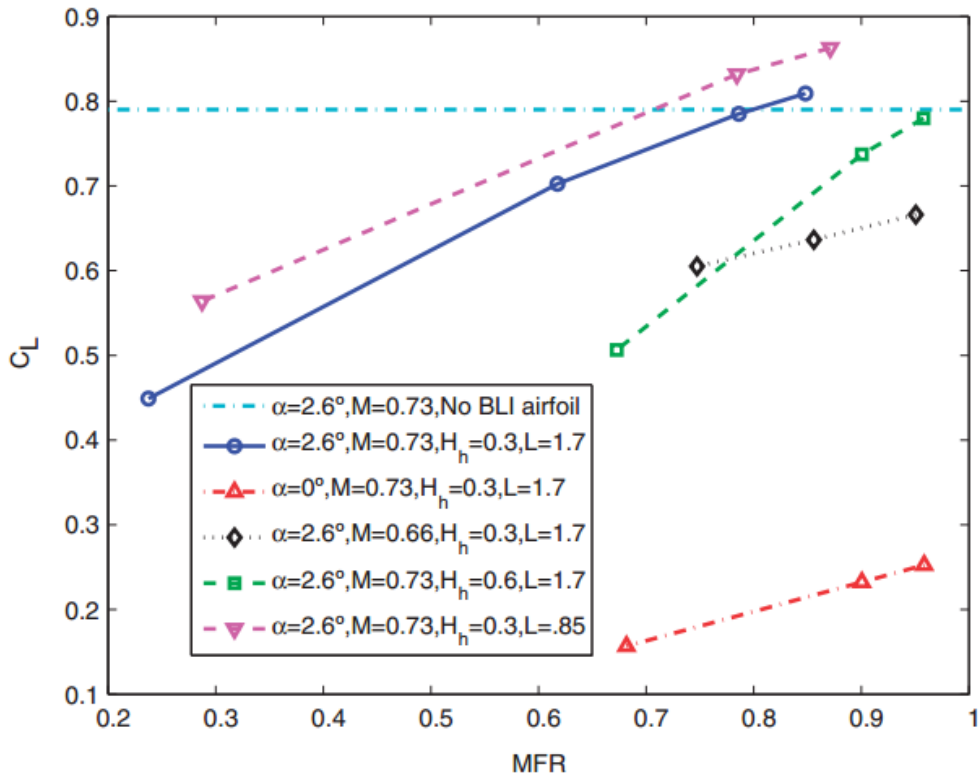


Figure 24: MFR influence on lift coefficient [36]

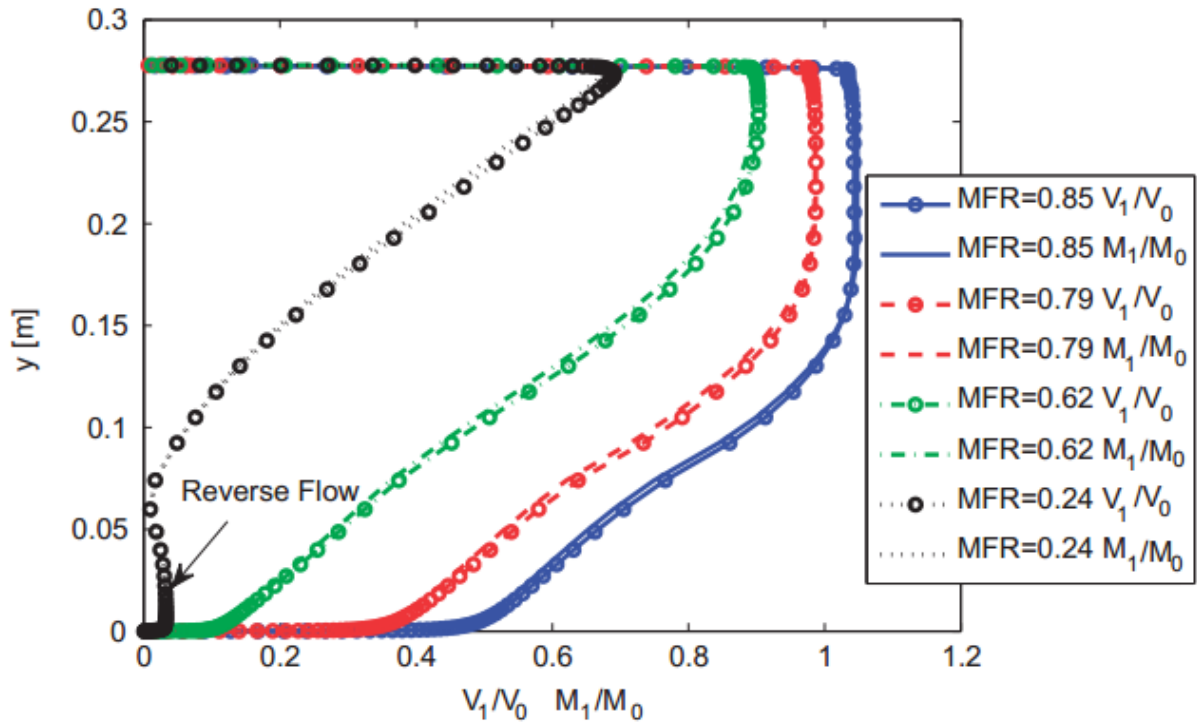


Figure 25: Boundary layer velocity and Mach number profiles at intake throat for different MFRs, $M=0.73$ [36]

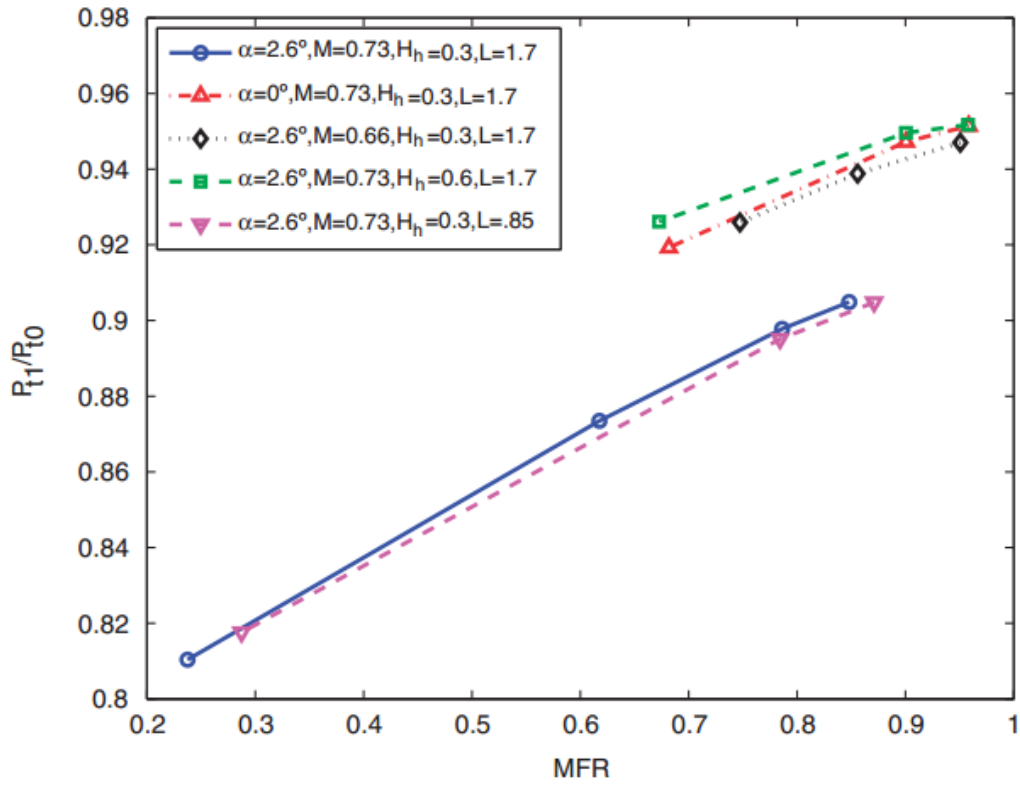


Figure 26: MFR influence on total pressure recovery [36]

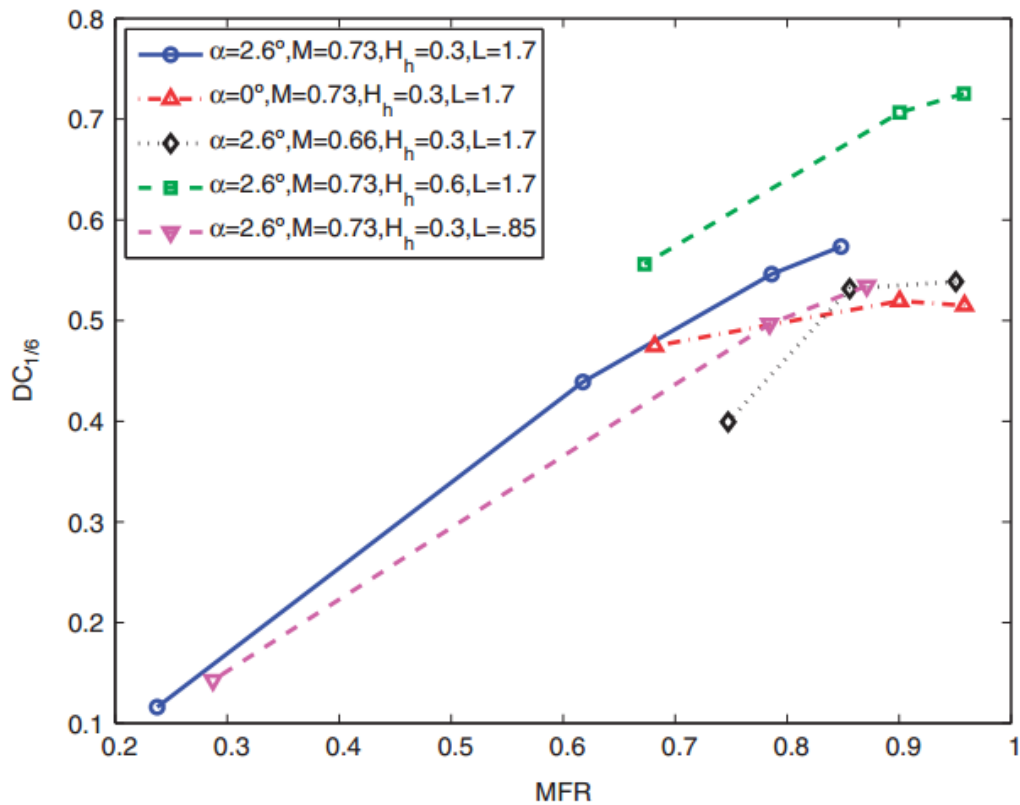


Figure 27: MFR influence on Distortion coefficient [36]

MFR is the ratio of the area of incoming streamtube of air to the geometrical throat area and is given by equation (2.2):

$$MFR = \frac{A_0}{A_{th}} = \frac{W_{fan}}{\rho_0 V_0 A_{th}} \quad (2.1)$$

As can be seen from Fig 24, increasing MFR increases the lift coefficient since high MFR increases the suction upstream of the engine and creates a more favorable pressure gradient. This reduces boundary layer thickness. Moreover, higher MFR creates higher acceleration on the upper surface of the airfoil, which creates more suction and hence increase overall lift coefficient.

However, in Fig 25, lower MFR values tend to create flow reversal, thereby adding losses. This is due to boundary layer growth at low MFR, since a recirculation region is created in the pre-compression zone ahead of the inlet due to an adverse pressure gradient. Fig 26 and 27 show the influence of MFR on pressure recovery and distortion coefficient, respectively. It can be seen that at low MFRs, due to large flow separation as describe above, pressure recovery is reduced. On the other hand, large flow separation at low MFR reduces average total pressure at the AIP and hence reduces the distortion which is evident in Fig 27.

Another study [38] focusing on the CFD analysis and wind tunnel testing of a BWB with BLI nacelles confirmed the predicted improvements, due to BLI, in forces and moments acting over the BWB. Catalano and Munoz [38] also tested a BWB configuration with BLI nacelles to study the effects of engine-airframe integration and concluded an overall efficiency increment of 25% as compared to a conventional aircraft.

Apart from computational and experimental research work, novel optimisation techniques also offer an alternative for BLI inlet design as it effectively takes into account the strong couplings between different systems. A Stanford University study by David L. Rodriguez [14] focused on a multidisciplinary design optimisation method to design BLI inlets. Rodriguez combined a Navier-Stokes flow solver, an engine analysis method and a non-linear optimiser into a single design tool to address the coupling of the problem. Fig 28 shows the inlet design tool setup for the implementation of MDO scheme. The design variables are passed to the flow solver from the optimizer. After modifications to inlet shape, airframe shape and grid settings, required aircraft thrust (T) and inlet pressure recovery (η_r) are evaluated by the flow solver. Then, these values are transferred to the engine simulator, where required airflow rate and fuel burn rate (\dot{m}_f) calculated. These values are then returned back to the optimizer along with C_l , C_m , $DC60$ and the predicted airflow rate. Using these values, the optimizer determines a new set of design variables while satisfying the constraints and minimizing the objective function. The process is iterated until an optimum solution is achieved. The design variables used for optimization are shown in Fig 29.

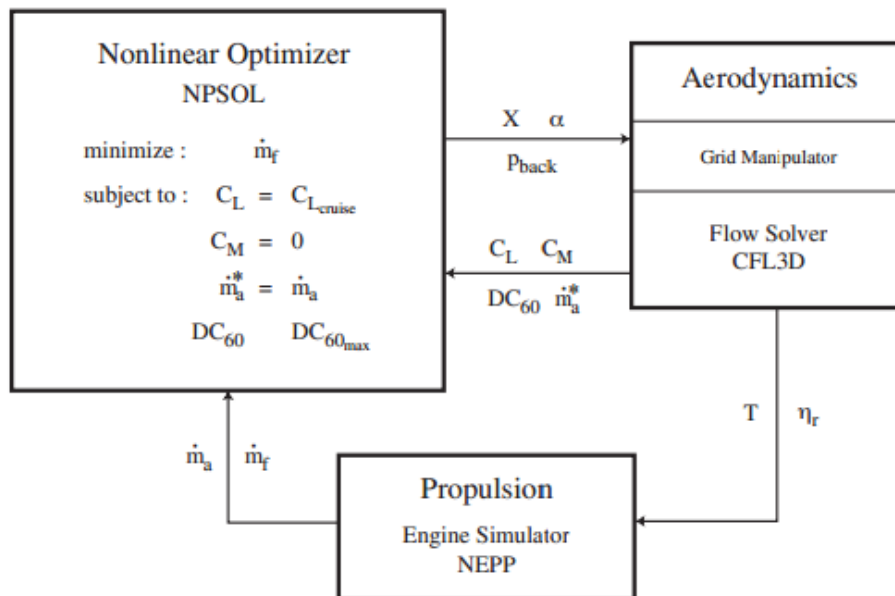


Figure 28: Setup of the inlet design tool [14]

Variable	Type	Location
1	angle of attack	entire aircraft
2	inlet back pressure	centerline engine fan-face
3	inlet back pressure	outboard engine(s) fan-face
4	linear wing twist	outboard wing section
5	inlet length	outboard nacelle
6	inlet length	centerline nacelle
7	nacelle thickness	centerline nacelle
8-10	inlet/nacelle camber	centerline nacelle
11-12	inlet lower wall	centerline nacelle
13-14	inlet junction/wall	centerline nacelle
15	inlet upper/side wall	centerline nacelle
16	inlet upper wall	centerline nacelle

Figure 29: Design variables used in the optimization for BWB [14]

Following the completion of optimization a number of useful results were obtained. These results are shown in Fig 30. It is seen from the first plot that the fuel burn rate has been reduced by approximately 4% of the baseline value. Reductions are also seen in the values of drag coefficient and distortion coefficient. On the other hand, the centerline inlet pressure recovery increased.

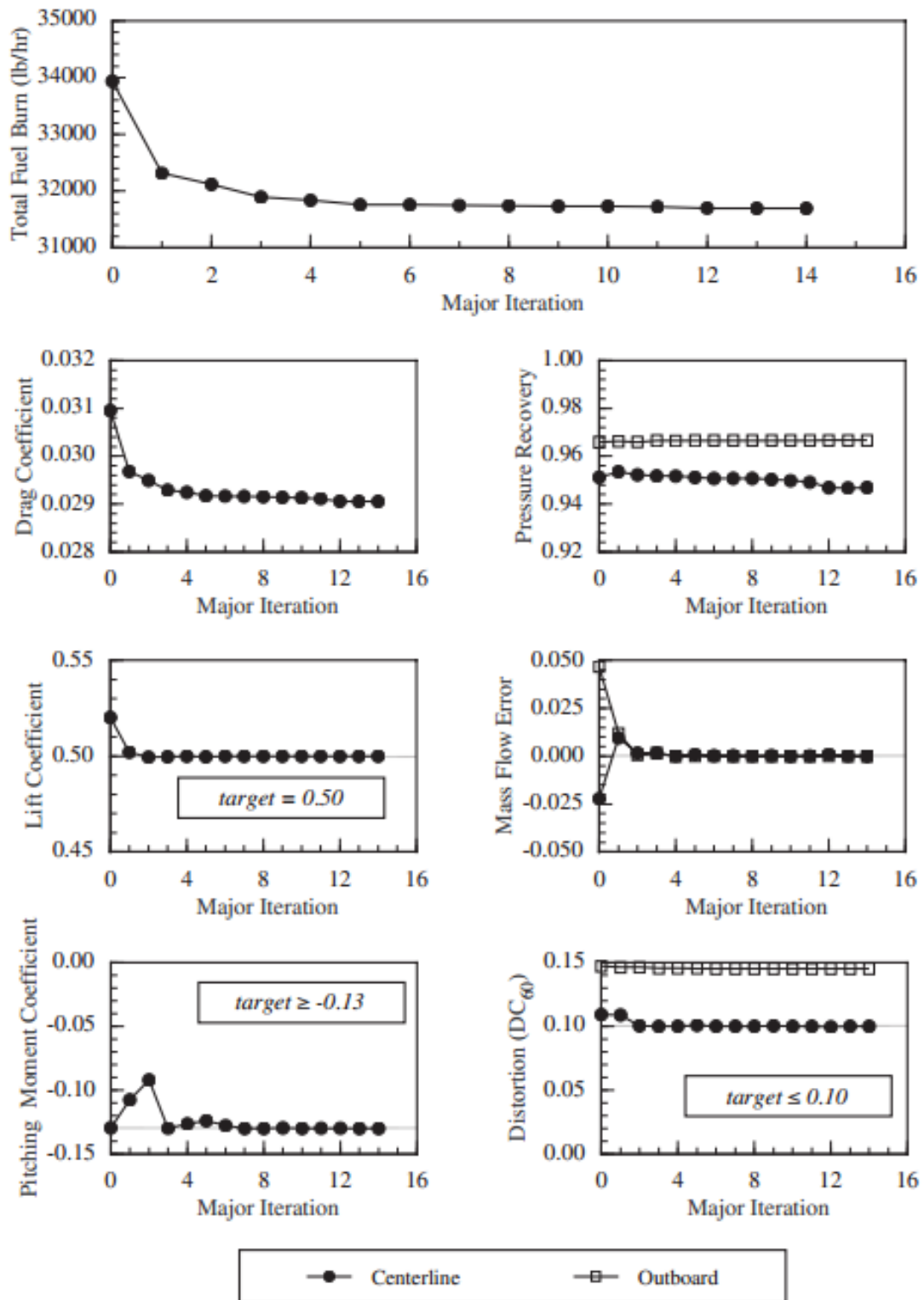


Figure 30: Performance results of optimization [14]

The values of these parameters are also shown in Fig 31 and the pressure contours on BWB nacelles and at AIP are shown in Fig 32 and 33, respectively.

Performance Parameter	Baseline	Optimized
Fuel Burn Rate (lb/hr)	32923	31691
Lift Coefficient	0.50005	0.50000
Pitching Moment Coefficient	-0.11813	-0.13000
Drag Coefficient	0.02974	0.02905
Centerline Mass Flow Error	0.00000	0.00002
Centerline Inlet Pressure Recovery	0.92717	0.94691
Centerline Fan-face Distortion (DC ₆₀)	0.09829	0.10003
Outboard Mass Flow Error	0.00000	0.00000
Outboard Inlet Pressure Recovery	0.96635	0.96663
Outboard Fan-face Distortion (DC ₆₀)	0.14531	0.14517

Figure 31: Comparison of performance parameters for baseline and optimized BWB configurations [14]

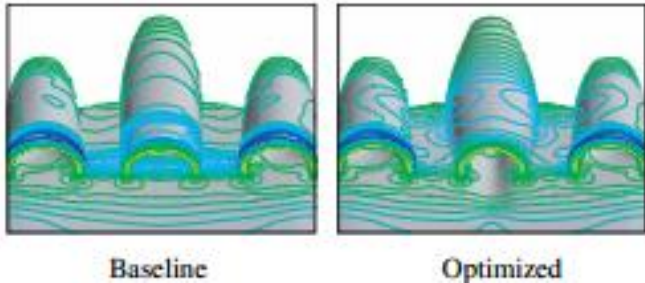


Figure 32: Comparison of pressure contours for BWB nacelles; baseline and optimized [14]

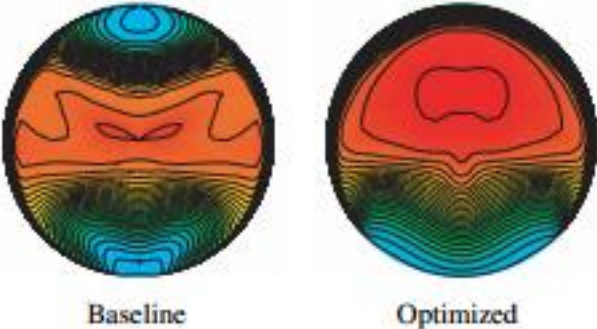


Figure 33: Pressure contours at AIP for baseline and optimized BWB configurations [14]

Fig 32 shows the elimination of the shock within the choked baseline inlet in the optimized result, which has contributed to a decrease in drag and increase in pressure recovery seen in Fig 31. Fig 33 also shows the improvement in pressure recovery for the optimized configuration. The small pocket of low pressure on the top of the fan-face, caused due to flow separation because of shock inside the choked baseline inlet, has been eliminated in the optimized result.

Overall, the MDO scheme proved to be successful in producing promising results, however the ability to reduce distortion levels appeared to be limited. This has been proposed to be because of the design of baseline inlet. Even though, the method proved to be effective, Rodriguez concluded it to be “too slow and not robust enough to apply in production mode”.

A number of other researchers [39] [40] [41] [42] [43] [44] have also attempted to study the effects of BLI and S-Ducts on BWB aircrafts and conclude reasonably effective results and feasibility in operation.

4

Existing Inlet Parameterization Examples

Design of the nacelle plays a crucial role in the performance of a propulsion system (as is seen from the results of existing literature on inlet design). Especially, for integration on a BWB and the issues arising due to the engine/airframe coupling, the design of the nacelle becomes all the more important when BLI is taken into account. This section attempts to look at some studies focusing on design and parameterization of the nacelle geometry.

4.1 Nacelle Geometry Definition

Riti Singh et al [36] have presented a detailed nacelle geometry definition using RAE2822 as the airfoil for the fuselage body with the engine nacelle located at the upper aft part of the airfoil ingesting fuselage boundary layer. In this study, the nacelle is divided into forebody and afterbody. In order to minimize length, midbody was not considered. Fig 34 depicts the main geometry parameters defining the 2D nacelle.

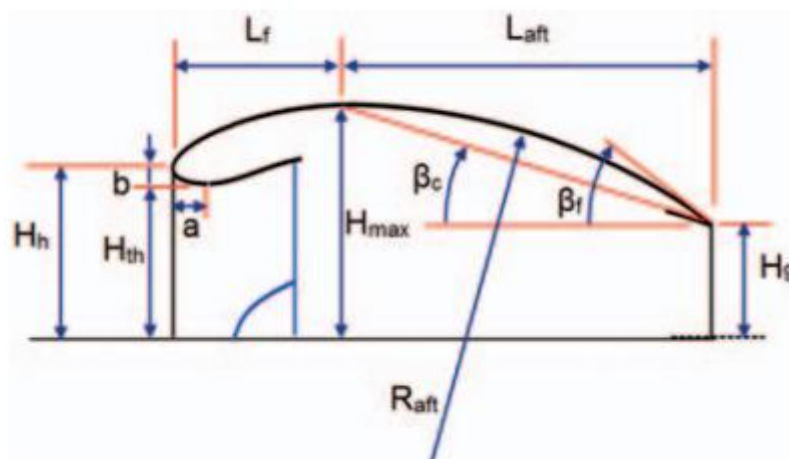


Figure 34: Nacelle geometry definition [36]

First, the design of forebody is considered, where dimensionless parameters, H_h , H_{max} and L_f are used to define the geometry. The performance parameters of the nacelle are drag rise Mach number, M_D , and critical mass flow ratio, MFR_{crit} , for the onset of significant spillage drag. Equations (2.2) and (2.3) give the relations for MFR_{crit} and M_D , respectively:

$$MFR_{crit} = \left(1 - 4 \frac{\left(1 - \frac{H_h}{H_{max}}\right)^2}{\frac{L_f}{2H_{max}}}\right)^{\frac{5}{2}} \quad (2.2)$$

$$M_D = 1 - \frac{1}{8} \frac{\sqrt{1 - \left(\frac{H_h}{H_{max}}\right)^2}}{\frac{L_f}{2H_{max}}} \quad (2.3)$$

Here, H_h is the highlight height, H_{max} the maximum height of cowl and L_f is length of the forebody.

Next, the design of afterbody is taken into account, where a circular boat-tail profile is considered. Equations (2.4), (2.5) and (2.6) show the relations for final boattail arc and the radius of the nacelle:

$$\tan(\beta_c) = \frac{(H_{max} - H_9)}{L_{aft}} \quad (2.4)$$

$$\beta_f = 2\beta_c \quad (2.5)$$

$$R_{aft} = \frac{L_{aft}}{\sin(\beta_f)} \quad (2.6)$$

Here, H_9 is the nozzle height, L_{aft} is afterbody length, β_c is the chord angle, β_f is the final boattail angle and R_{aft} is the arc radius.

Finally, design of lip is considered, where an elliptic lip is used between the highlight and the throat (H_{th}). Equations (2.7) and (2.8) give the relations between the semi-major and semi-minor axes of the elliptical lip with highlight and throat height:

$$a = 2b \quad (2.7)$$

$$b = H_h - H_{th} \quad (2.8)$$

Here, 'a' is the lip length and 'b' is its height.

The height of the lip, b, comes from equation (2.9), which gives the relation for contraction ratio, Cr:

$$Cr = \frac{A_h}{A_{th}} = \frac{H_h}{H_{th}} \quad (2.9)$$

Here, A_h is the highlight area and A_{th} is the throat area.

Equation (3.0) gives the relation for the length of the nacelle:

$$L_{tot} = L_f + L_{aft} \quad (3.0)$$

The study carried out by Riti Singh et al presents the nacelle geometry definition as described above but does not consider many inlet performance parameters.

4.2 Inlet Design Parameters

Lemmens [7] carried out research on feasibility of embedded engines with BLI on AeroCity, a part of which was the parameterization of the inlet and duct. Fig 35 shows the inlet and duct design parameters used by Lemmens in his study.

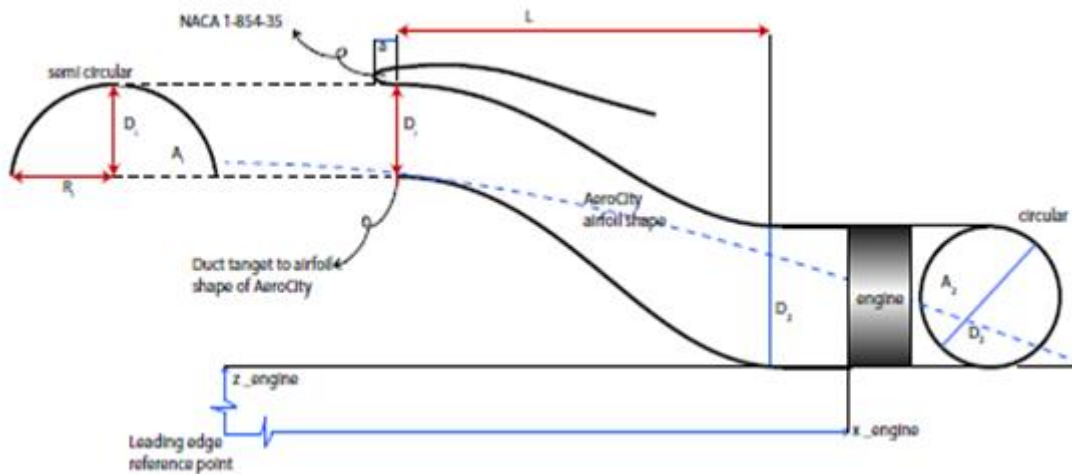


Figure 35: Inlet and duct design parameters [7]

The length of the duct, L , is considered as a design parameter. The steepness of the duct curvature and internal surface area is determined by the length L . Lemmens reasoned that the steepness of the duct has a large influence on the distortion level. The steeper the duct, the shorter its length and higher secondary flows will lead to high distortion. On the other hand, a longer duct would mean higher friction losses, which will lead to loss of pressure recovery. So duct length has to be chosen carefully.

Another design parameter considered in this study is the inlet shape since it has a direct influence on the amount of boundary layer ingestion. Following the conservation of mass at the AIP, equation (3.2) was obtained, which gives the relation between the inlet area, A_{i1} , and the area at the AIP, A_2 :

$$\dot{m}_a = \rho VA \quad (3.1)$$

$$A_i = A_2 \frac{\rho_2 V_2}{\rho_0 V_0} \quad (3.2)$$

Lemmens introduced a design parameter, Φ , which he defined as the ratio of the inlet radii (semi-major axis and semi-minor axis) shown in equation (3.3):

$$\Phi = \frac{R_i}{D_i} \quad (3.3)$$

$$A_i = \frac{1}{2} \pi R_i D_i \quad (3.4)$$

Combining all these equations, Lemmens found the relations for inlet radii in terms of the design parameter, Φ , as shown in equations (3.5) and (3.6):

$$R_i = \sqrt{\frac{2}{\pi} \Phi A_2 \frac{\rho_2 V_2}{\rho_0 V_0}} \quad (3.5)$$

$$D_i = \sqrt{\frac{2}{\pi \Phi} A_2 \frac{\rho_2 V_2}{\rho_0 V_0}} \quad (3.6)$$

In this way, the design parameter, Φ , comes to determine the shape of the inlet. If it is less than 0, then the inlet will be higher and less wide meaning %BLI will be less. If it is equal to 0, then the inlet will be circular. If it is greater than 0, then the inlet will be wider and less high meaning %BLI is larger. This can be seen in Figure 35a.

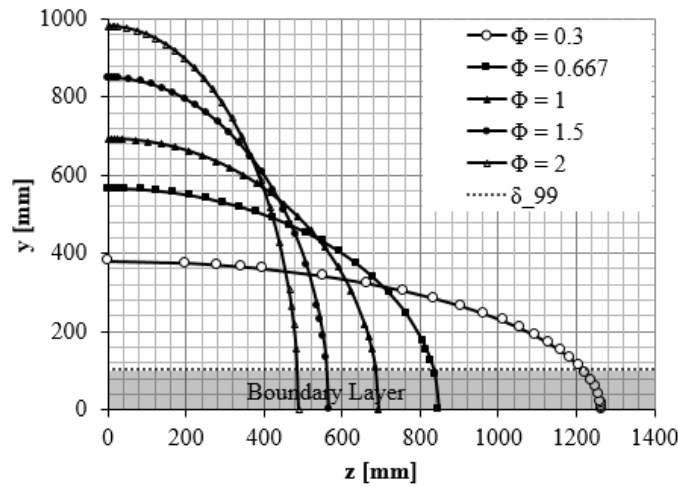


Figure 35a: Inlet shapes with varying Φ [7]

4.3 Design of Engine Inlet for JI5D-1

Duncan Reijnen [45] carried out a detailed study into the design of S-Duct engine inlet at $M_{cr}=0.5$ for JI5D-1 engine. He divided the inlet design in internal and external nacelle and described the parameters affecting the same. This study contains detailed parameterization of the internal and external geometry inlet as well as parameters affecting the performance of the inlet.

As the geometrical parameterization is already covered in Sections 3.1 and 3.2, this section will only briefly describe the parameters affecting performance of S-Duct inlets. Reijnen described the following parameters affecting performance in his study:

a) *Contraction ratio*

Pressure recovery directly depends on the contraction ratio since a correctly chosen contraction ratio avoids flow separation and flow spillage. Reijnen showed in his results that an increase in contraction ratio results in an increase in pressure recovery at taxi, take-off, climb and landing speeds.

b) *Lip sizing*

Based on the survey conducted by Reijnen, it was found that the flattest pressure distributions were identified for the lips with the largest radius at MFR near 1. However, at lower values of MFR, it was found that lips with smaller radius had more uniform pressure distribution. So, a careful design for the lip is required in order to minimize drag losses.

c) *Inlet diameter ratio*

Smaller inlet diameter generally has more uniform pressure distribution.

d) *Inlet critical Mach number*

The inlet design has to be such that the critical Mach number stays below the acceptable value in order to prevent flow spillage and hence drag.

e) *Angle of attack*

The lip experiences higher pressure coefficient when the angle of attack is increased. This plays a crucial role, when flow separation is considered. Very high angles of attack can also lead to flow spillage.

The parameters described above are only a small part of a number of factors that influence inlet design and performance. Reijnen's research presents a detailed parameterization and performance calculations for S-Duct inlet, which is of vital use to the current thesis project.

5

Parameterization, Numerical Modelling and Approach

This chapter focuses mainly on the design approach, parameterisation and numerical modelling of the inlet configurations tested in the thesis. The first part of this chapter sheds light on the criteria for S-Duct inlet design followed by the geometrical parameters that affect the S-Duct design. After this, the parameters relevant to this thesis are chosen for testing the influence of their geometrical variations on pressure recovery, distortion, etc. results at the AIP. The combinations of these geometrical variations are formulated in the form of a flowchart to show the number and type of tests performed to obtain the final design. Also included in this chapter is an insight into the numerical modelling, mesh setup and the parameters affecting the mesh topology. This is followed by a description of the stages of testing performed. In addition to this, a section on validation is also provided to present a verification for the results.

5.1 Criteria for S-Duct Design

While designing the embedded engine inlet, there are certain criteria that need to be kept in mind. The inlet should be able to produce the following:

- a) Low total pressure distortion at the AIP
- b) High total pressure recovery at the AIP
- c) High BLI for high wake recovery
- d) Acceptable velocity at the engine fan-face for high pressure rise across compressor
- e) Minimal secondary flow formation inside the S-duct
- f) Low overall drag

As stated before, low total pressure distortion and high total pressure recovery are the major success criteria for this thesis. In addition to these, it is important for the inlet to ingest as much of the fuselage boundary layer as possible in order to minimize wake dissipation. However, ingesting a large amount of boundary layer also implies a large pressure distortion level at the AIP. These alternating pressure fields at the AIP cause non-uniform load distribution over the fan and reduce the fatigue life of the blades. This means even though ingesting a large amount of boundary layer can reduce wake dissipation and hence reduce fuel consumption, it can also significantly affect inlet performance, which can in turn reduce the potential benefits associated with BLI.

One of the major functions of an inlet requires it to bring the airflow at an acceptable velocity and angle at the fan face. A high inlet velocity implies an increase in ram drag, whereas a very low velocity implies lower pressure rise across the fan. Because of the shape of the S-Duct, another important factor to keep in mind is the formation of secondary flow inside the duct, which affect inlet performance, so the design has to be such that it minimizes the formation of these flows.

5.2 Parameters Affecting Duct Design

The design of the S-Duct depends on a number of geometrical parameters, some of which are listed as follows:

- a) Inlet duct offset
- b) Curvature of the two bends (spline shape)
- c) Area Ratio (Fan area/Inlet throat area)
- d) Aspect ratio of inlet (width of inlet face/height of inlet face)
- e) Length of duct
- f) Height of duct
- g) Percentage of BLI

Mentioned above are some of the major parameters that affect the design of an S-Duct inlet. However, the scope of this thesis is limited to testing by geometrical variations in length, height and aspect ratio of the duct.

5.3 Parameterization of S-Duct

As a starting point for testing, major parameters that affect the geometry of an inlet are discussed in the following section.

5.3.1 Main Geometrical Parameters for Inlet Design

The main geometrical variables for the design of the S-Duct are chosen as follows:

1. Aspect Ratio of inlet face ($AR = a/b$)
2. Length of duct (L)
3. Height of duct (H)
4. Contraction Ratio ($CR = A_{hl}/A_{th}$)
5. Lip semi major-to-minor axis ratio (m/n)

a) Aspect Ratio of inlet face

Aspect ratio directly relates to the shape of the inlet face. The percentage of boundary layer ingested by the inlet is directly related to the aspect ratio of the inlet face. The testing in the current thesis is conducted on semi-elliptical inlets. Hence, the aspect ratio of the inlet face is defined as the ratio of the length of major axis of the inlet face to the length of semi-minor axis of the inlet face as shown in Fig 36 and equation (3.7):

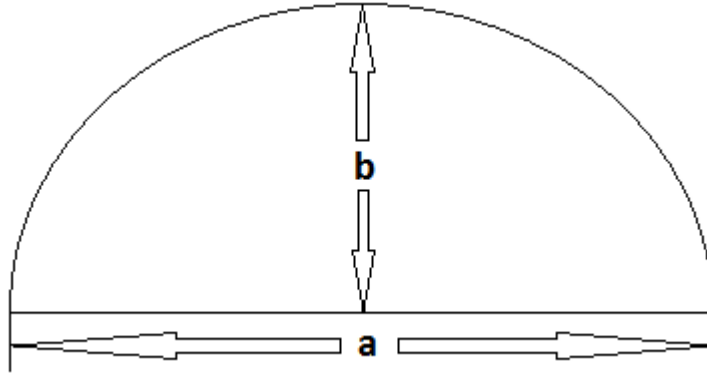


Figure 36: Major axis length ('a') and semi-minor axis length ('b') for inlet face

$$AR = \frac{a}{b} \quad (3.7)$$

Here, 'a' is the major axis length and 'b' is the semi-minor axis length of the inlet face.

This means, as the aspect ratio is increased, the inlet face becomes more elliptically wider than higher and vice versa. Increasing the aspect ratio to a high value will mean a very wide inlet with less height, which signifies a high distortion at the AIP due to very large amount of BLI. On the other hand, a low aspect ratio would mean less distortion at the AIP, but also less amount of BLI, which reduces the benefits associated with BLI. Therefore, an optimum value for aspect ratio has to be selected keeping in mind a balance between the values of these parameters.

b) Length of Duct

In addition to inlet aspect ratio, the length of the inlet is also a critical factor that affects inlet performance. Hence, optimised selection of a value for length requires careful consideration as well. For the same height, a longer length would mean that the boundary layer entering the inlet will experience lesser adverse pressure gradient due to reduced slope of the lower spline of the inlet. However, a shorter length would indicate a higher adverse pressure gradient, which would create larger secondary flow formation at the second bend of the S-Duct directly affecting total pressure recovery and distortion at fan face. On the other hand, a higher length value implies a higher internal surface area, which will induce more losses inside the boundary layer due to wall friction as compared to a shorter length duct. So, duct length is a major design parameter in the selection of a high performance inlet configuration.

Fig 37 shows the definition of the length and height of an inlet configuration tested in this thesis. Length (L) is the horizontal distance between the throat and the fan face. Height (H) is the vertical distance between the center of the inlet face and center of the fan face.

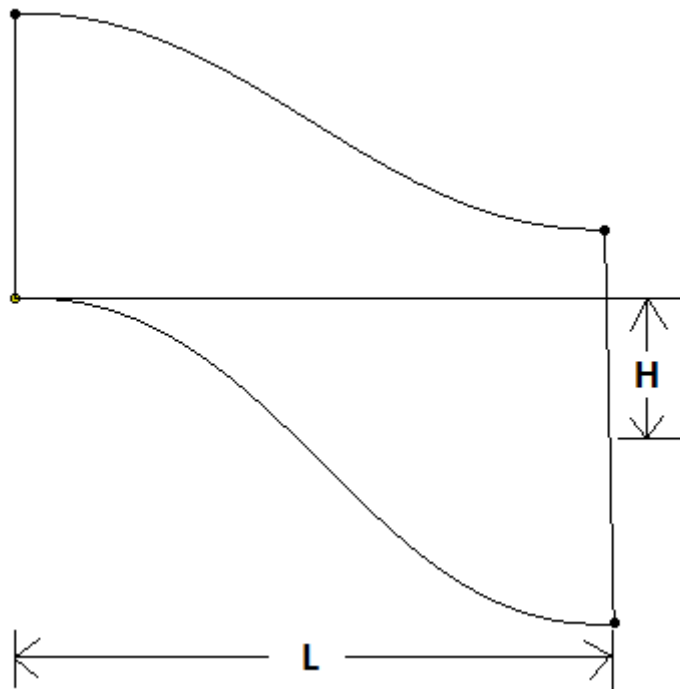


Figure 37: Definition of length and height of an inlet configuration

c) Height of Duct

As can be seen from Fig 37, the height of the inlet is parameterized from center of inlet face to center of the engine fan-face. This means height of the duct would directly control the formation of secondary flows inside the duct. Increasing the height will cause the ingested low momentum boundary layer to separate more quickly due to higher adverse pressure gradient at the bottom wall of the S-Duct. A lower height will make the separation more gradual. Hence a lower height value is preferred for this case.

d) Contraction Ratio

Contraction Ratio is defined as the ratio of the area at the highlight (A_{hl}) to area at the throat (A_{th}) of the inlet. Contraction ratio affects pressure recovery. An optimum value of contraction ratio helps avoid flow separation at the entry of the inlet. Fig 38 shows the highlight and throat areas of the inlet.

Contraction Ratio (CR) is given by the following relation:

$$CR = \frac{A_{hl}}{A_{th}}$$

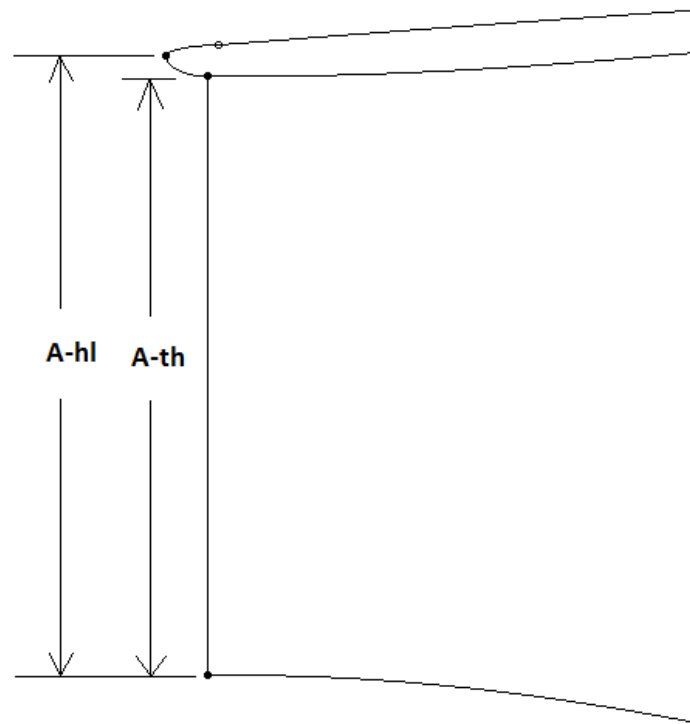


Figure 38: Highlight area and throat area at upstream inlet

e) *Lip semi major-to-minor axis ratio*

Lip sizing is critical in improving pressure recovery and reducing spillage drag. This is controlled by the ratio of the semi-major axis of lip ellipse, m , and the semi-minor axis of the lip ellipse, n . A correct value of m/n will ensure no separation upstream of the throat and hence a higher pressure recovery. Moreover, it is essential in accommodating a wide range of inflow angles. Fig 39 shows the geometry of the nacelle lip and geometrical parameters 'm' and 'n'.

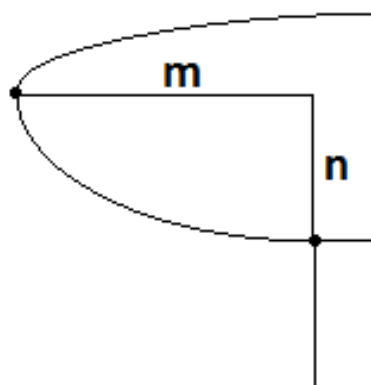


Figure 39: Nacelle lip construction

5.3.2 Calculation of Area Ratio

Equation (3.8) shows the relation for area of a semi-ellipse:

$$A = \frac{1}{2} \pi xy \quad (3.8)$$

Here, 'x' and 'y' are the semi-major and semi-minor axes of the ellipse, respectively.

The calculations for finding out the area ratio of the S-Duct are carried out using Freuler's approach [2]. To do this, the 1-D isentropic Area-Mach relation is used, shown in equation (3.9):

$$\left(\frac{A}{A^*}\right) = \frac{1}{M} \left(\frac{2}{\gamma+1} \left(1 + \frac{\gamma-1}{2} M^2\right)\right)^{\frac{\gamma+1}{\gamma-1}} \quad (3.9)$$

Assuming a fan Mach number of 0.6, $\frac{A_F}{A^*} = 1.188$

And for a throat Mach number of 0.72, $\frac{A_T}{A^*} = 1.081$

Therefore,
$$\frac{A_F}{A_T} = 1.099 \approx 1.1 \quad (4.0)$$

This means, **Fan Area = 1.1 * Inlet area**

Now,
$$\text{Area of fan} = \frac{\pi D_{fan}^2}{4}$$

Engine dimensions are given and their values are as follows:

1. Diameter of engine fan = 3.23m
2. Length of engine = 4.75m

Using fan diameter value of 3.23m, **area of fan** is calculated to be **8.194 m²**.

So, from equation (4.0), **area of inlet throat** is calculated to be **7.45 m²**.

Following this, based on the area ratio calculations, values for 'a' and 'b' for different aspect ratios are obtained as shown in Table 1:

Table 1: ‘a’ and ‘b’ values for different aspect ratios for area ratio = 1.1

Aspect Ratio, AR	‘a’ (in meters)	‘b’ (in meters)
1	3.08	3.08
1.25	3.443	2.754
1.5	3.772	2.514
1.75	4.074	2.328
2	4.356	2.178
2.5	4.87	1.948

Based on the values for ‘a’ and ‘b’ shown in Table 1, their corresponding aspect ratios are tested to understand the effect of variation of aspect ratio, and hence percentage of BLI, on the total pressure distortion and total pressure recovery at the engine fan face. An optimum value of inlet aspect ratio will be an instrumental factor in improving inlet performance.

Table 2 shows all the values of aspect ratio, length and height of duct tested in this thesis. A combination of these values will determine the most optimum S-Duct inlet configuration. Afterwards, some more inlet configurations are tested to further improve results.

Table 2: Values of geometrical parameters for testing

Aspect Ratio (AR)	Height of Duct (H)	Length of Duct (L)
1	1.5m	4.85m
1.25	1.052m	5.65m
1.5	0.7m	6.46m
1.75	0.3m	7.27m
2		
2.5		

5.4 Operating Conditions

Table 3 shows the operating conditions that were used for the simulations:

Table 3: Operating Conditions

Flight Regime	Cruise
Altitude	10000 m
Mach Number	0.82
Free-stream Velocity	279 m/s
Density of Air	0.41 kg/m ³
Dynamic Viscosity of Air	0.0000147 Pa-sec
Heat Transfer	None
Molar Mass of Air	29 kg/kmol

5.5 Numerical Modelling: Governing Equations

The software used for solving the equations governing the flow and the subsequent analysis was ANSYS CFX. The underlying numerical algorithms are solved for a number of boundary conditions to capture the flow physics inside the inlet. The following section provides an elaboration on the description of flow equations and turbulence modelling.

5.5.1 Reynolds Averaged Navier-Stokes (RANS) equations

The flow of air through the inlet is governed by the 3 fundamental laws of conservation:

- a) *Conservation of Mass*: Mass can neither be created nor destroyed during the process
- b) *Conservation of Momentum*: For two objects in a closed system, interacting with each other, the total momentum is constant. From Newton's third law perspective, the momentum lost by one object is equal to the momentum gained by the other.
- c) *Conservation of Energy*: Energy cannot be created nor destroyed in an isolated system. This means that the total energy of an isolated system remains constant.

The mathematical manifestation of these laws is given by the Continuity equation, Momentum equation and the Energy equation. More commonly known as the Navier-Stokes equations, they require discretization for smaller volumes and cannot be solved directly. This discretization method is known as the Finite Volume Method, which is also the underlying discretization approach in the CFX software package. Different types of elements such as hexahedrals, prisms, tetrahedrals, wedges are used to create the unstructured domain [46]. The Navier-Stokes equations are shown in equation 4.01 (Continuity Equation), equation 4.02, 4.03 and 4.04 (Momentum Equations) and equation 4.05 (Energy Equation).

$$\frac{\partial \rho}{\partial t} + \nabla \cdot (\rho b f V) = 0 \quad (4.01)$$

$$\frac{\partial(\rho u)}{\partial t} + \nabla \cdot (\rho u V) = -\frac{\partial p}{\partial x} + \rho f_x \quad (4.02)$$

$$\frac{\partial(\rho v)}{\partial t} + \nabla \cdot (\rho v V) = -\frac{\partial p}{\partial y} + \rho f_y \quad (4.03)$$

$$\frac{\partial(\rho w)}{\partial t} + \nabla \cdot (\rho w V) = -\frac{\partial p}{\partial z} + \rho f_z \quad (4.04)$$

$$\frac{\partial}{\partial t} \left[\rho \left(e + \frac{V^2}{2} \right) \right] + \nabla \cdot \left[\rho \left(e + \frac{v^2}{2} \right) V \right] = \rho \dot{q} - \frac{\partial(\rho u p)}{\partial x} - \frac{\partial(\rho v p)}{\partial y} - \frac{\partial(\rho w p)}{\partial z} + p f \cdot V \quad (4.05)$$

In the equations shown above, t is time ρ is the density of air, u velocity in x-direction, v is velocity in y-direction, w is velocity in z-direction, f is body force, V is the velocity vector and p is the pressure.

5.5.2 Turbulence Modelling

Various kinds of turbulence models are available for accurate approximation of the complex flow phenomenon namely Spalart-Allmaras model, k- ϵ model, k- ω model and the Shear Stress Transport (SST) model. k- ϵ model is a more widely used turbulence model that relatively accurately captures the boundary layer flow, accounts for compressible and viscous effects. Standard k- ϵ model was used for modelling the turbulence for the inlet testing.

The k- ϵ model consists of 2 transport equations which describe the turbulence:

- *Turbulent Kinetic Energy* (k) : determines the energy in the turbulence
- *Turbulence Dissipation Rate* (ϵ): determines the rate of dissipation of the turbulent kinetic energy

5.6 Mesh Topology

In the first phase of the thesis, the geometry and grids were created using Reinier's code written in ParaPy language [50], since a large number of geometries and grids were required to test the influence of geometrical parameters on results and study the flow physics inside the ducts. In the second phase of the thesis, geometries were created using splines in CATIA and the unstructured meshes were created in ICEM CFD. Varying combinations of length, height and aspect ratio cases were tested to analyse the influence of these geometrical parameters on the results at the AIP. The following sections will elaborate on the general factors that affect mesh topology, the mesh topology of the inlet configurations and boundary conditions.

5.6.1 Factors Affecting Mesh Topology

There are a number of parameters that affect the topology of a grid. Based on variations in the values of these parameters, factors like grid size, number of elements, quality of a mesh, etc. are affected. These parameters are described as follows:

1. **y-plus** (y^+): It is known as the non-dimensional wall distance and is described by equation (4.1):

$$y^+ = \frac{y\sqrt{\rho\tau_w}}{\mu} \quad (4.1)$$

Here, μ is the dynamic viscosity of air, τ_w is shear stress and ρ is the density of air.

It is physically the distance in the boundary layer from the wall to the end of the layer closest to the wall. The main reason for using the wall function is because there are lack of mesh points near the wall region. A smaller value of y-plus signifies a finer mesh in the region. If y-plus value is increased, the nodes in the layer closest to the wall increase in thickness and hence make the mesh coarser, which makes it difficult to capture the flow characteristics accurately in the boundary layer region.

2. **Local edge length:** It is the length of the mesh cells at the walls. Decreasing the local length increases the number of elements in the mesh as the wall region is now divided into more number of nodes and each node increases from wall region to core region through a growth rate (described in the next point). Similarly, increasing the local length makes the mesh coarser and decreases the number of elements in the mesh.
3. **Growth rate:** It is the rate by which the element thicknesses grow from the wall to the core region (in the s-duct in this case). The S-Ducts tested in this thesis are meshed fine near the walls and coarser in the central core region. The smaller nodes at the walls grow by a certain rate in thickness towards the core region. Growth rate affects the number of elements in the mesh like the local edge length. Decreasing the growth rate signifies higher number of elements. A low value of growth rate implies very fine mesh near the walls and very coarse mesh in the core region. This growth of cell sizes from wall region to central core region can be seen in Fig 40:

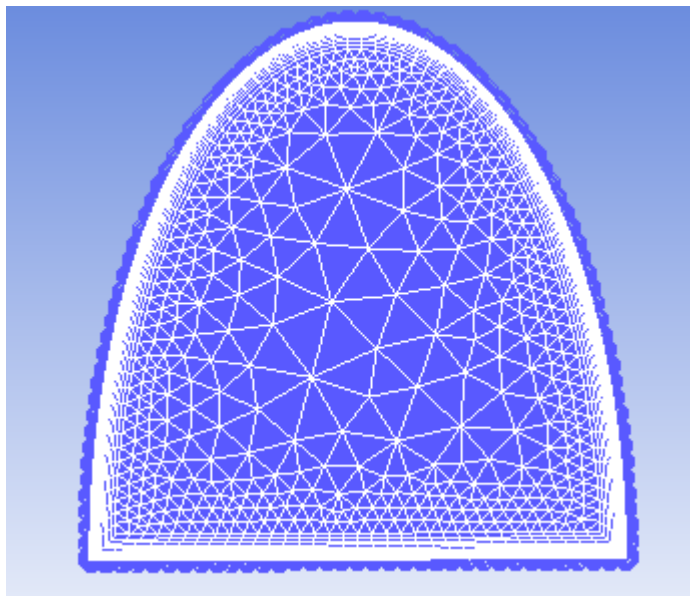


Figure 40: Mesh topology at the inlet face

4. **Fineness:** This is the growth rate of the unstructured core region. The mesh in the S-Ducts is structured at the walls and divided into a number of layers and the core region in the center has an unstructured mesh. Increasing the fineness increases the number of elements in the core region. However, increasing the fineness in the core region can also increase the skewness of the first tetrahedral elements closest to the layer farthest from the wall. This might affect mesh quality and hence the accuracy of the results.
5. **Number of layers:** The structured wall region is divided into a number of layers to capture the thick boundary layer being ingested into the intake. Most cases tested in this thesis consist of 17 layers near the wall region. This is an important factor when the flow characteristics at the wall region are significant. In this case, a thick boundary layer is ingested inside the inlet and to accurately capture the boundary layer ingestion, a certain number of layers are created in the structured wall region. These layers are shown in Fig 41.

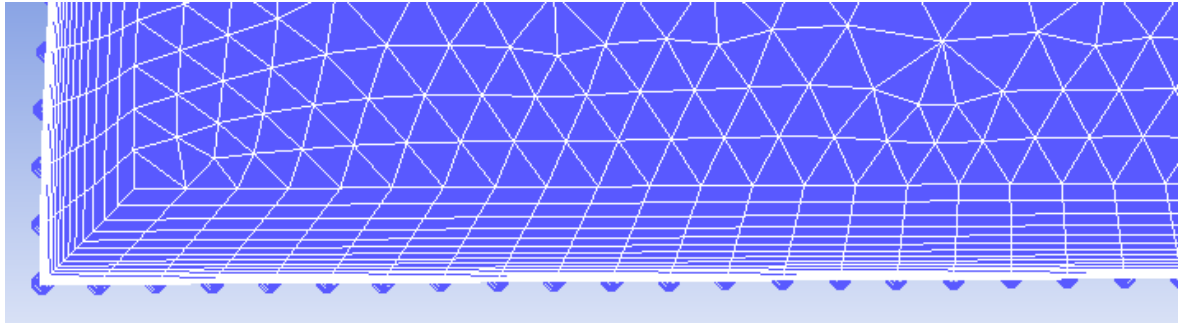


Figure 41: Layers in the structured wall region at the bottom part of the inlet face

5.6.2 Mesh Topology of the Tested Inlet Configurations

The mesh used in this thesis is a hybrid mesh with structured wall region and unstructured core region containing approximately 600,000 elements for the smallest duct and as the length, height and aspect ratio increased, the size of the domain also increased, thereby increasing the total number of elements. It can be seen from figures 40 and 41 in previous section and also Figure 42 that the wall region of the inlet is meshed using prismatic layers containing tetrahedral elements and the core region is an unstructured region with triangular cells. This was mainly done in order to capture the boundary layer ingestion as accurately as possible. Since there is significant ingestion of fuselage boundary layer through the inlet, a structured wall region would accurately describe the flow inside the S-Duct.

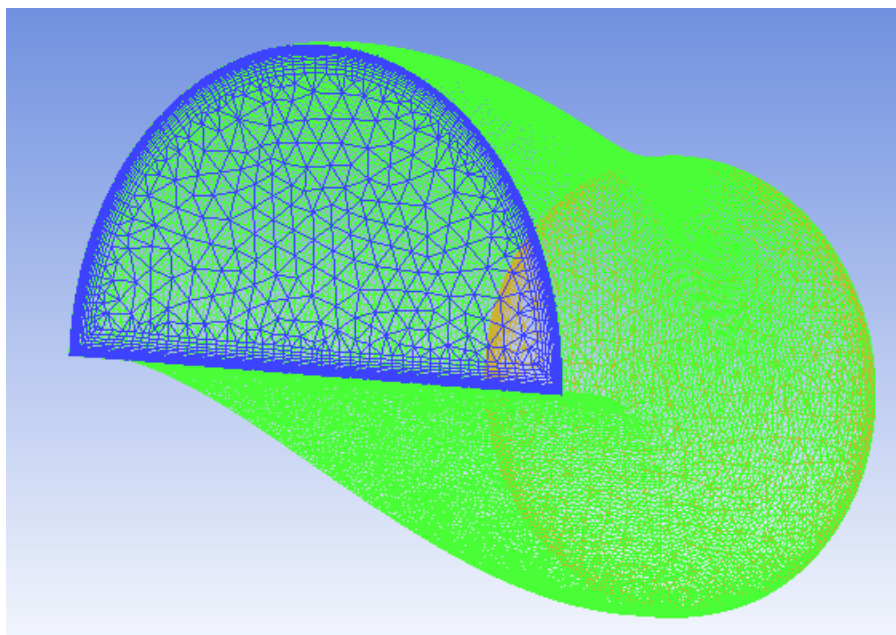


Figure 42: Mesh topology for an inlet configuration

In addition to creating the mesh, checking the mesh quality provides vital information about the sensitivity of a mesh to divergence. An unstructured mesh is good for handling complex configurations, whereas a structured mesh is generally better in terms of quality. When the grid lines are aligned with the flow, the accuracy of the solution is enhanced.

Mesh quality is mainly described by 3 factors:

- Aspect ratio
- Skewness
- Smoothness

ICEM CFD provides some options to smoothen the mesh for better mesh quality. A number of smoothing iterations were given to every mesh to improve the quality. The 3 factors affecting mesh quality are shown in Fig 43 for clarity.

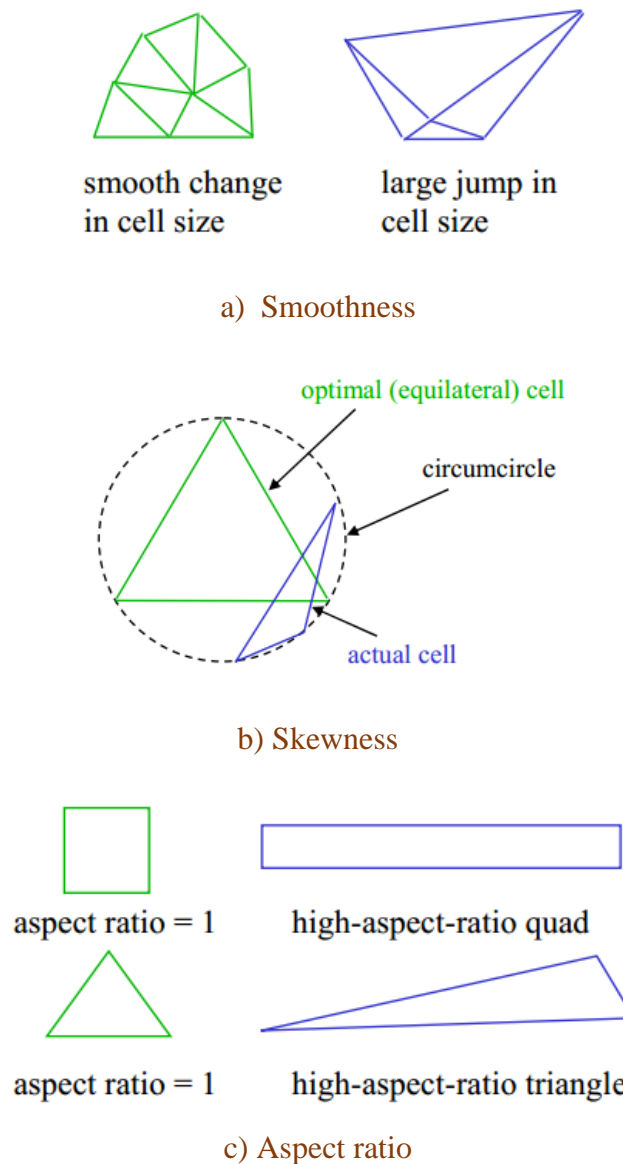


Figure 43: Factors defining mesh quality [47]

5.6.3 Boundary Conditions

The boundary conditions for the inlet configurations are defined as follows:

- a) **Inlet:** The entry of the S-Duct at the semi-elliptical face (shown in Fig 42) is defined as the inlet. The velocity profile at the location, where the inlet will be embedded, is obtained from the results of the BWB fuselage simulation and applied as inlet to the semi-elliptical entry face of the inlet.
- b) **Outlet:** The circular face at the exit of the S-Duct is defined as the outlet for the inlet configurations. This circular face is the engine fan-face or AIP. Some of the critical effects of flow inside the S-Duct will be assessed based on results of total pressure distortion and Mach number at the engine fan-face. The diameter of the engine fan face is constant.
- c) **Wall:** Between the inlet and the outlet, solid wall condition is defined for the cylindrical surface. Flow is considered adiabatic, which means no heat transfer is assumed. The wall boundary condition assumed is a no-slip conditions. This means that the fluid velocity at the boundary, will be zero. In other words, it dictates the presence of boundary layer. Hence the velocity increases from zero at wall region to a finite value at core region. Also, there is no normal flow at the boundaries (Neumann boundary condition).

5.6.4 Geometry and Mesh Generation using ParaPy

As mentioned in the introduction of Section 5.6, the first phase of the thesis required generation of a number of geometries and meshes to be tested, which was not possible using CATIA or ICEM CFD. Codes were written in ParaPy language by Reinier [50] [Appendix F] to generate these geometries and grids.

The ParaPy language is a high level form of Python programming language, which serves as the knowledge based engineering framework for Python. ParaPy makes easy the development of software tools for automation of routine engineering tasks, which otherwise require large amount of time like CAD modelling, grid generation, CAE pre-processing and multi-disciplinary design optimization (MDO). However, these are only some of the many applications of ParaPy. ParaPy makes it straightforward to codify generic, parametric engineering models and succeeds in capturing the engineering intent behind these models. Since ParaPy is being built on top of Python, it uses a number of Python's intrinsic features like readability, a large community, a vast range of built-in and 3rd-party libraries and online resources. ParaPy replaces the manual drafting in CAD softwares by using the industrial grade open source OpenCascade geometry kernel, which allows the automations of the generation of 3D geometries by coding. In addition to this, integration with the Salome meshing suite provides the automatic generation of grids for the created geometries to be fed into solvers for analysis. Any changes in the geometry or grid are automatically updated by intelligent caching and dependency tracking algorithms. ParaPy provides a high level of flexibility and generalization to the geometries and grids it generates. This allows it to serve as the central design representation that is used by other discipline-specific simulation tools to retrieve information from during MDO studies [50].

Figure A shows a standard S-Duct model created in ParaPy using only 134 lines of code [See Appendix F]. The duct shown in this figure has a length of 4.85m, height of 0.3m and an inlet aspect ratio of 1.75.

Figure B shows the hybrid grid generated using ParaPy for the model shown in Figure A using only 53 lines of code [See Appendix F]. The grid comprises nearly half a million cells, a structured boundary layer region with 17 layers to accurately capture the boundary layer ingestion effect and an unstructured core region.

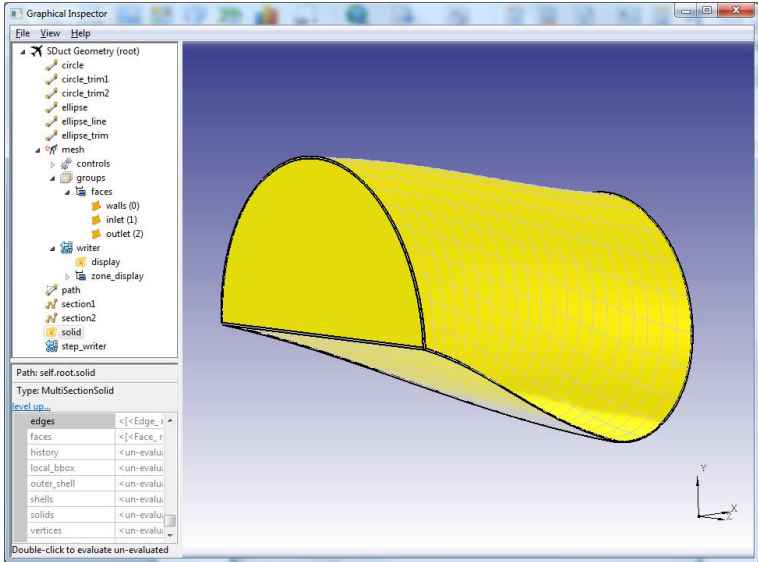


Figure A: S-Duct model generated using ParaPy [50]

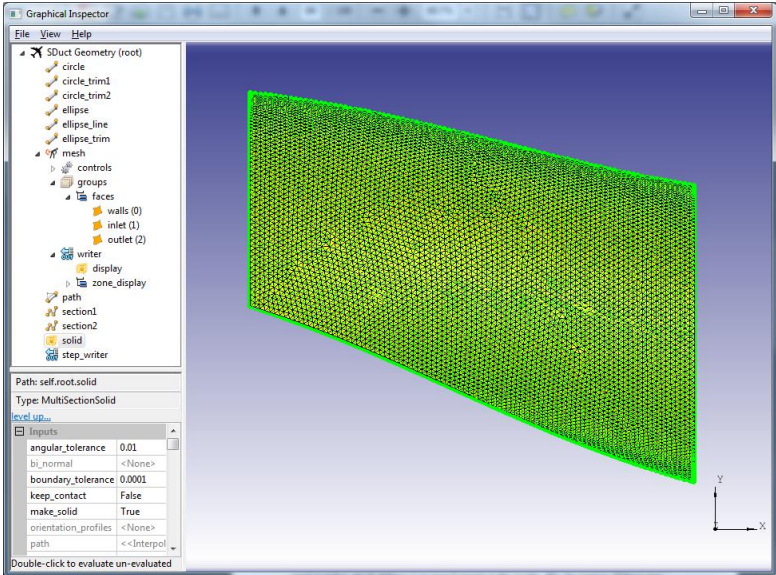


Figure B: Grid generated using ParaPy [50]

5.7 Testing Procedure

The entire testing procedure is divided into 2 stages. The first stage concerns the CFD analysis of a 3D BWB aircraft and the second stage comprises of inlet configuration testing. These 2 stages are described in detail in the following sub-sections.

5.7.1 First Stage

The first stage of testing consisted of a 3D model of a BWB aircraft in clean configuration (without engines). A flow simulation was conducted in order to obtain velocity profiles over aft fuselage at different locations, where the inlet will be embedded. These velocity profiles were applied as inlet boundary conditions to the ducts tested in Stage 2 of testing.

The S-Ducts were tested separately using BWB velocity profiles in order to save computational time, as testing entire BWB configuration with embedded engines for every variation of length, height and aspect ratio was not a feasible option. Figures 44 and 45 show the BWB aircraft in clean configuration and applied velocity profiles at the inlets of the ducts, respectively.

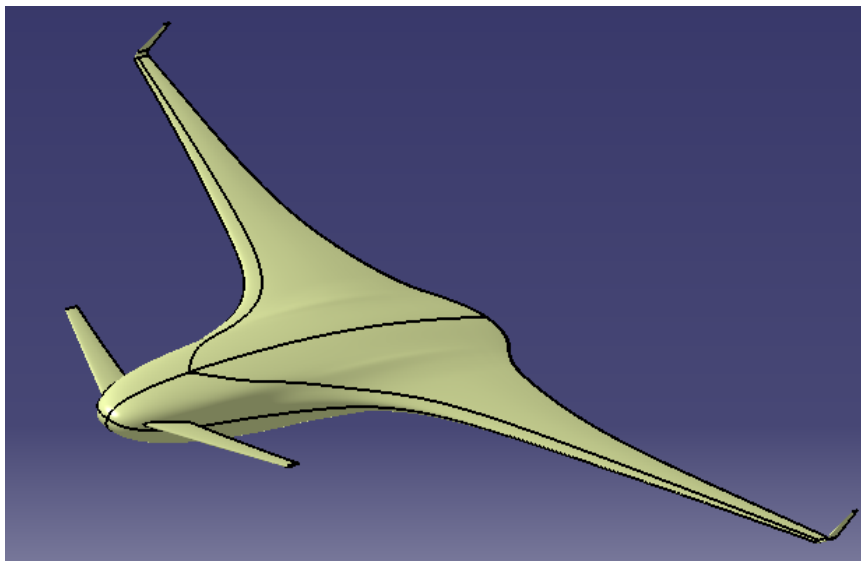


Figure 44: BWB in clean configuration (without engines)

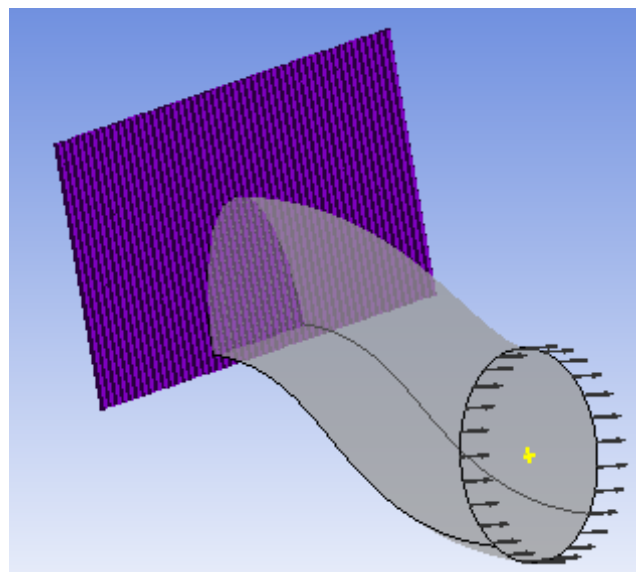


Figure 45: Velocity profile applied as inlet to S-Duct

5.7.2 Second Stage

A large number of simulations were carried out based on combinations of varying aspect ratio, height and length of the inlet to accurately determine the effect of these parameters on the results. Initially, the tests were only carried out specifically for S-Duct inlets. However, as the testing progressed, new configurations were investigated

First, the tests were carried out for the shortest duct length (4.85m) and a given height value (1.052m) and changes were only made in the value of aspect ratio so that the influence on results would be only due to the sole effect of aspect ratio. As shown in Table 2 in Section 5.3.2, aspect ratio was varied from 1 to 2.5. This meant that the inlet became wider as the aspect ratio was increased and consequently the amount of boundary layer ingestion increased. Variation in aspect ratio is critical in understanding the actual effect of increasing percentage of BLI. Furthermore, as discussed before, increasing the aspect ratio also reduces wake dissipation as larger amount of the aircraft wake is being ingested.

After an optimum value of aspect ratio was chosen, height was varied keeping the same duct length and the chosen aspect ratio value. And finally, after a conclusion on the value of height, variation in length indicated the optimum length of the duct required to achieve minimized losses in terms of pressure recovery, distortion and wetted area.

5.7.3 Other Configurations Used For Testing

In addition to S-Ducts, 3 other configurations were investigated to understand the flow physics inside the inlet to a higher level and also to understand if the results improve as a consequence of these configuration changes. The standard S-Duct and the 3 new configurations are shown in Figure 46.

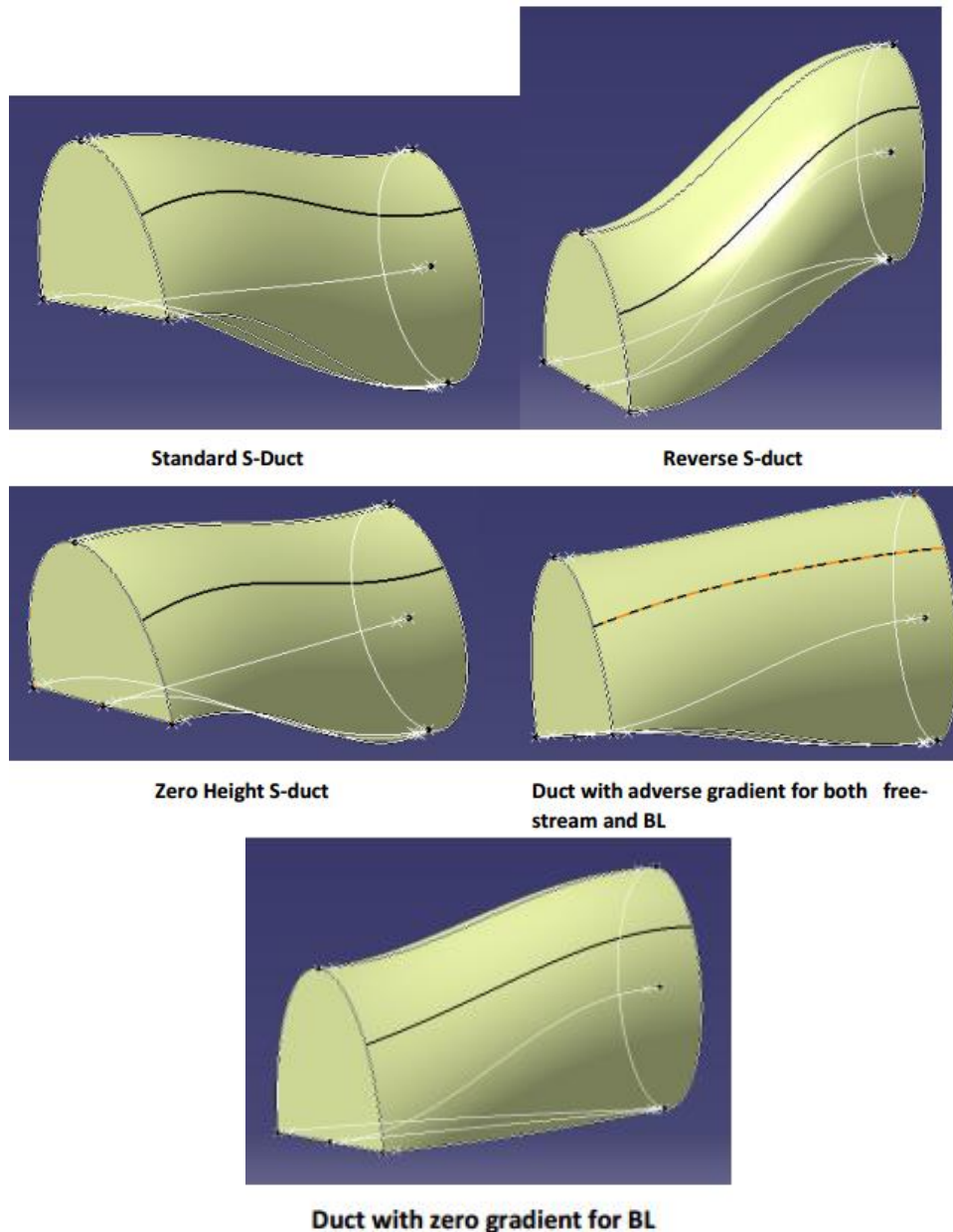


Figure 46: Different configurations used for testing

The standard S-Duct is a configuration that came as a result of the testing in second stage (described in Section 5.7.2). The other configurations included reverse S-Duct (to check the effect of accelerating boundary layer), zero height S-Duct (with centers of the inlet and outlet on the same horizontal location), an inlet with fan directly in front of the inlet so there is adverse pressure gradient both for the boundary layer and freestream and finally, a duct with no gradient for the ingested boundary layer. The reason for doing this is elaborated in detail in the next chapter (Results). Some final changes were made to these configurations at the end to obtain the final design. The analysis of the final design is also presented in the next chapter.

To compile all the stages of testing for a better understanding, Fig 47a shows the overall framework of the testing procedure.

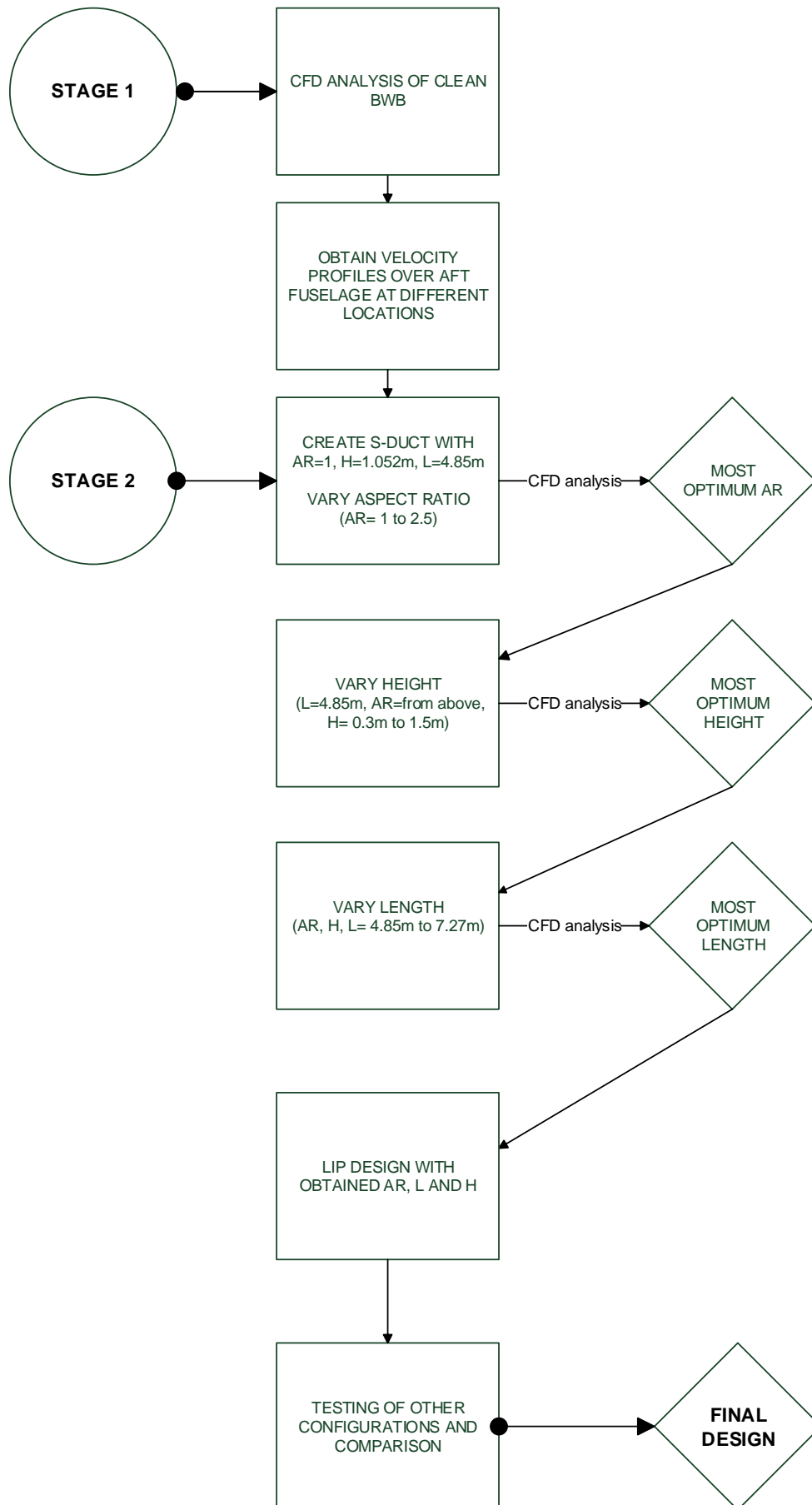


Figure 47(a): Framework for testing

5.8 Validation

There have been a number of studies conducted in the field of BLI on a BWB as is described in detail in the previous chapters. The research work carried out for this thesis is focussed only on the computational analysis of the effects of BLI on inlet performance on a BWB. Since no experimental simulations were conducted, it is not possible to validate the results for the same geometry used in this thesis. However, research work carried out in the past presents a number of results that can be used to validate the results of the current thesis work. The 2 major parameters that are chosen as criteria to judge inlet performance are total pressure recovery and total pressure distortion.

A.P. Plas [8] presented a paper on the performance of an embedded propulsion system with BLI. At similar operating conditions as in this thesis and using an S-Duct inlet, following results were obtained from the analysis shown in Figures 47b and 47c.

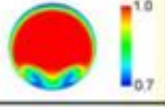
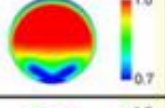
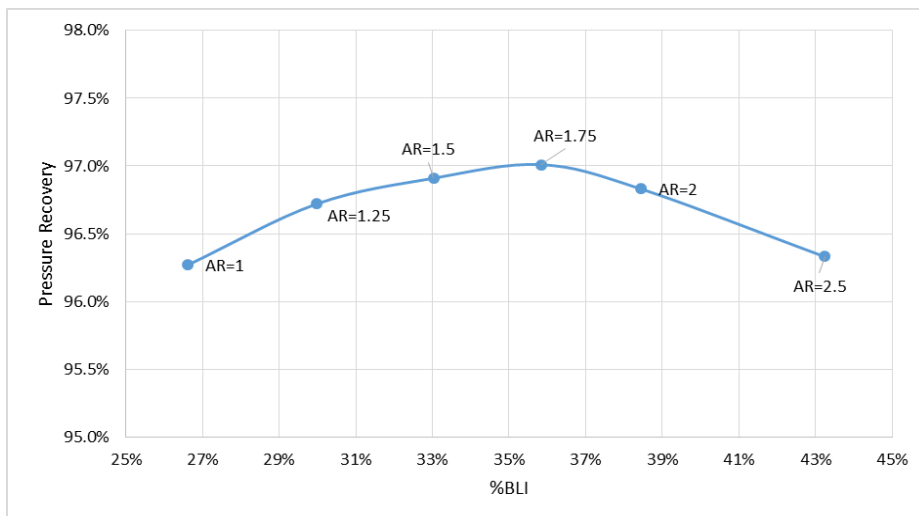
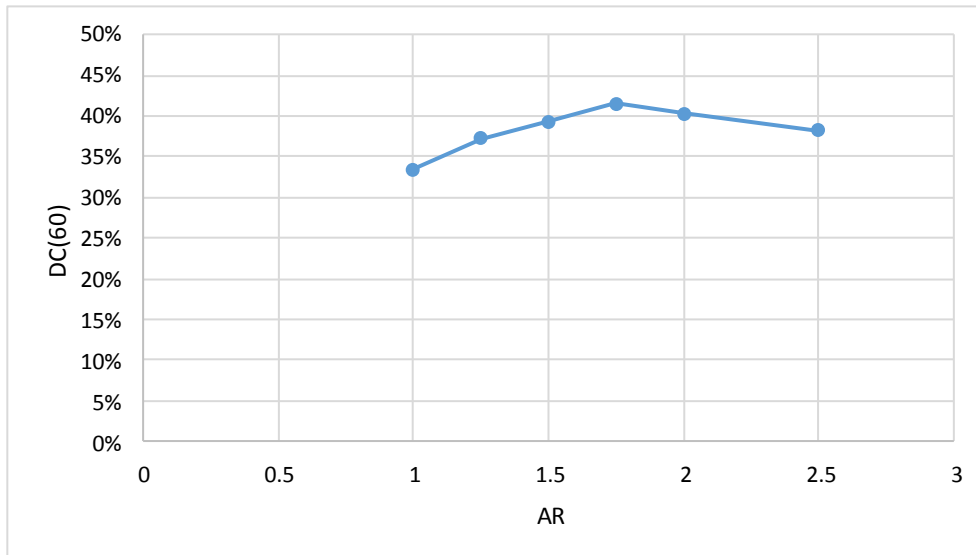
BLI	PR	DC(60)	Contours of P_t
10%	0.962	0.249	
20%	0.955	0.324	
33%	0.941	0.418	
45%	0.930	0.474	
59%	0.915	0.512	

Figure 47(b): Effect of %BLI on PR and DC(60) [8]



Variation of pressure recovery with %BLI (Result from the current thesis work)



Variation of DC₆₀ with %BLI (Result from the current thesis work)

From Figure 47b and the plots of pressure recovery and distortion coefficient variation with %BLI, it can be seen that the pressure recovery and distortion coefficient results for this thesis show comparable values to those of A.P. Plas [8].

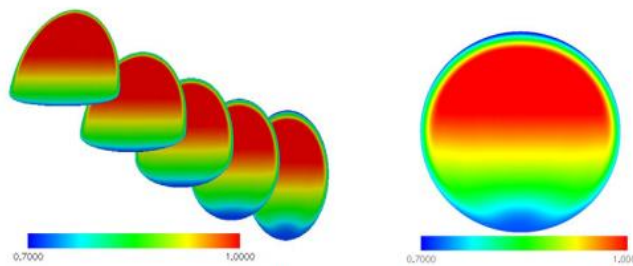


Figure A2. Total pressure contours at different sections (left) and fan face (right), PR = 0.946.

Figure 47(c): Flow Development inside the S-Duct [8]

Figure 47b shows the effect of increasing BLI on inlet performance. It is seen that increasing the BLI decreases total pressure recovery for a constant duct height, inlet aspect ratio and duct length and the distortion coefficient value increases significantly.

A similar study conducted at NASA by B.L. Berrier [17] produced the following plots for total pressure recovery and the circumferential distortion descriptor DPCPavg.

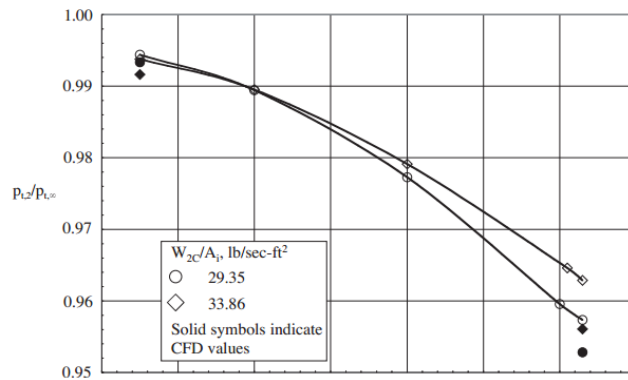


Figure 47(d): Variation of Pressure Recovery with M [17]

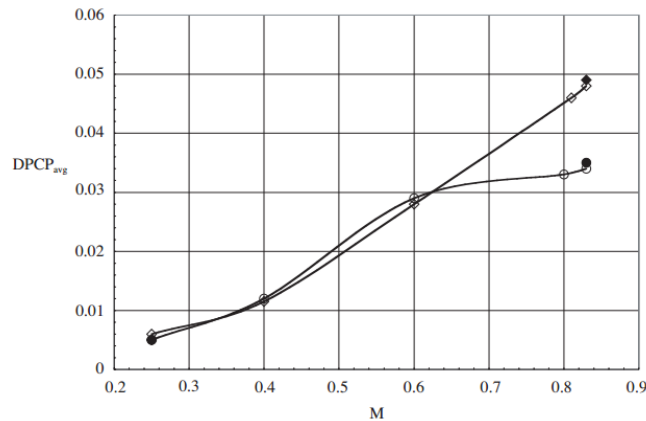


Figure 47(e): Variation of Circumferential Distortion Descriptor with M [17]

Figures above show that the pressure recovery vary from 95.5% to 99.5% approximately as the Mach number is varied from 0.25 to 0.85. The Mach number used in the current thesis work is 0.82 for the free-stream. Judging from the plots above, a pressure recovery value of nearly 96.5% is achieved by B.L. Berrier for $M=0.82$, which is comparable to the results of the current thesis. For different duct configurations, the present thesis work produced results of pressure recovery ranging from 95% to 98%.

B.H. Anderson [49] came up with the results shown in the following figures for total pressure recovery and DC(60) at 0 angle of attack and a throat Mach number of 0.7. These figures clearly show the value of DC(60) reaches around 45% for $M_t=0.7$ and $AOA=0$ degrees.

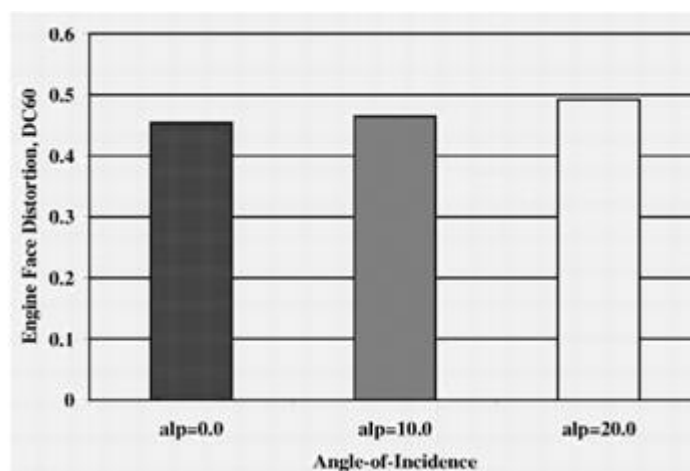
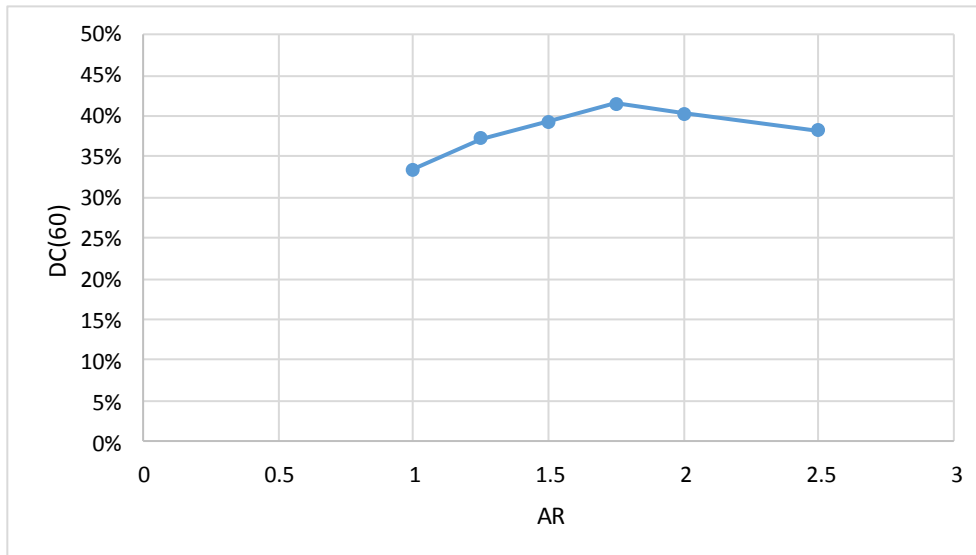


Figure 47(f): Variation of DC(60) with angle of incidence [49]



Variation of DC₆₀ with %BLI (Result from the current thesis work)

The plot above shows the results for the current thesis. It is seen that the inlet with AR=1.75 has a DC(60) value of approx. 43%, which is comparable to Anderson's DC(60) value of 45% for 0 degree angle of attack and throat Mach number of 0.7, which is also seen in Figure 47g.

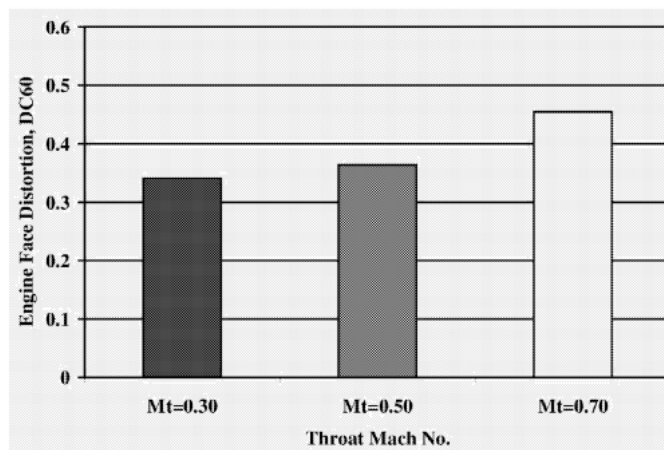


Figure 47(g): Variation of DC(60) with throat M [49]

These results in addition to the ones provided in the first four chapters provide a basis for validation of the results obtained in the current thesis work. However, accurate validation can only be performed if experimental tests are conducted on the scaled model of the BWB used in this research work.

6

Results

This chapter focuses on the results obtained from the various simulations conducted as described in the previous chapter. First part of this chapter deals with the results of the testing conducted in Stage 1 as described in Section 5.7.1. The second part of this chapter provides an analysis of the results of the testing conducted in Stage 2 as described in Section 5.7.2. Following this, discussion of the results of testing on other configurations and nacelle lip is presented. After analysing these results, some variations are made in the geometry of the inlet to further minimize losses and obtain a final design.

6.1 Clean Blended Wing Body

As shown in Fig 44, Stage 1 of testing comprised of flow analysis of a BWB in clean configuration in order to obtain 3D velocity profile over aft fuselage, where the inlets will be embedded. This was mainly done to shorten the computational time and the required computational power. The length of the BWB fuselage is approximately 46m. Since four length cases were tested ($L = 4.85\text{m}$, 5.65m , 6.46m and 7.27m), four velocity profiles were required from the BWB results. The location of the engine was fixed at the end of the fuselage based on the dimensions of the engine provided. This meant that the semi-elliptical entry face of the inlet with $L=4.85\text{m}$ will be more aft on the fuselage upper surface as compared to the entry face of the inlet with larger length, $L=7.27\text{m}$. So, the velocity profiles at different x-locations were different in magnitude. This also means that the Mach number at the entry of the inlet with $L=7.27\text{m}$ will be larger as compared to the one with $L=4.85\text{m}$ because of higher skin friction losses in the latter case since the flow traverses a larger distance over the fuselage in the case of $L=4.85\text{m}$.

Since the model of BWB is symmetric about the length of the fuselage (roll-axis), only half the geometry was meshed using a symmetry plane. The BWB model was meshed using an unstructured grid containing approximately 2.5 million elements with fine meshing near the wall of the BWB to capture the boundary layer flow accurately. Figures 48 and 49 show the 3D computational domain around the BWB and the zoomed in view of the BWB near the symmetry plane, respectively.

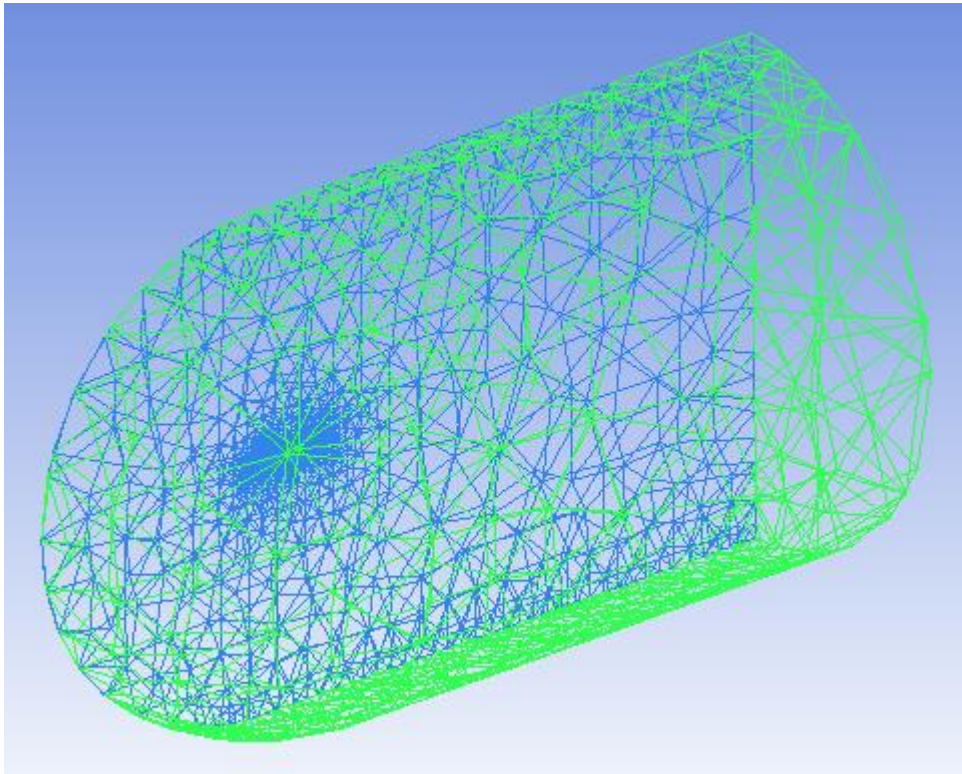


Figure 48: 3D computational domain around the BWB with unstructured mesh

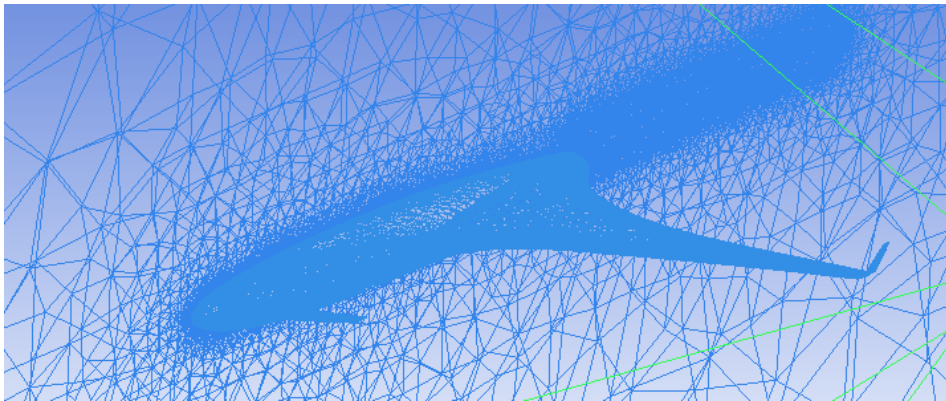


Figure 49: Meshed BWB at the symmetry plane

After the meshing was complete, boundary conditions were defined in the setup cell of ANSYS CFX Workbench. The BWB shown in Fig 49 was defined as wall with no-slip condition, symmetry was defined for the symmetry plane also visible in Fig 49 and inlet condition was defined for the rest of the boundary shown in green colour in Fig 48. Operating conditions for cruise were also inputted taking into account that the BWB will operate at cruise conditions (shown in Table 3 in Section 5.4). Following this, the solution was run. No convergence criteria was given and the solver was run until the residuals of mass and momentum stopped varying. The solver ran up till approximately 1600 iterations. This is shown in Fig 50.

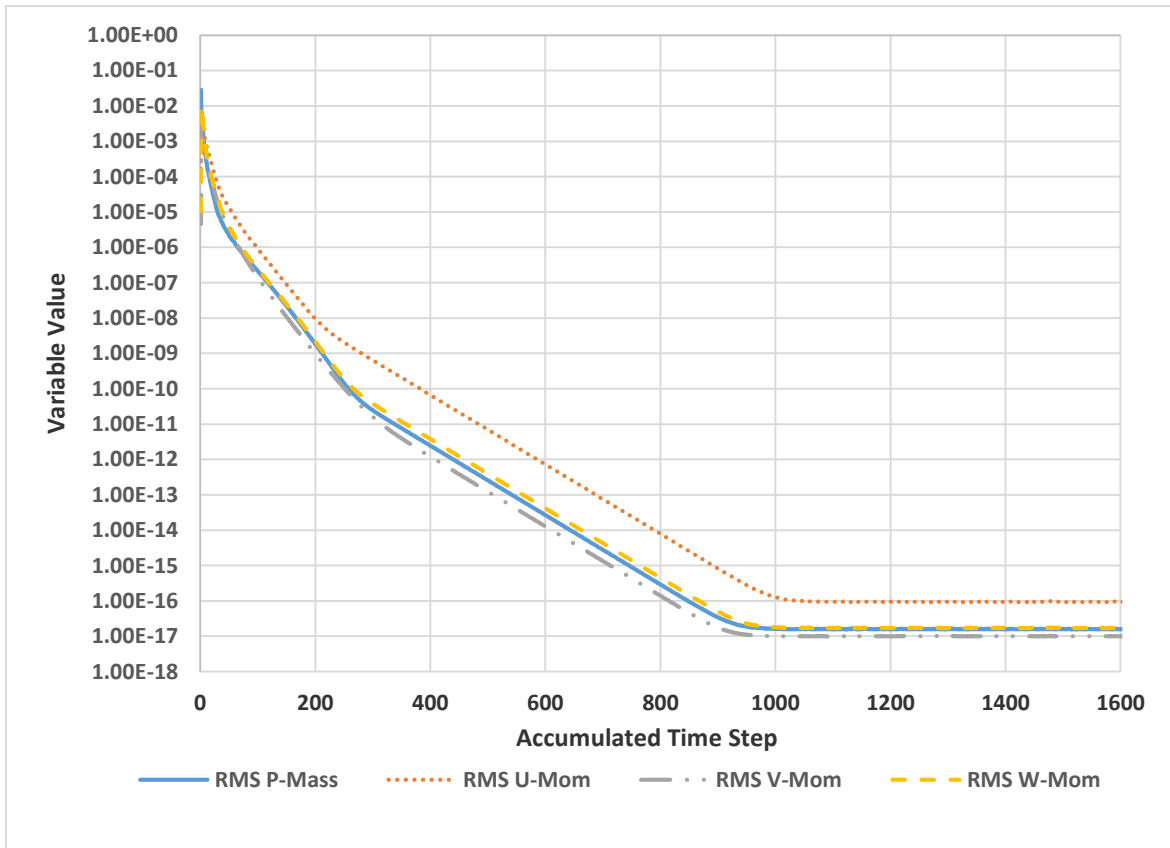


Figure 50: Mass and momentum residual history for clean BWB

Following this, results were obtained in the post-processor. The main objective of this simulation was to obtain the velocity profiles over aft fuselage. Fig 51 shows the velocity distribution over the BWB at the symmetry plane.

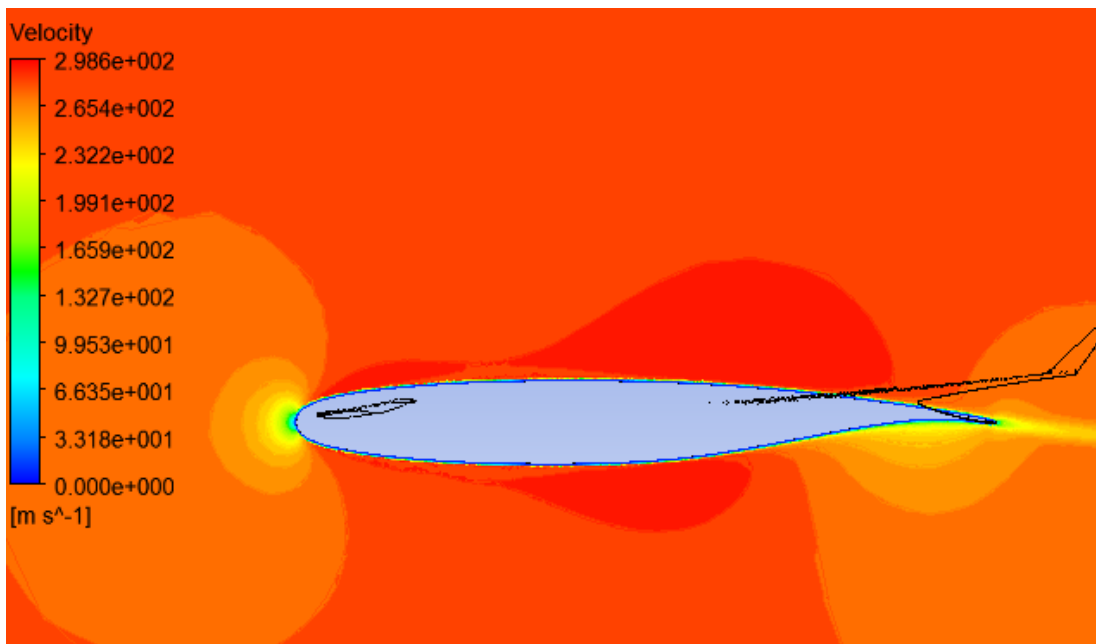


Figure 51: Velocity distribution over BWB

It can be seen from Fig 51 that the flow over the fuselage accelerates to a high value because of the curvature of the fuselage. However towards the aft of the fuselage, the flow velocity starts to decrease as the flow decelerates and the boundary layer (wake) becomes thicker. Fig 52 shows a sampling plane displaying the local velocity profile at a possible inlet integration location. Depending on the length of the inlet, the velocity profiles were obtained and exported to the CFX setups of the S-Ducts to be applied as inlet boundary condition for the same.

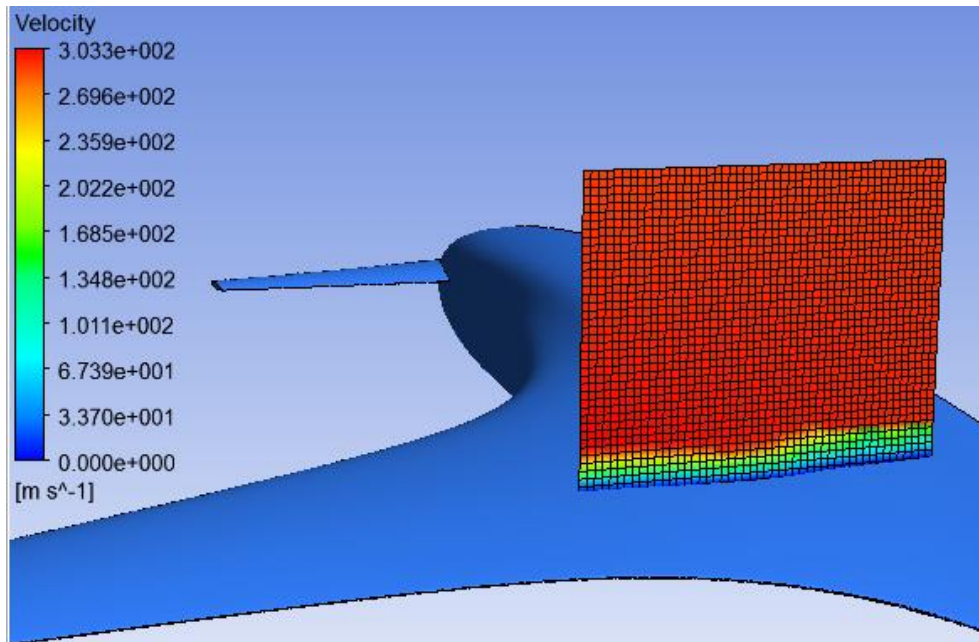


Figure 52: Velocity profile over aft fuselage of clean BWB

6.2 Influence of Inlet Aspect Ratio and BLI

First, the inlet aspect ratio was varied keeping the length and height of duct constant at $L=4.85\text{m}$ and $H=1.052\text{m}$. The shortest length duct was chosen for the initial testing in order to save computational time for tests that required understanding of the effects of aspect ratio and height on results. The inlet aspect ratio has a critical influence on the results as it dictates the amount of boundary layer ingested, which affects pressure recovery and distortion. As described in Section 5.3.1, a high aspect ratio indicates a wider and less high inlet, which means higher boundary layer is ingested into the intake. Consequently, distortion at the AIP increase due to higher low momentum flow being ingested. These effects are described in detail in this section.

These velocity profiles obtained from the clean BWB results were applied to the inlets with varying length, height and aspect ratios. Fig 53 shows the velocity distribution at the inlet faces for ducts with different aspect ratios.

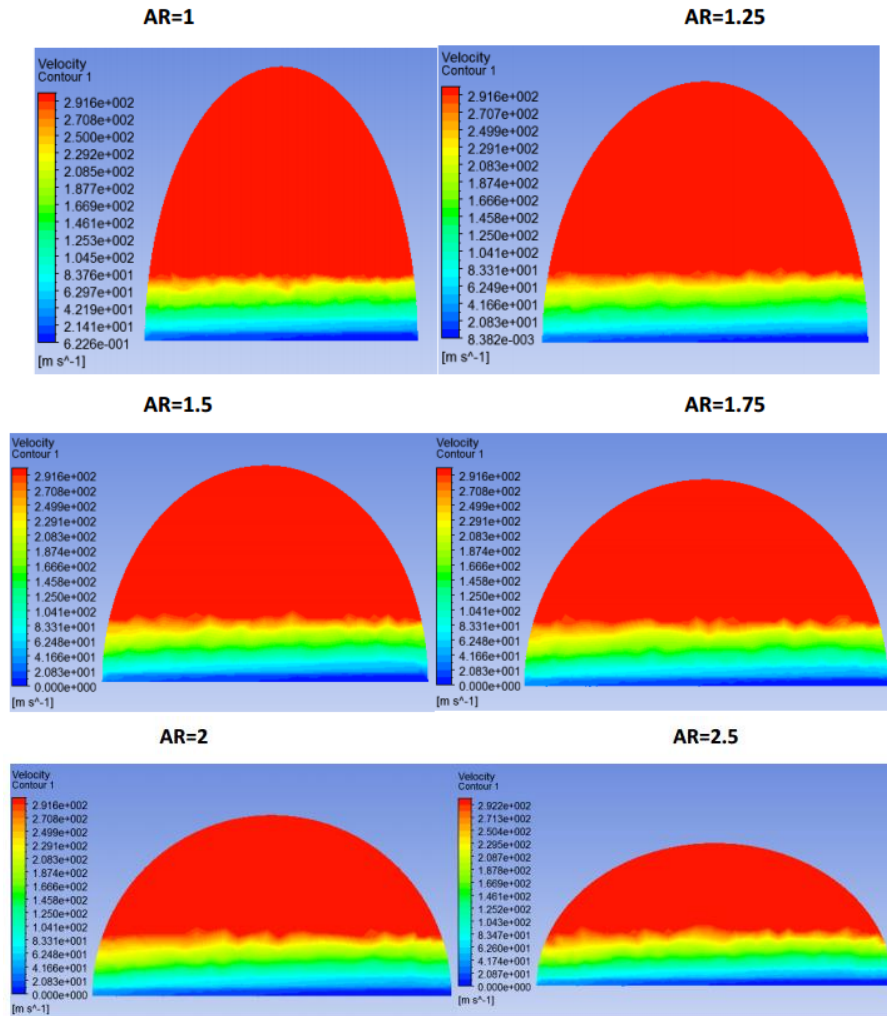


Figure 53: S-Duct inlet faces for different aspect ratios showing BLI

It is evident from Figure 53 that the higher the aspect ratio, the higher is the percentage of BLI as compared to free-stream. Figure 54 shows the variation of %BLI with increasing aspect ratio. The method for calculating %BLI is adapted from Lemmens [7].

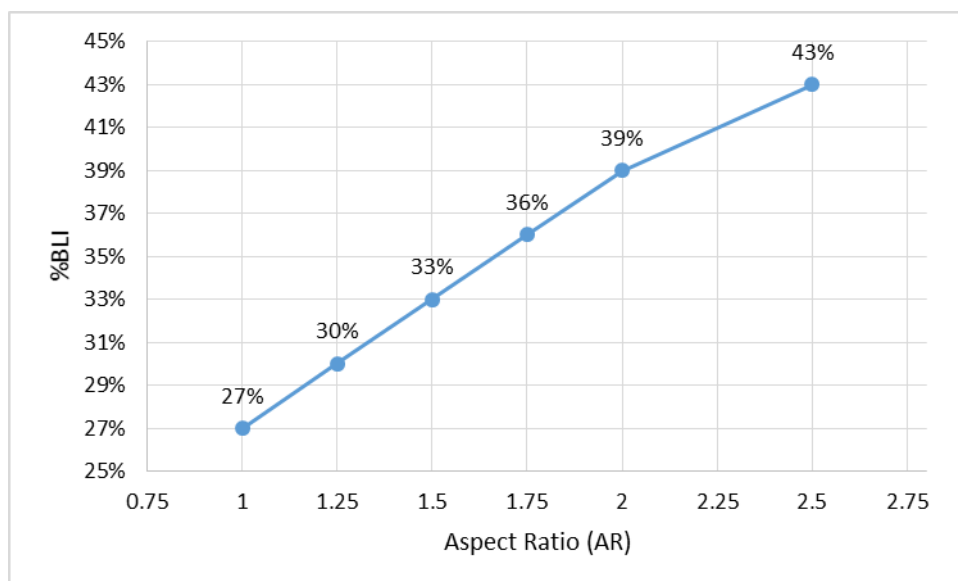


Figure 54: Variation of %BLI with increasing AR

6.2.1 Total pressure and x-Velocity Results at AIP

The testing was carried out on the S-Ducts for varying aspect ratios starting from AR=1. Fig 55 shows the results of total pressure and x-velocity obtained at the engine fan-face or AIP for AR=1.

AR=1

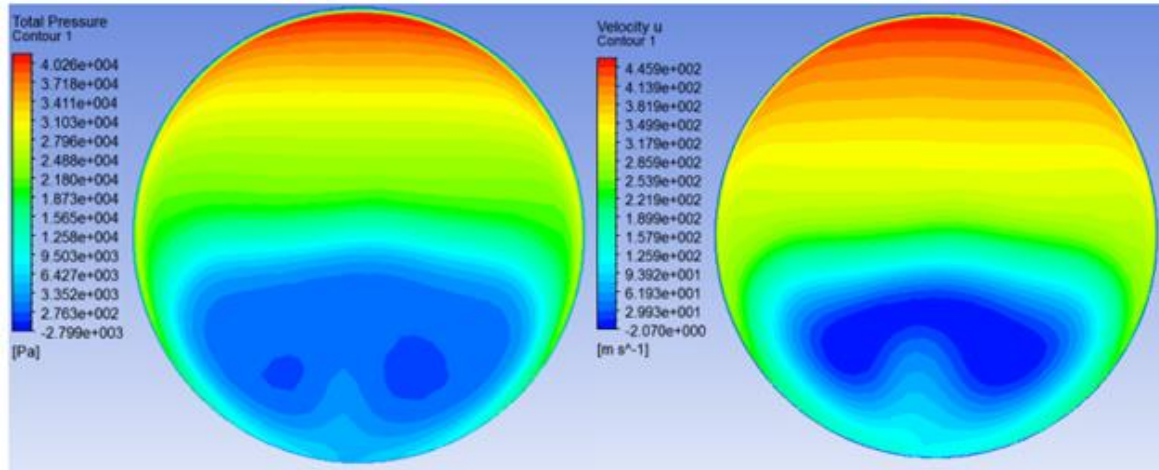


Figure 55: Total pressure and x-velocity contours at AIP for AR=1

Fig 55 clearly shows the effect of the formation of a vortex pair at the bottom of the S-Duct. This vortex pair is a part of the secondary flows formed at the second bend of the S-Duct due to the adverse pressure gradient experienced by the low momentum boundary layer, which easily separates and causes a region of recirculation. Since the freestream flow on the upper part of the S-Duct experience a favorable pressure gradient, it accelerates and a low static pressure region is created on the upper part. This low static pressure region lifts the slow moving boundary layer causing the formation of the vortex pair at the bottom of the S-Duct. This is shown in detail in Fig 56. The distorted total pressure distribution at the AIP will cause non-uniform loading of the fan, which can lead to vibrations of the blade and blade stall. Therefore, it is important to understand the cause of these secondary flows and make design improvements to minimize their formation.

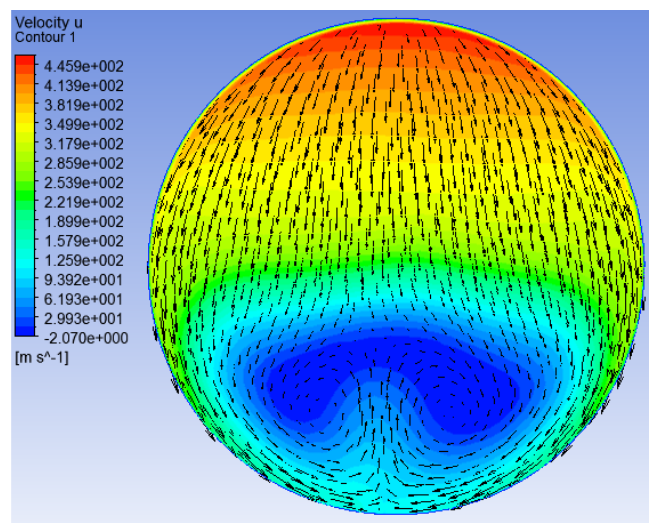


Figure 56: Tangential flow at the AIP

Fig 56 shows the negative velocity in the region of recirculation going as low as 2.07 m/s at the bottom of the S-Duct. This region of recirculation adversely affects the total pressure recovery and increases total pressure distortion at the AIP, as will be seen later in this section. It is also seen that the upper limit of x-velocity value is too large (445.9 m/s), which is a consequence of flow acceleration on the top part of the S-Duct. To provide a better understanding of how the flow accelerates at this part, Fig 57 depicts the streamlines over the x-velocity contours to show flow acceleration and point of separation.

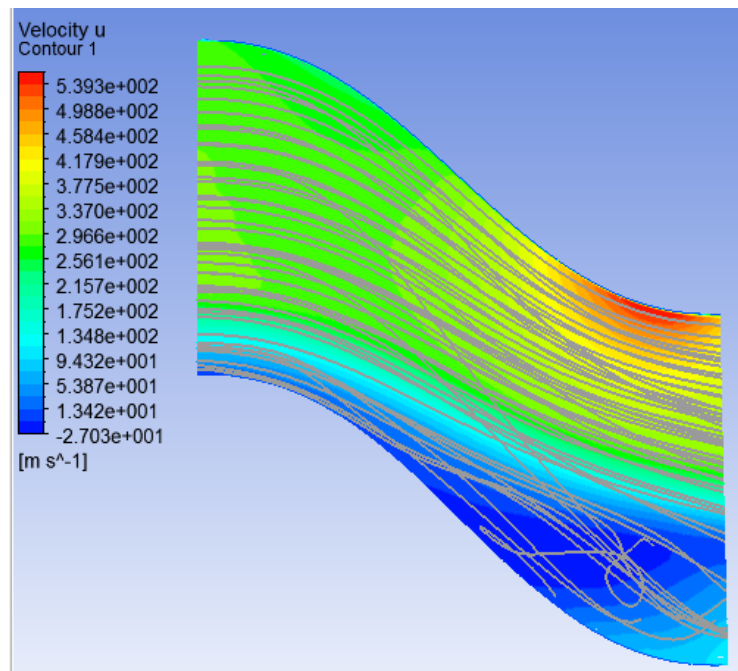


Figure 57: Streamlines at the mid-plane for AR=1

One reason for this extremely high velocity on the upper part of the duct is the long length of the semi-minor axis of the inlet face for AR=1, which is 3.08m. For low aspect ratios, the inlet face is higher and less wide (See Figure 53). And since the height is parameterized from center of inlet face to center of AIP and is constant while varying aspect ratio, the only variation in the curvature of the upper spline of the S-Duct comes from the length of the semi-minor axis of the inlet face. For high aspect ratios, the length of the semi-minor axis is low as compared to the length of the major axis of the inlet face, indicating a wider inlet face and hence larger amount of boundary layer ingestion. This shortening of semi-minor axis length of the inlet face with increasing aspect ratio in turn reduces the pressure gradient at the upper part of the S-Duct and flow acceleration reduces.

Figure 58 shows boundary layer separation and the region of negative velocity at the bottom part of the duct. The large semi-minor axis length of the inlet face can also be seen at the entry of the S-Duct at the left. The region of recirculation seen in Figure 58 can be reduced with careful selection of the aspect ratio value, by reducing height of duct, etc. which will be discussed in this chapter.

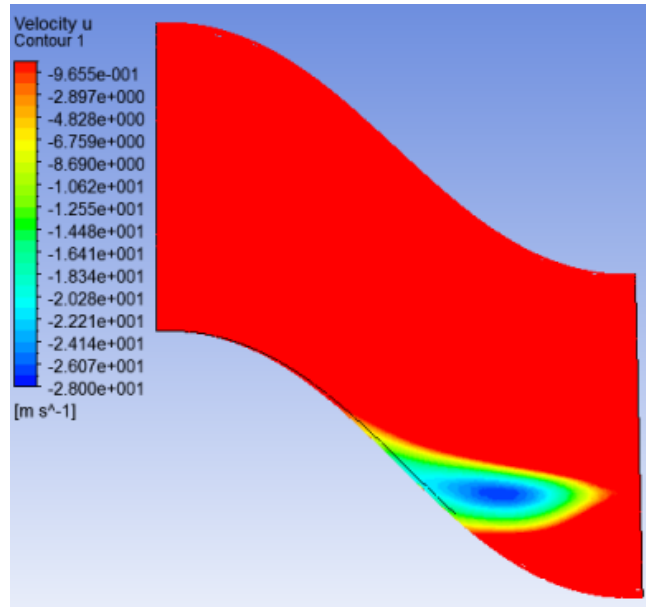


Figure 58: Mid-plane view of S-Duct (AR=1) showing recirculation region

To show the difference in upper spline curvature of S-Duct, Figure 59 shows the mid-plane view of the S-Duct with AR=2.5 (widest inlet with shortest semi-minor axis length).

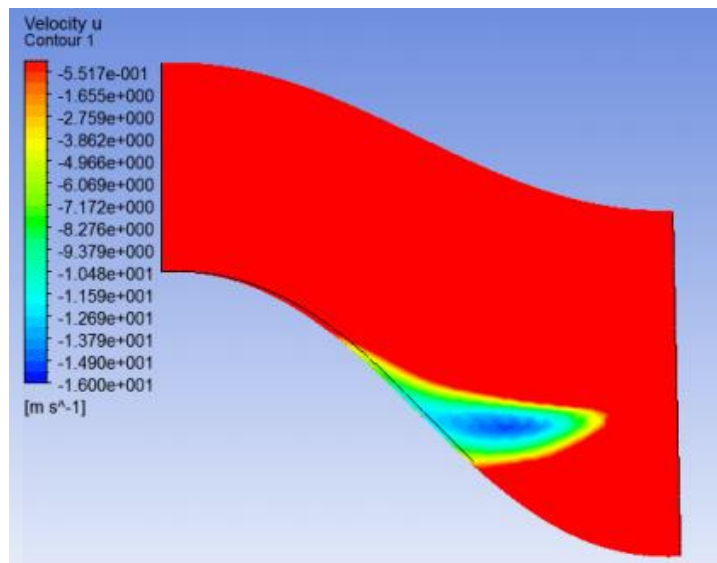
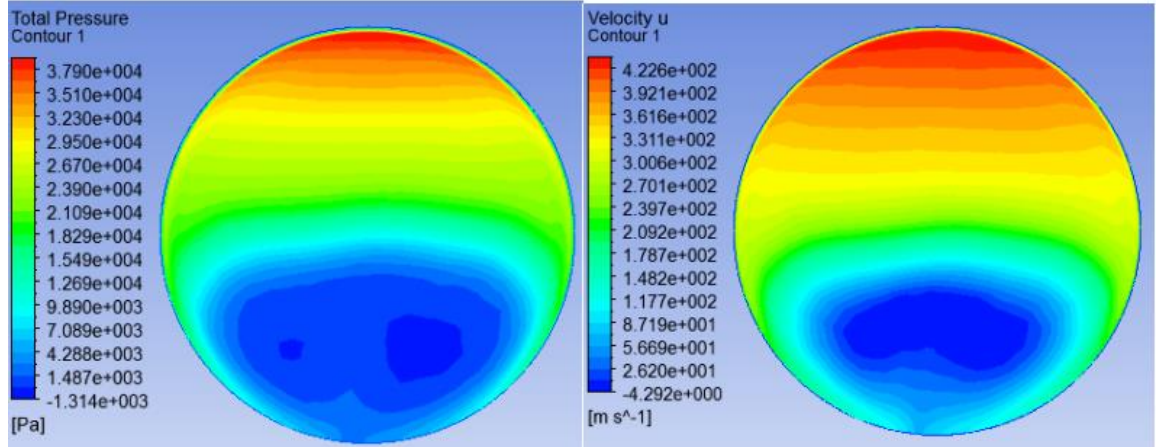


Figure 59: Mid-plane view of S-Duct with AR=2.5 showing recirculation region

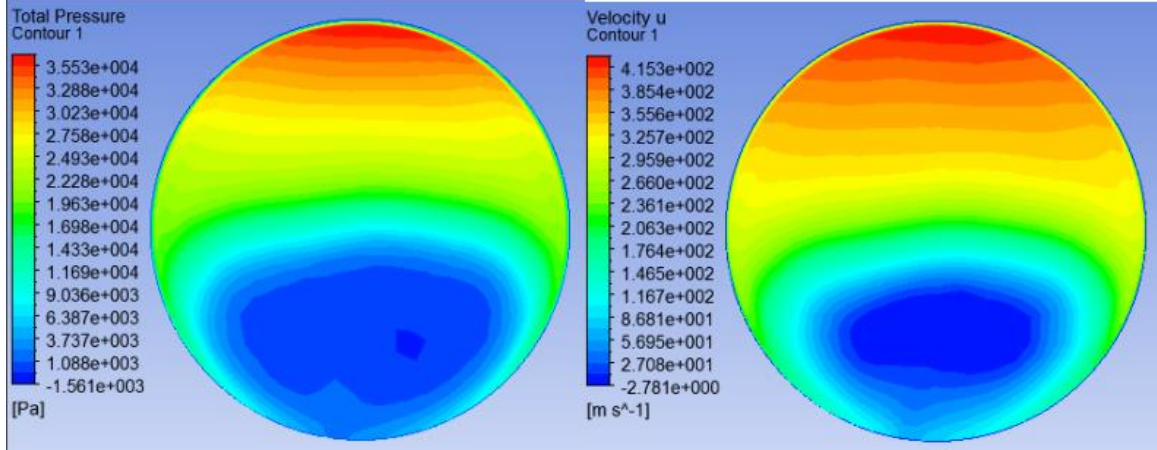
It can be seen from Figure 59 that the pressure gradient on the upper spline has considerably reduced with increased aspect ratio. This means that the flow on the upper wall of the duct does not accelerate as much as it does for the duct with AR=1. Hence, the static pressure region on the upper wall for AR=2.5 duct is not as low as for AR=1 duct. Therefore, the lowest value in the recirculation region in Figure 59 (-16 m/s) is less than in Figure 58 (-28 m/s) because the static pressure in the duct with AR=2.5 is not low enough to lift the boundary layer on the bottom wall to a considerable amount. However, aspect ratios as large as 2.5 are not desirable due to high pressure loss because of large ingestion of fuselage boundary layer and hence %BLI.

Total pressure and x-velocity results at the AIP for other inlet aspect ratios are shown in Figure 60 (a). It is evident that with increasing aspect ratio, the upper limit of x-velocity reduces due to reduced duct upper spline curvature, which in turn causes lower negative velocity on the bottom region of the s-duct as explained before.

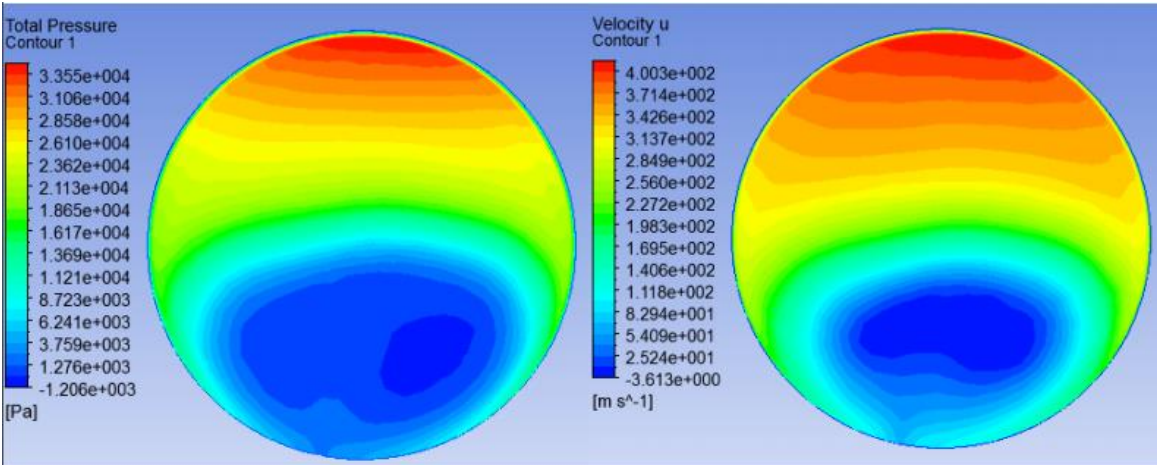
AR=1.25



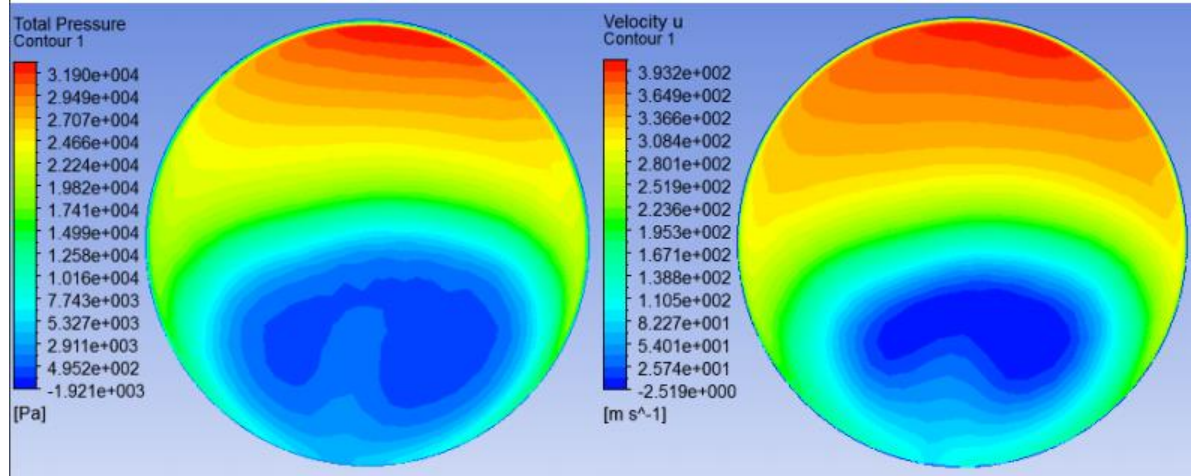
AR=1.5



AR=1.75



AR=2



AR=2.5

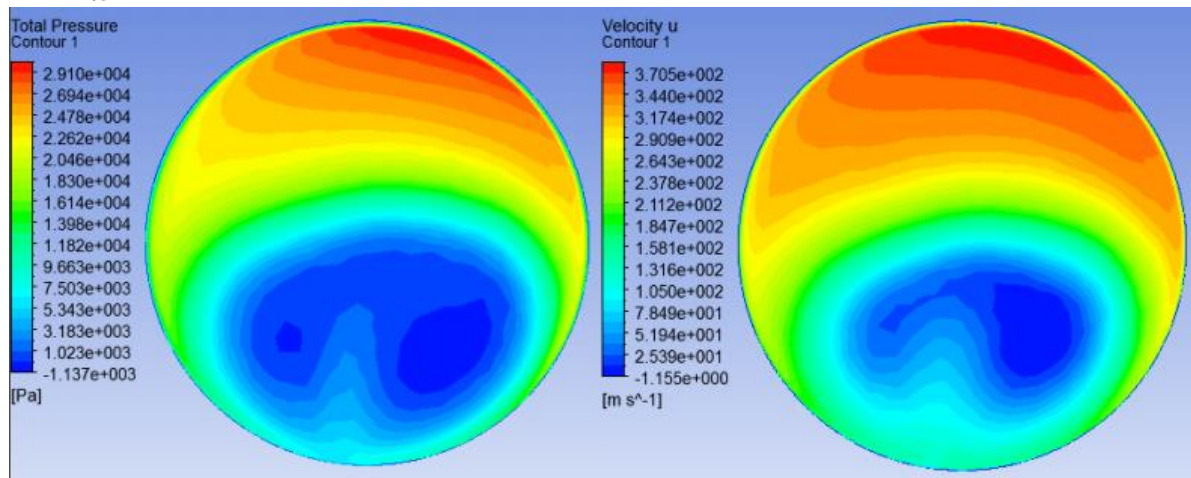


Figure 60(a): Total pressure and x-velocity contours at AIP for different inlet aspect ratios

Figure 60(b) displays the variation of mass averaged Mach number at the AIP for different aspect ratios.

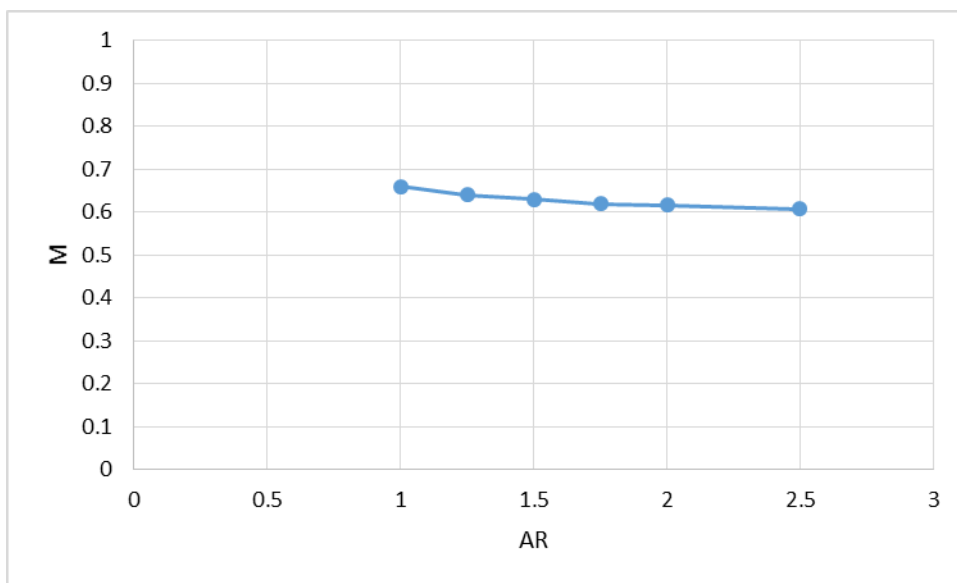


Figure 60(b): Variation of Mach number at AIP for different aspect ratios

6.2.2 Total Pressure Recovery at AIP

Pressure recovery is an important criteria in judging inlet performance. Pressure loss in the duct can be due to a number of reasons namely higher surface area of the duct that causes higher wall friction for the flow, formation of secondary flows in the duct due to flow separation, high vorticity in the boundary layer, increased turbulence, etc. Pressure recovery is defined in equation (1.8) in Section 1.2.3. Pressure recovery factors for general aviation is expected to be between 90% and 98% [23]. This is mainly because general aviation aircraft mostly fly at transonic Mach numbers, which can cause high pressure loss in the duct.

Figure 61 shows the variation of total pressure recovery with increasing BLI. The difference in the values of pressure recovery for different aspect ratios is not significant. However, it is noticeable that the pressure recovery increases up to an aspect ratio of 1.75 and then starts to decrease for very high aspect ratios. This trend can be explained based on the discussion in the previous section regarding the upper spline curvature of the S-Duct. As discussed before, with increasing aspect ratio, the upper spline curvature of the duct reduces, because of which the static pressure region in this part is not low enough to lift up the slow moving boundary layer on the bottom wall. Hence, pressure loss reduces up till AR=1.75.

Interestingly, this phenomenon is not persistent after AR=1.75. This is mainly because for aspect ratios greater than 1.75, the percentage of BLI becomes too high (43%) relative to the ingested free-stream to maintain a low pressure loss. Also, for aspect ratios greater than 1.75, major part of the AIP is covered with vortex pair developed inside the duct, which reduces total pressure at the AIP, even though it reduces distortion (explained in the next section).

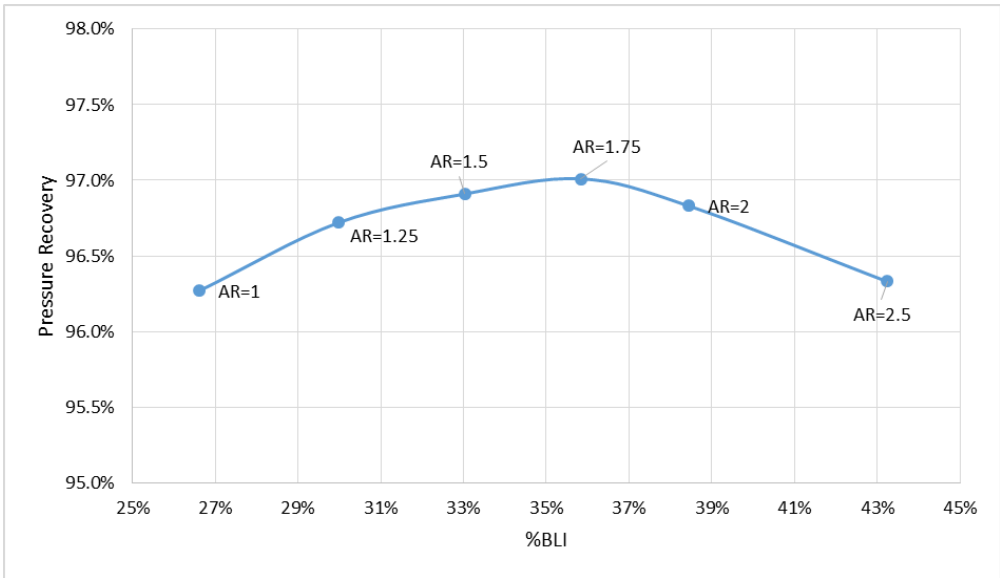


Figure 61: Variation of Pressure Recovery with %BLI

Large amount of low momentum boundary layer is more turbulent than the free-stream and separates quickly inside the S-Duct and causes larger secondary flows affecting pressure recovery at the fan-face.

6.2.3 Distortion at AIP

Aspect ratio will also influence distortion at the AIP. As the aspect ratio increases, BLI increases and hence more non-uniform flow is ingested by the inlet, which means that the distortion should increase with increasing aspect ratio. This is seen in Figure 62, where the distortion coefficient, DC(60), increases with increasing aspect ratio till AR=1.75. After this, the DC(60) value starts to decrease. This is mainly attributed to the fact that at very high aspect ratios, very large part of the engine fan-face is covered with the vortex pair. Therefore, the pressure loss is now spread over a major part of the AIP and not just at the bottom of the duct.

For AR=2 and AR=2.5, the pressure loss between the top and bottom part of the S-Duct is very small because of which, the distortion value reduces but the pressure recovery reduces as well since large part of the AIP is covered with the vortex pair, which reduces total pressure at the AIP and hence pressure recovery.

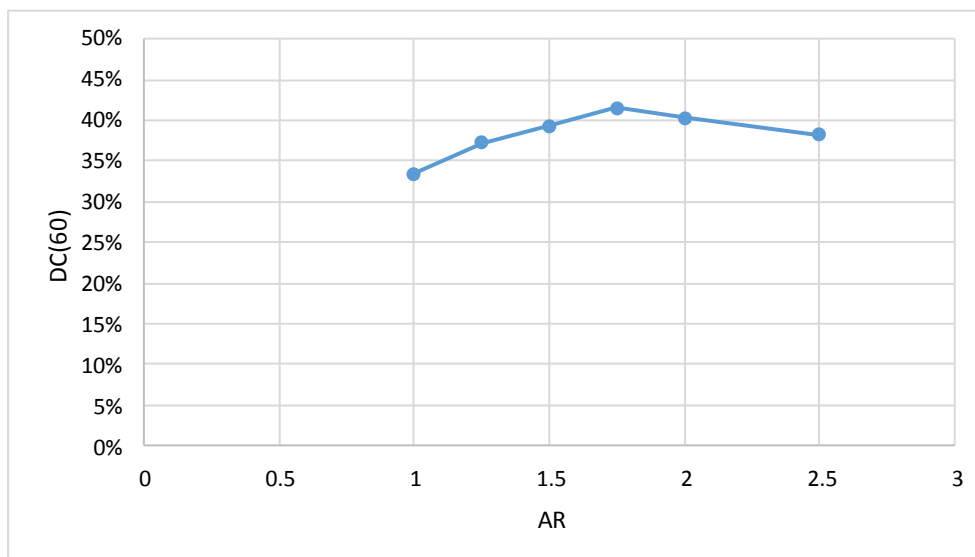


Figure 62: Variation of DC(60) with aspect ratio

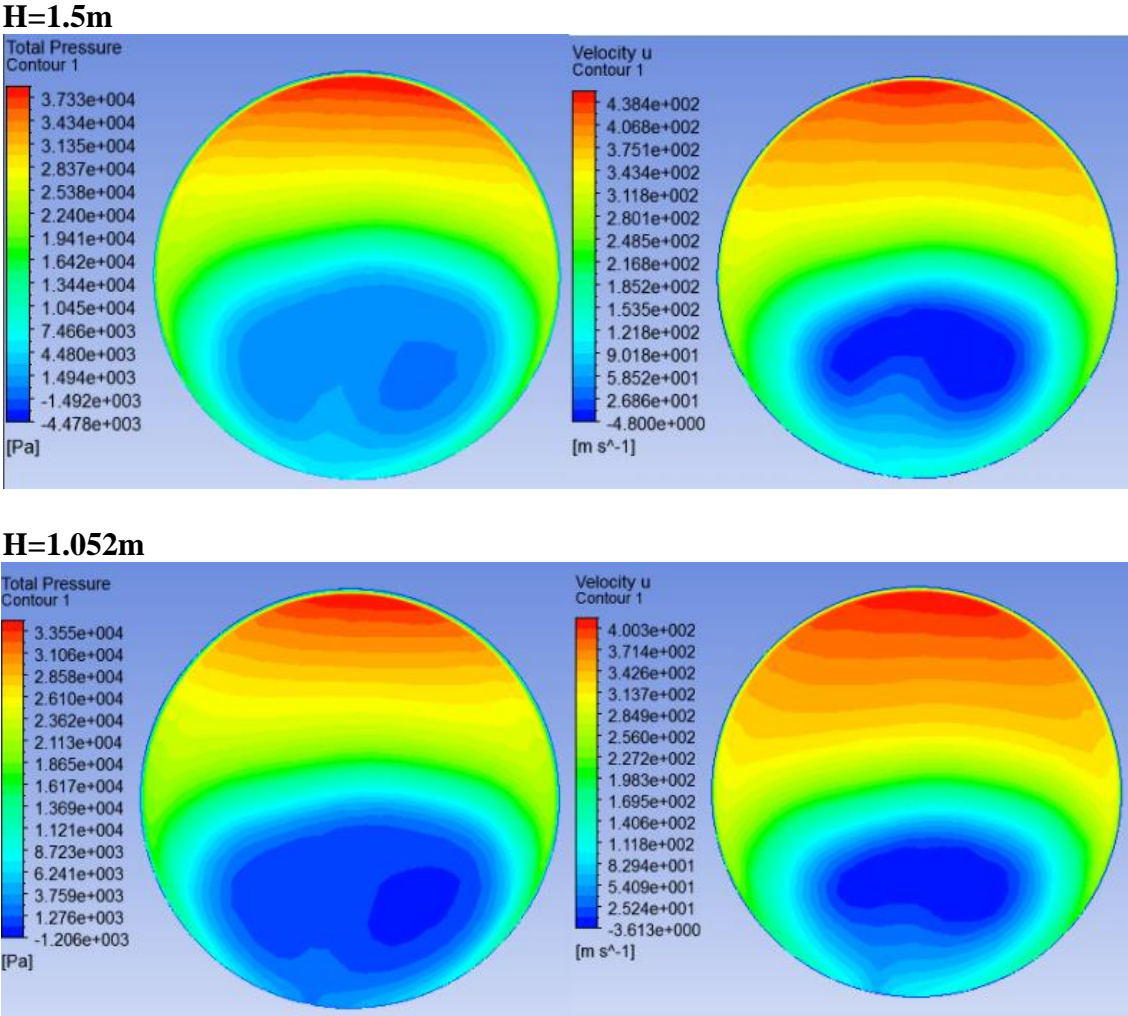
Although the distortion value is high, design changes in the later sections will significantly improve the results. The pressure recovery for AR=1.75 was the highest at 97.01% with a poor DC(60) value of 41%. The distortion levels of other aspect ratios are not very significantly lower. Hence, the gain in pressure recovery is prioritized over high distortion value.

In addition to this, Fig 60 (b) shows that the mass averaged Mach number obtained at the AIP for AR=1.75 is nearly 0.6, which is more acceptable than lower aspect ratios that reach up to a Mach number of 0.66. Therefore, AR=1.75 is chosen for further testing of the inlets for variation in height and length.

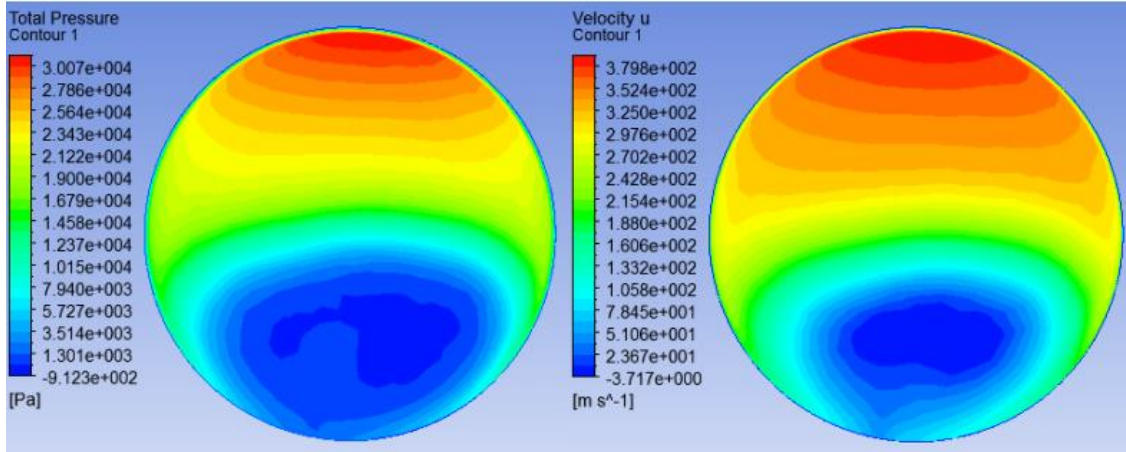
6.3 Influence of Duct Height

As described in Section 5.3.1, the duct height is parameterized from center of the inlet face to center of the fan-face or AIP. This means that as the duct height increases, the formation of secondary flows will be magnified. This can be attributed to the adverse pressure gradient at the bottom wall of the duct causing flow separation and also due to the flow acceleration on the upper wall of the duct due to higher curvature of the spline caused by increased height, which in turn causes vortex pair formation due to low static pressure region at the upper wall. For constant inlet aspect ratio and length, an increase in the value of height will most certainly reduce pressure recovery and increase distortion at the AIP. Fig 63 shows the total pressure and x-velocity contours at AIP for variation in height.

The contour plots make it evident that for highest value of height (1.5m), the region of recirculation is the largest and as the height is decreased, the blue region becomes smaller. This is mainly because with decreasing height, the adverse pressure gradient of the bottom wall of the S-Duct reduces and separation becomes more gradual than sudden. Hence separation is delayed and pressure recovery increases, which is seen in Fig 64.



H=0.7m



H=0.3m

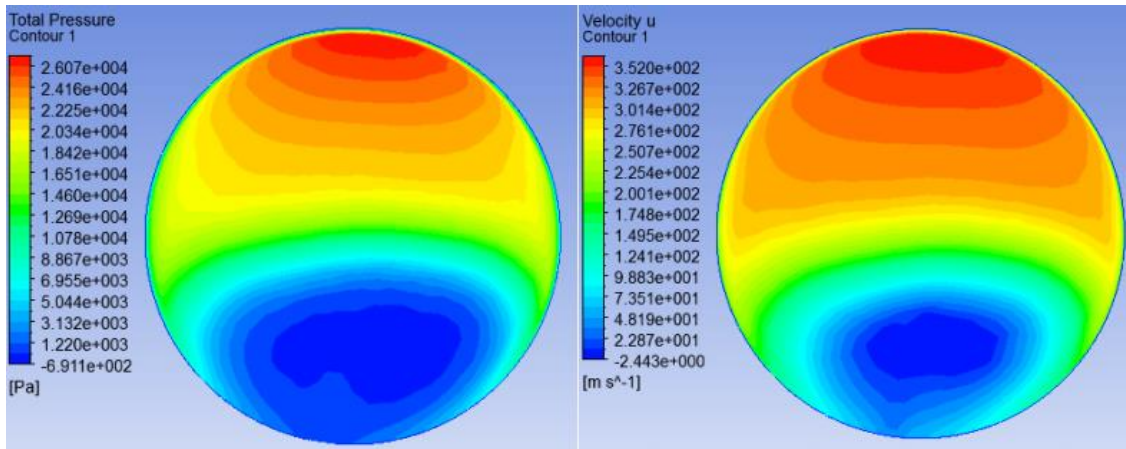


Figure 63: Total pressure and x-velocity contours at AIP for variation on duct height

Fig 64 shows the variation of pressure recovery with increasing height. The trend predicted above is seen in Fig 64. The pressure recovery value reduces from 97.7% to 96.4%.

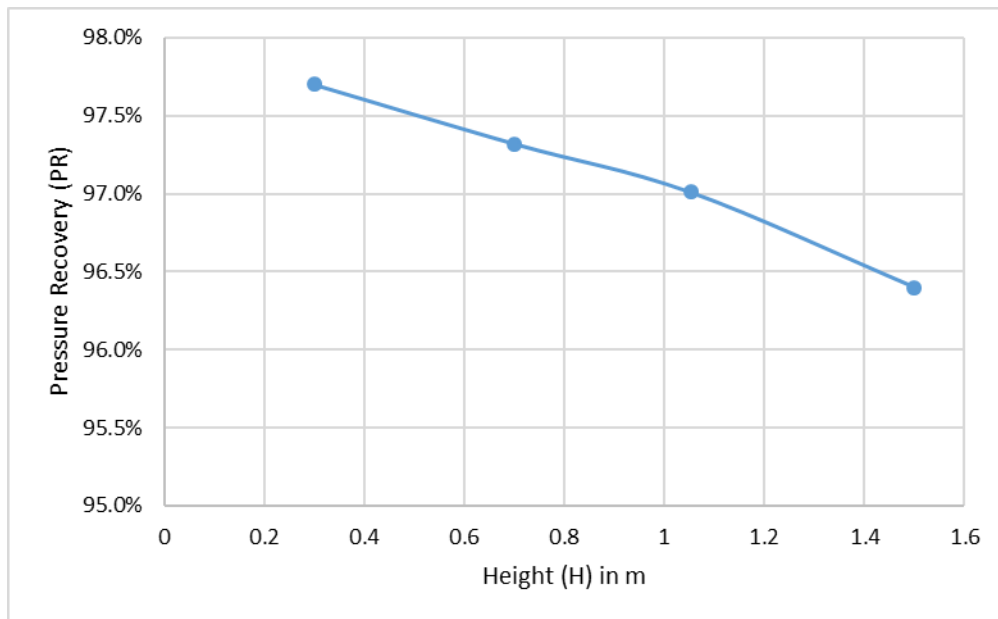


Figure 64: Variation of pressure recovery with duct height

The effect of variation in duct height also influence distortion at the AIP. With increasing height, the boundary layer separation moves further upstream towards the throat and large secondary flow formation takes place, which causes a major portion of the AIP to experience low total pressure. The difference in the total pressures of the top and bottom half of the AIP is significant and hence the distortion values linearly increase with increasing height. Fig 65 shows that there is approximately a 15% increase in the value of DC(60) as the height increases from 0.3m to 1.5m. Naturally, the lowest height value is preferred for further testing. Hence, H=0.3m is chosen as the preferred height value for further testing with variation in duct length.

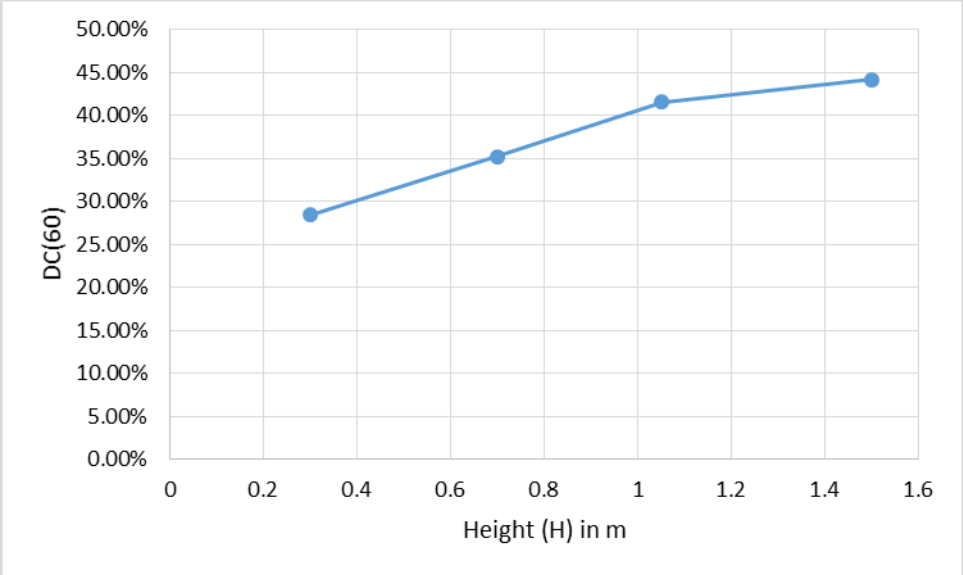


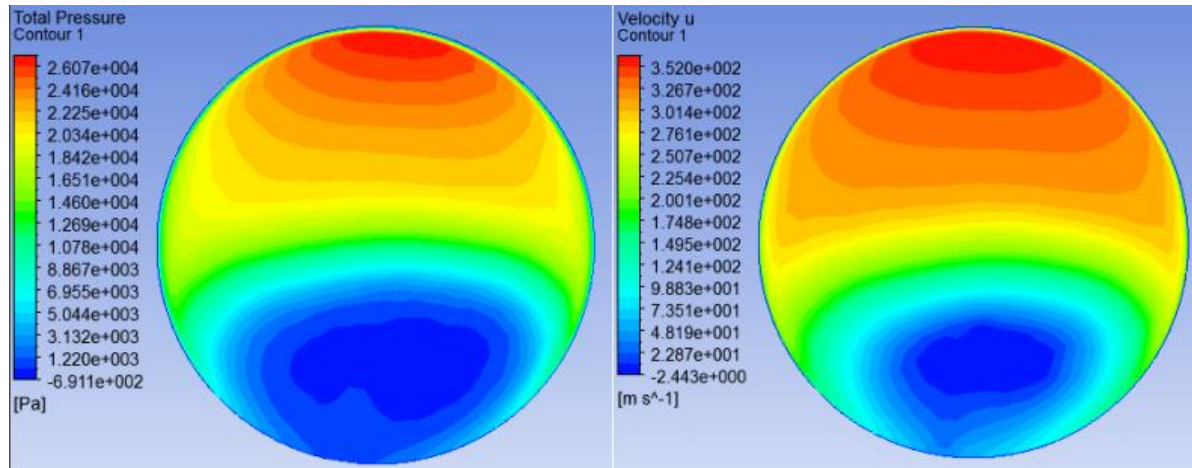
Figure 65: Variation of DC(60) with duct height

6.4 Influence of Duct Length

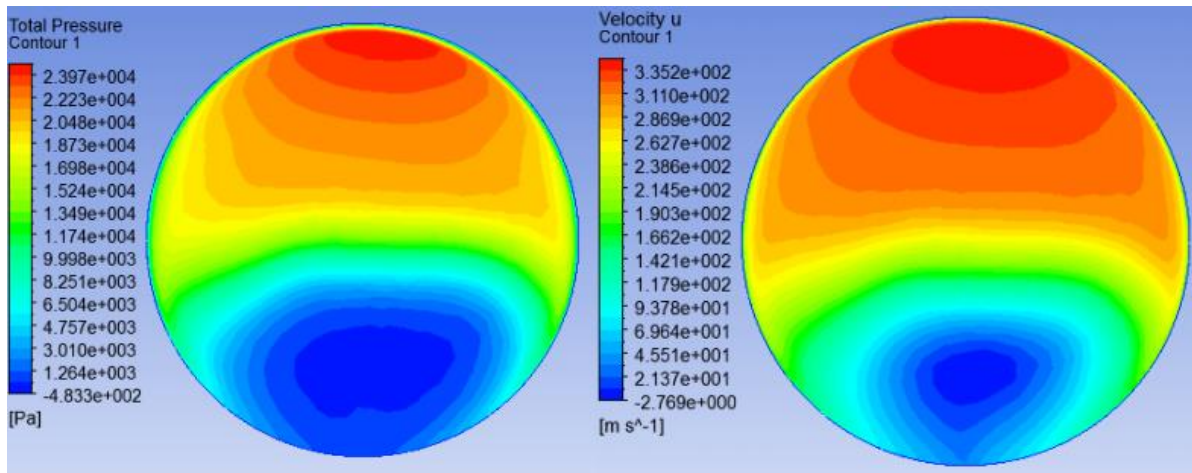
Length of the duct plays a crucial role in the overall performance of the inlet. 4 different duct lengths were tested ranging from 4.85m to 7.27m. It becomes clear that the non-uniformity in flow will be larger for lower duct length. This is because in this case, the flow traverses a larger distance over the fuselage before entering the inlet and hence suffers more losses as compared to when it enters a longer length duct. However, for a long duct length, the pressure losses will be more than for a shorter duct length due to higher wetted surface area of the duct for the former case. Fig 66 shows the total pressure and x-velocity contours at the AIP for variation in duct length.

It is quite clear from Fig 66 that the total pressure on outlet decreases as the duct length increases. As discussed before, this is mainly due to pressure losses because of higher wetted surface area for longer lengths. This in turn means that the pressure recovery will get reduced as the length of duct is increased. Fig 67 shows how the wetted area of the duct increases with increasing duct length.

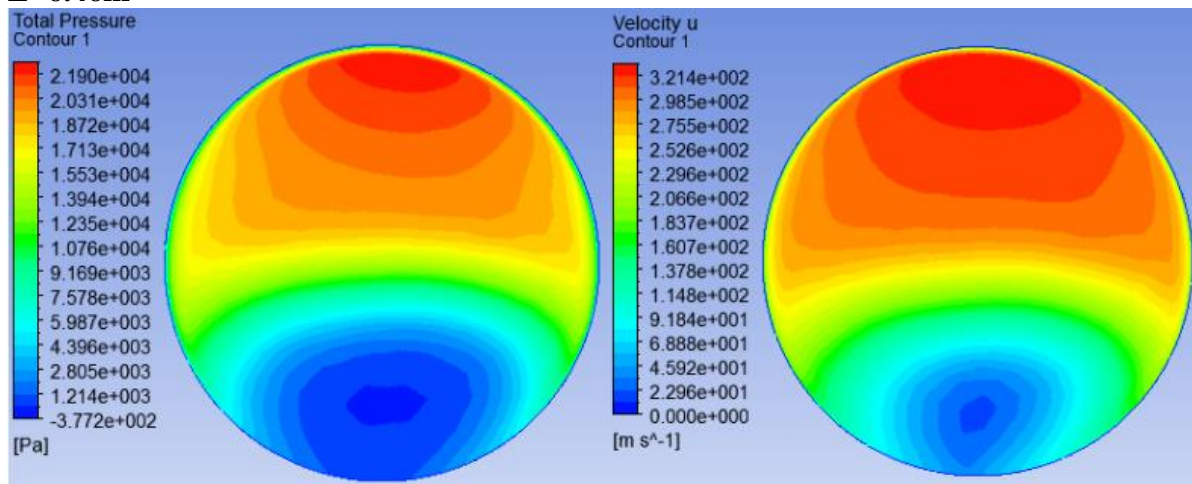
L=4.85m



L=5.65m



L=6.46m



L=7.27m

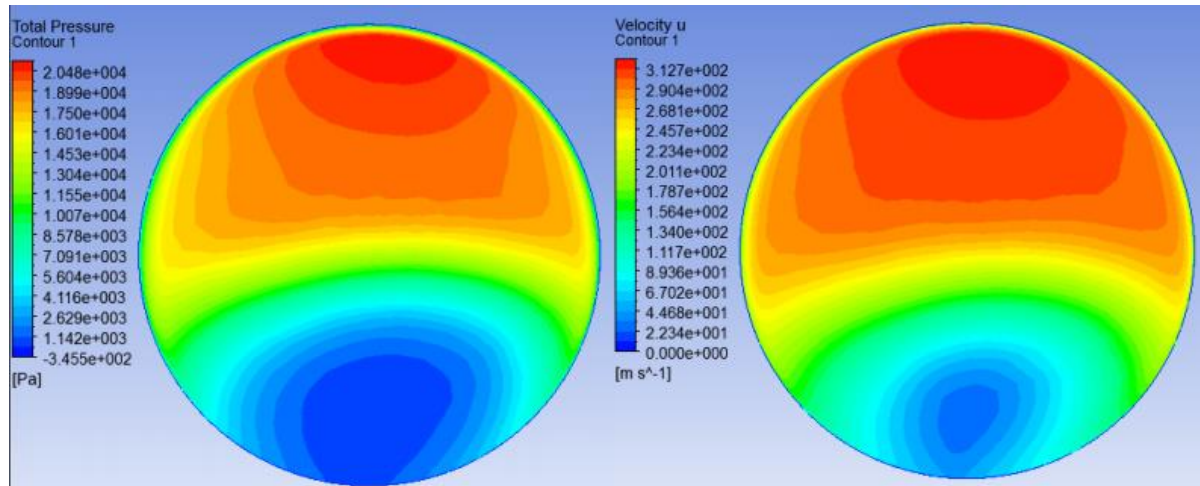


Figure 66: Total pressure and x-velocity contours at AIP for variation in duct length

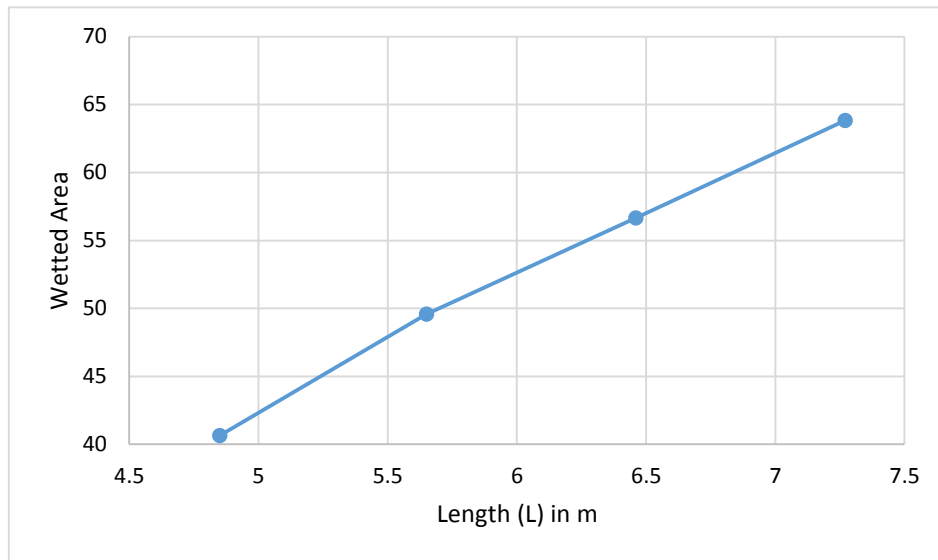


Figure 67: Variation of duct wetted area with duct length

The variation of pressure recovery with increasing duct length is shown in Fig 68. As described before, the decreasing pressure recovery is attributed to increased wall friction due to higher wetted surface area of the longer ducts. The shortest duct with $L=4.85\text{m}$ performs best with a pressure recovery value of 97.7%, which means that the pressure loss in this duct is only 2.3%.

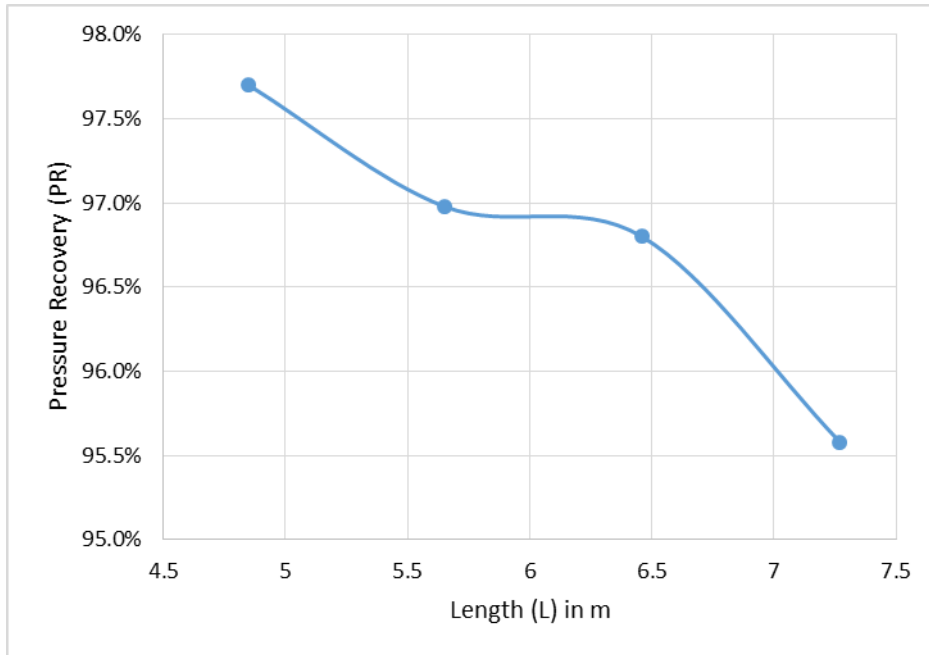


Figure 68: Variation of pressure recovery with duct length

Fig 69 shows the mid-plane views of the different length cases to show the separation areas and the values of the negative velocities.

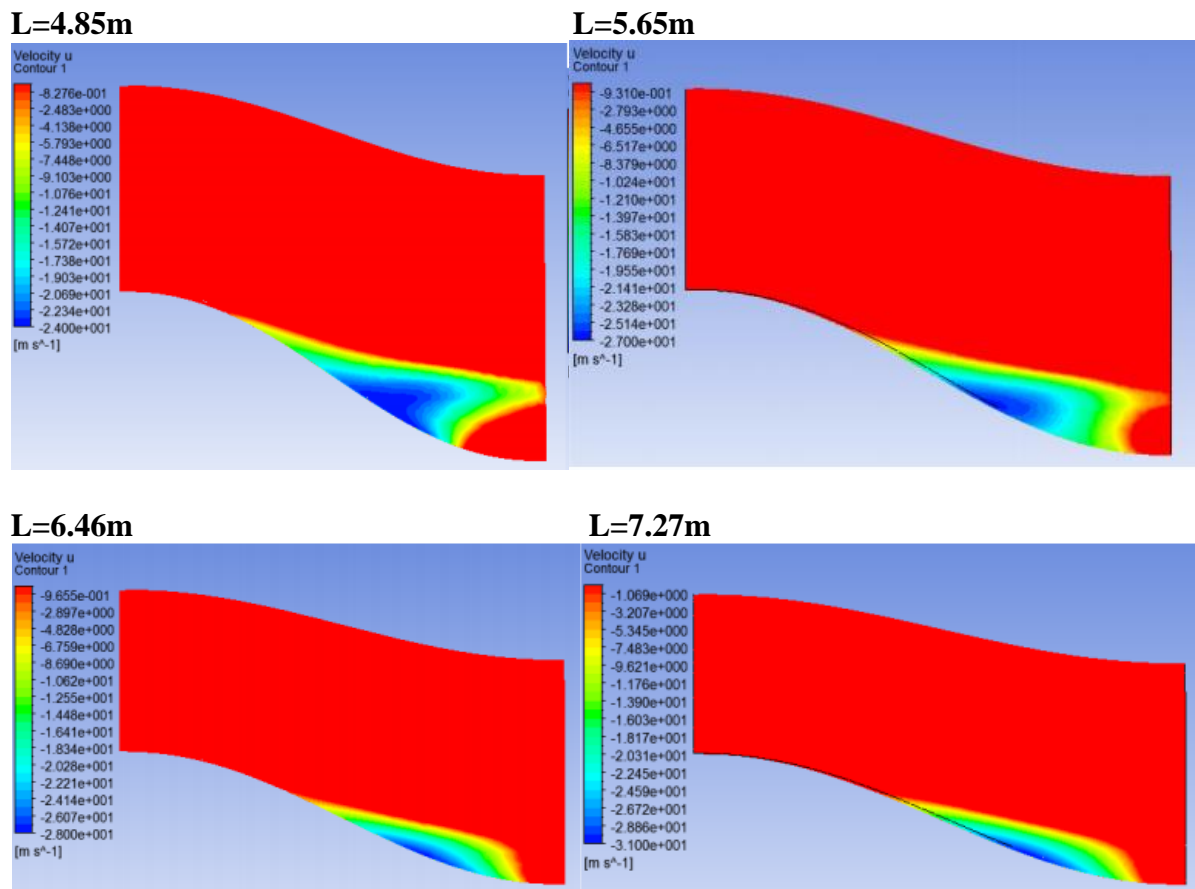


Figure 69: Mid plane views for increasing duct lengths

Fig 69 shows that the separation inside the S-Duct becomes more gradual and decreases quite significantly for the largest length duct. However, the value of negative velocity is also quite high for this case due to high in the boundary layer caused by wall friction. So, even though a smaller area of the fan is affected by the recirculation region for the larger length case, the value of x-velocity and total pressure significantly less and causes high pressure difference between the upper and lower part of the AIP.

The increase in length causes higher pressure losses in the boundary layer as compared to the freestream. This causes a large difference in pressure loss in the upper half of the AIP (affected by free-stream without major losses) and the bottom half where the low momentum boundary layer imparts low pressure. This difference in pressures gives rise to a large distortion value for the longer ducts.

From Fig 70(a), it is evident that the shortest duct gives the best performance with a DC(60) value of 28%. This will be further reduced in later sections after design improvements.

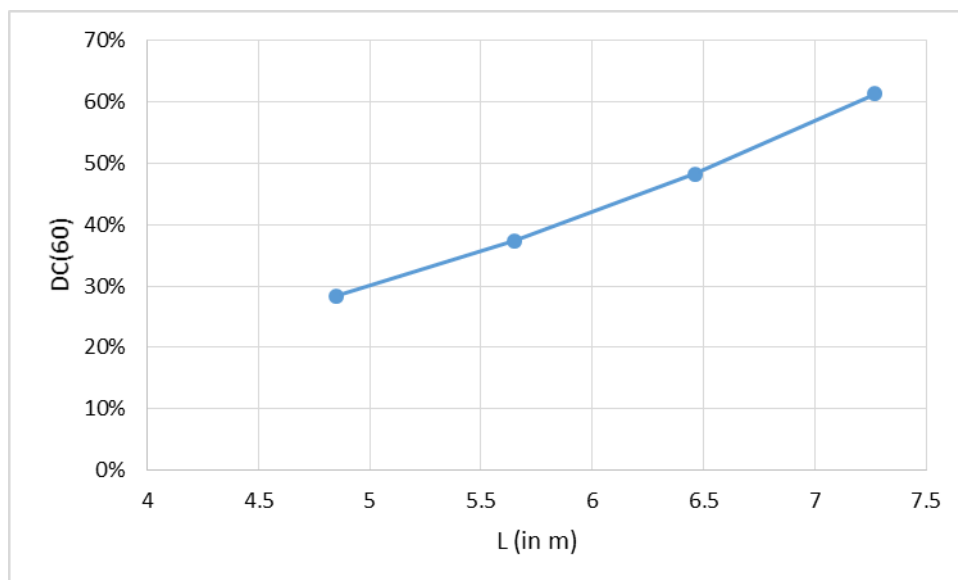


Figure 70(a): Variation of DC(60) with duct length

From the conclusions on length, height and inlet aspect ratio results, so far the inlet with best performance (PR = 97.7% and DC(60) = 28.45%) has the following dimensions:

1. H = 0.3m
2. L = 4.85m
3. AR = 1.75

Figures 70(b) and 70(c) show the flow development and streamlines inside the s-duct obtained from testing, respectively.

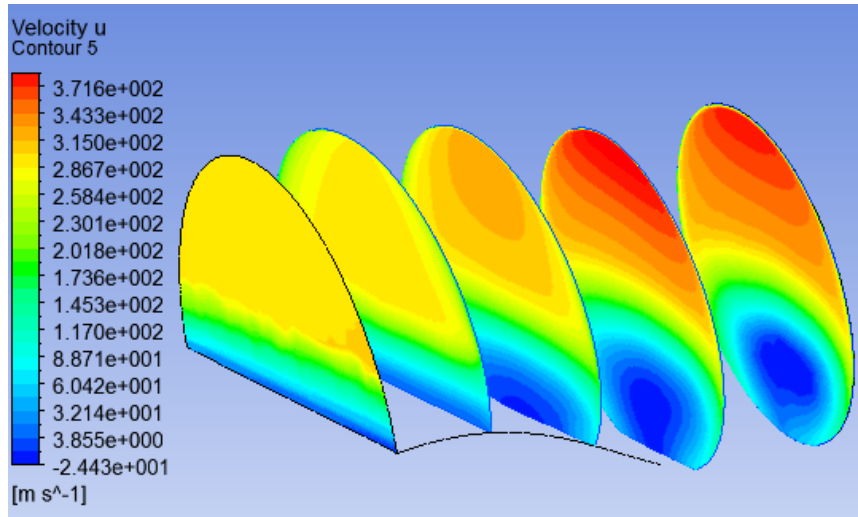


Figure 70(b): Flow development inside the S-duct obtained from testing of geometrical parameters

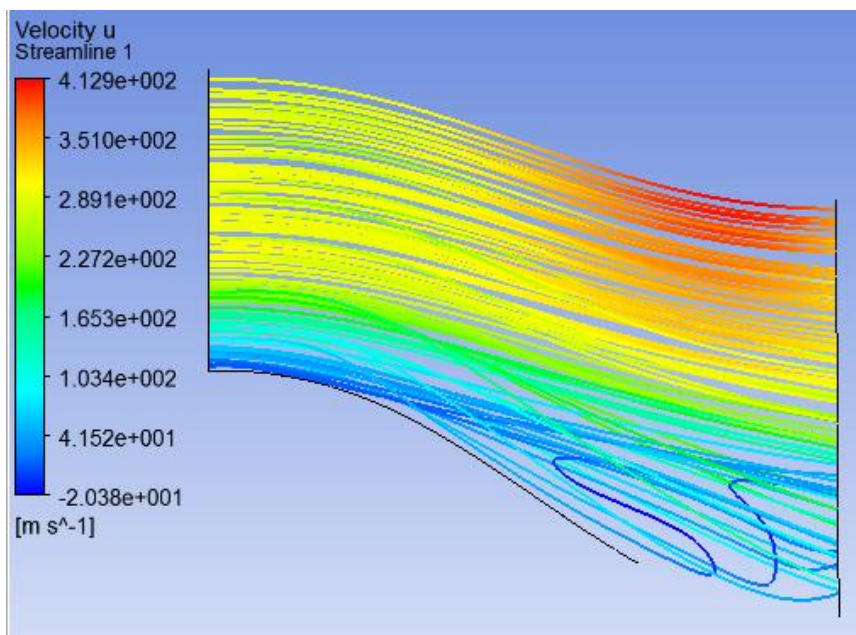
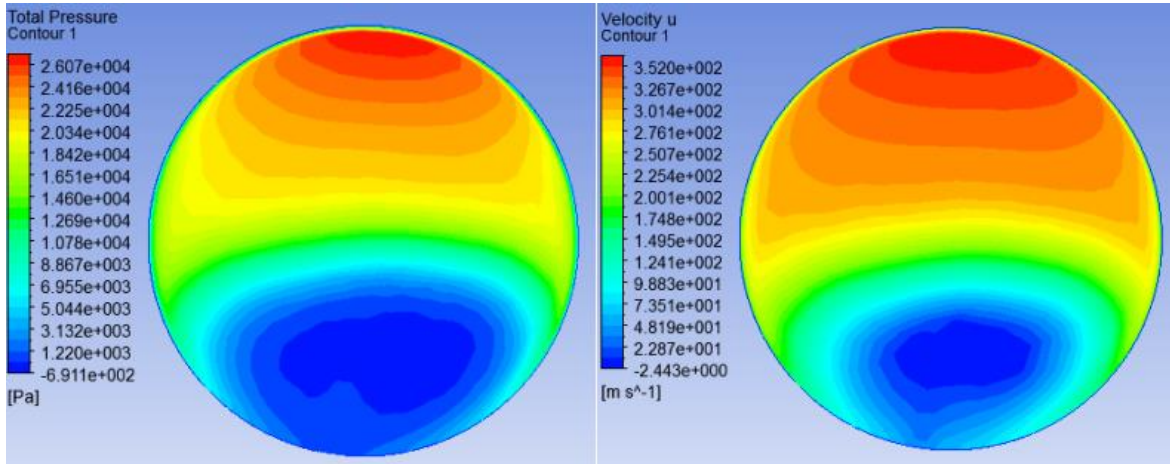


Figure 70(c): Streamlines inside the S-duct obtained from testing of geometrical parameters

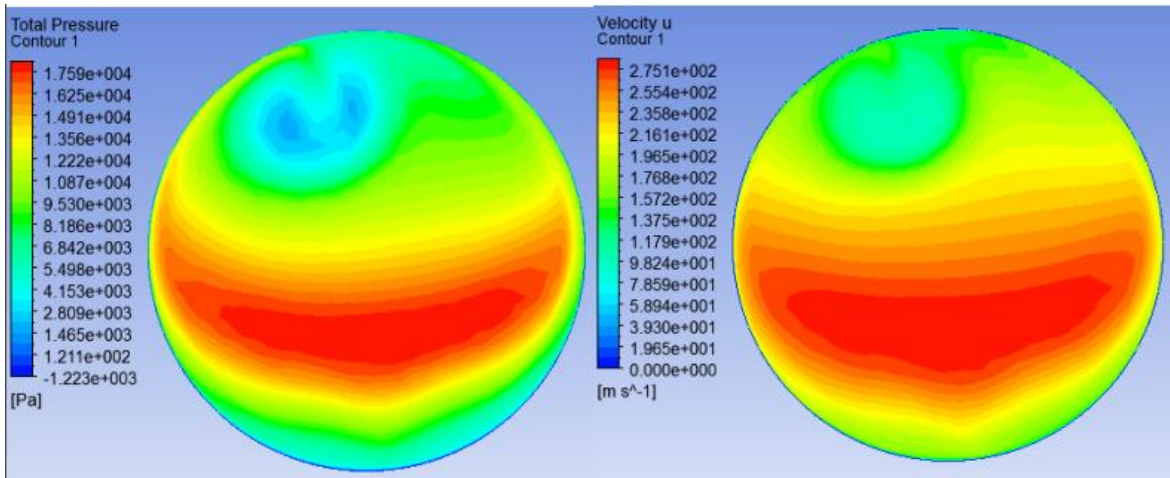
6.5 Influence of Other Configurations

So far, a high value of pressure recovery has been achieved. However, the distortion levels can be further reduced if the recirculation region in the duct is eradicated. Therefore, further design improvements are required. Fig 46 in Section 5.7.3 shows the configurations that were tested to check if there is an improvement in the results. The description of these new configurations is also given in the same section. The main requirement is to improve distortion levels and minimize secondary flow formation. Keeping this in mind, Fig 71 shows the total pressure and x-velocity contours at the AIP for different configurations. Figures 72 and 73 shows the pressure recovery and distortion values for the same.

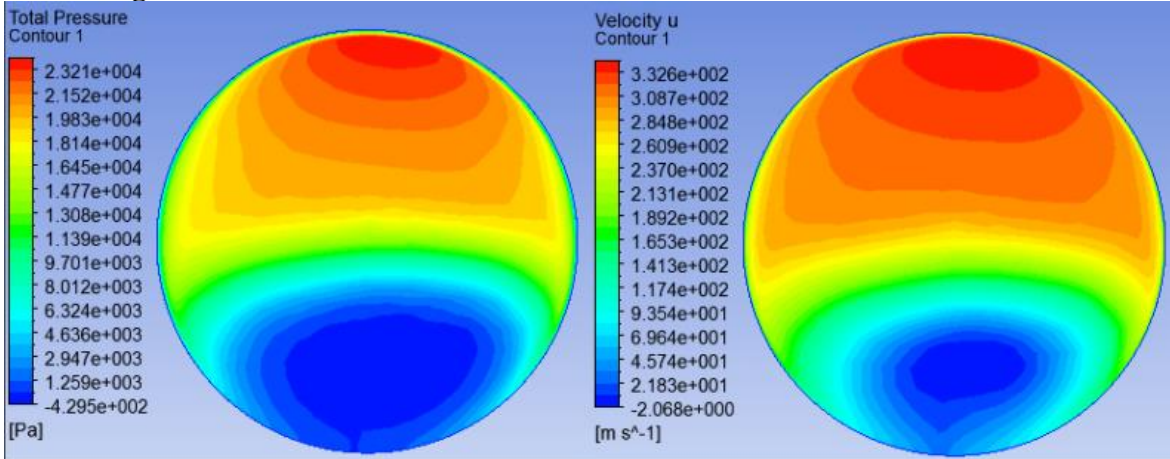
Standard S-Duct



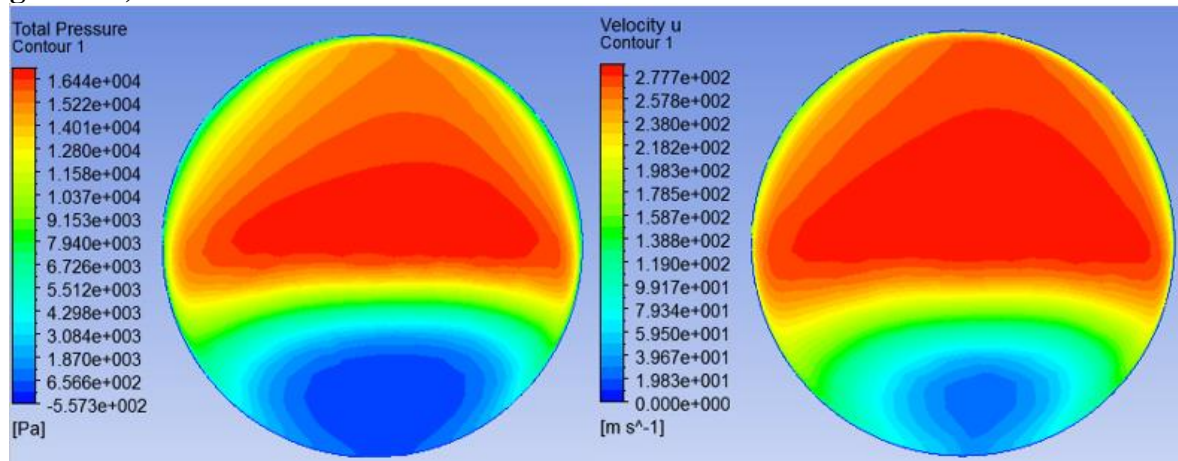
Reverse S-Duct



Zero Height S-Duct



Duct with pressure gradient for both freestream and boundary layer (double gradient)



Duct with zero pressure gradient for boundary layer (zero gradient)

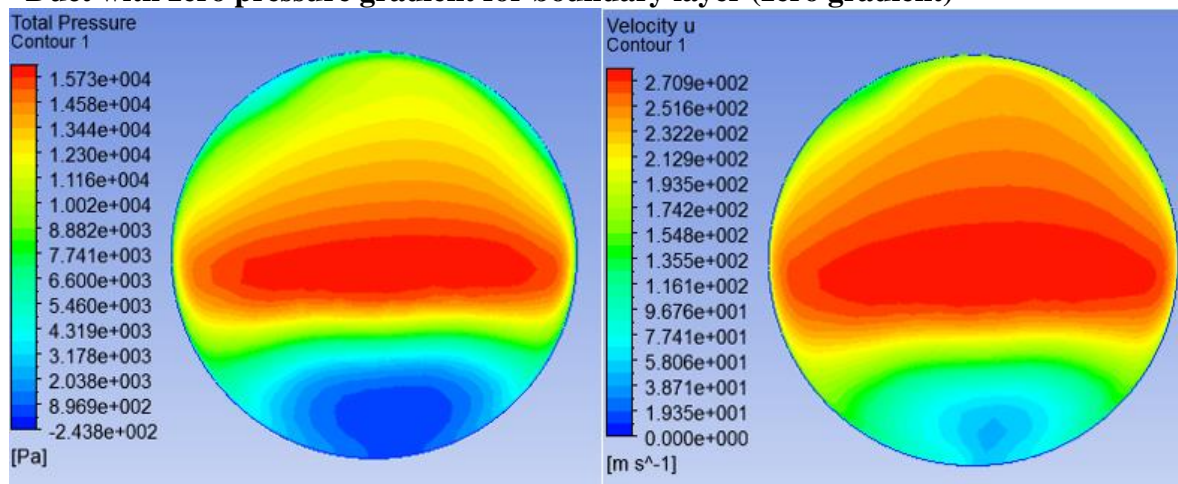


Figure 71: Total pressure and x-velocity contours at AIP for different configurations

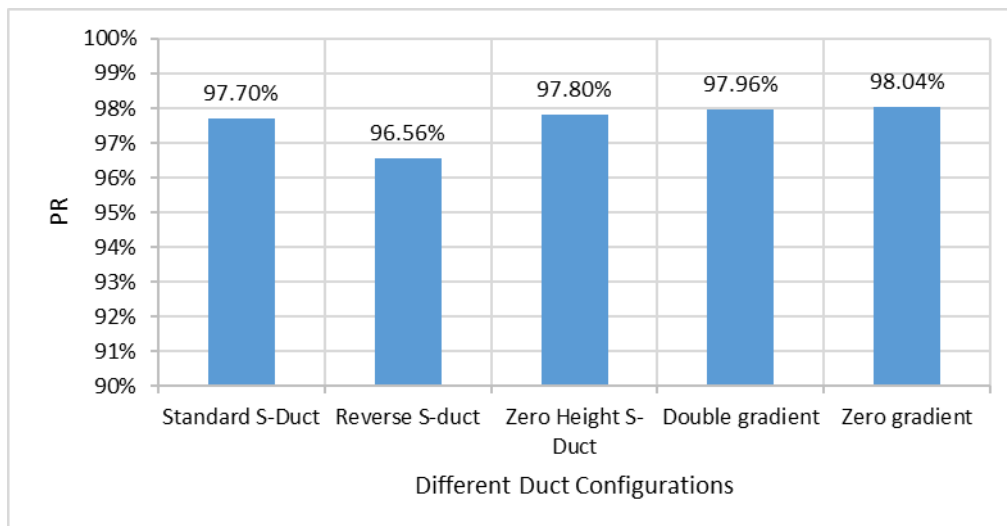


Figure 72: Pressure recovery for different inlet configurations

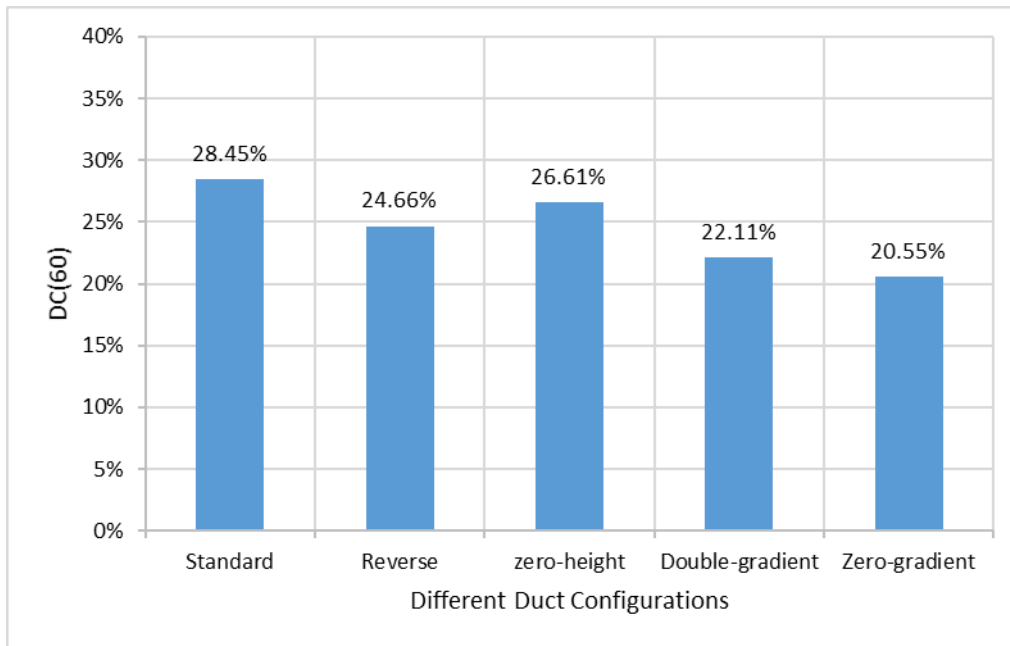


Figure 73: DC(60) for different inlet configurations

In Figure 71, the first case (standard S-Duct) is the most case that is most optimum based on the previous results of length, height and aspect ratio testing. After this, reverse s-duct case was tested in order to see if pressure recovery and distortion levels improve, when ingested boundary layer in accelerated instead of the freestream. It is interesting to note that this method reduces the distortion levels by as much as 4% as shown in Fig73. However, since the freestream air entering inside the upper part of the inlet is at a much higher velocity than the boundary layer, it separates quickly even for a low adverse pressure gradient on the upper wall of the reverse s-duct. This causes some pressure loss on the upper half of the AIP as is seen in the second case in Figure 71. As seen in Figure 72, there is almost a 1% pressure loss in the reverse s-duct case as compared to the standard s-duct.

The mid-plane views for all configurations is shown in Figure 74 to visualise the areas of separation.

The next case is the one with zero center-to-center height of the s-duct. This is bound to improve results as a reduction in height reduces secondary flow formation. As a result of this, although the pressure recovery improved only very slightly, but the value of DC(60) reduced by 2%. The next case was with the adverse pressure gradient for both boundary layer and freestream, which means that the fan-face is almost symmetrically in front of the inlet. This case was tested in order to reduce the boundary layer separation on the lower wall without increasing freestream separation on the upper wall of the s-duct. This can be seen for a better understanding in Figure 74. Promising results were obtained as shown in Figures 72 and 73. Pressure recovery of 97.96% and DC(60) value of 22.11% was achieved.

Finally, the last case was the one with zero pressure gradient for the ingested boundary layer. In, this case the bottom wall is completely flat, which means that the deceleration in the boundary layer flow is only due to wetted surface area and not because of pressure gradient. This also completely eradicates secondary flows or any areas of separation inside the S-Duct. The zero-gradient case provides the best results with a pressure recovery value

of 98.04% and a DC(60) value of 20.55%. Further reduction in the DC(60) values can be achieved by the use of flow control techniques using vortex generators or gas jets to re-energize the boundary layer flow. The current thesis project does not focus on flow control techniques.

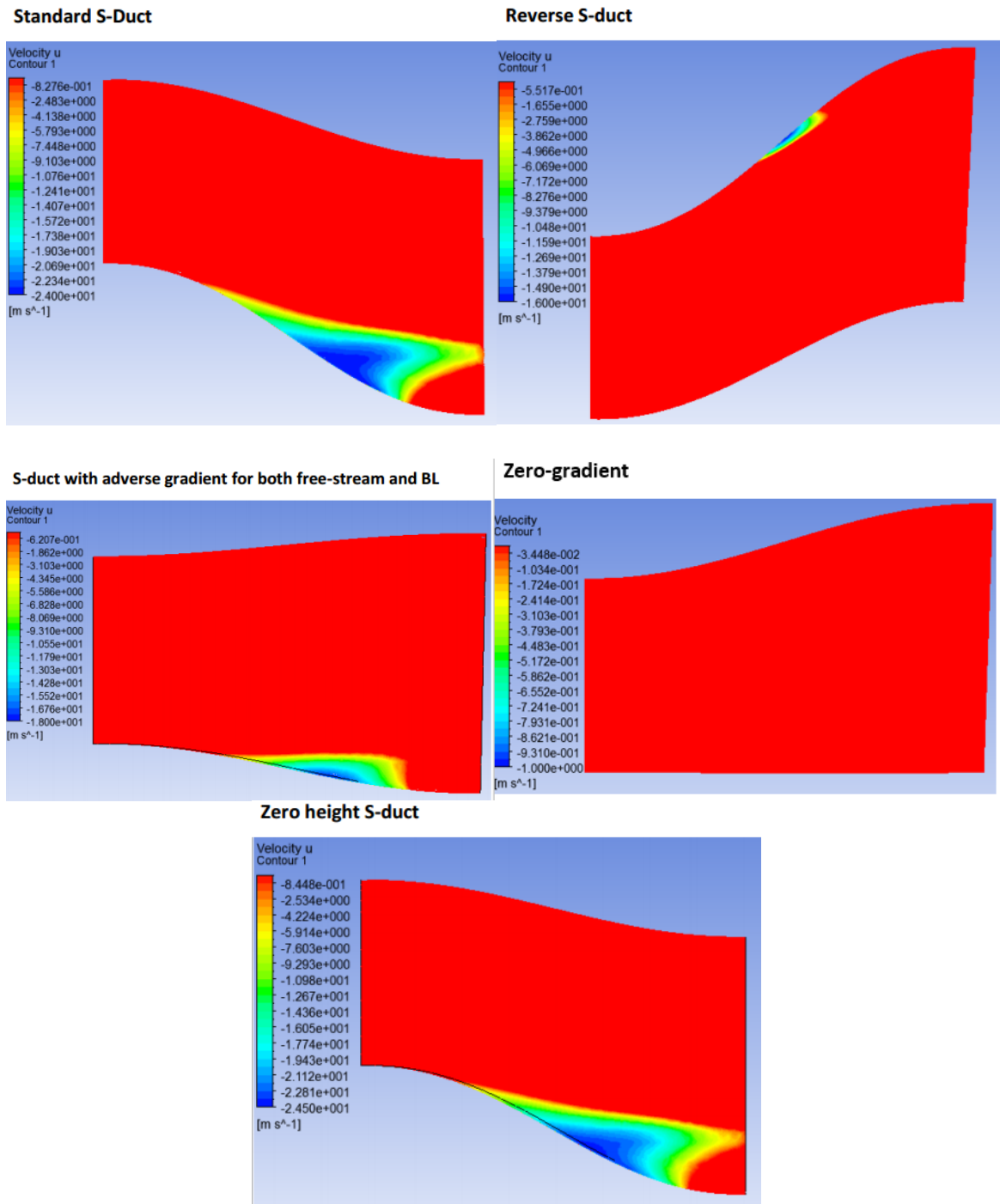


Figure 74: Mid-plane views for different configurations to show separation regions

Figure 74 clearly shows the benefit of a flat bottom wall for an inlet configuration as there are no separation regions inside the inlet with zero pressure gradient for the bottom wall. Furthermore, the adverse pressure gradient for the freestream slows down the velocities on the upper half of the AIP and hence creates a more uniform pressure distribution at the AIP, thereby reducing pressure distortion.

For a final comparison, Figure 75 shows the mass averaged Mach numbers at the AIP for all the inlet configurations shown in Figure 74. Based on Mach number at the AIP, double-gradient duct provides the best performance since the desired Mach number at the AIP is nearly 0.5. However, since the pressure recovery and DC(60) values are both better for the zero-gradient case, and the Mach number at the AIP ($M=0.538$) is only slightly higher than the lowest value (0.516) it is chosen as the duct with the most optimum performance,

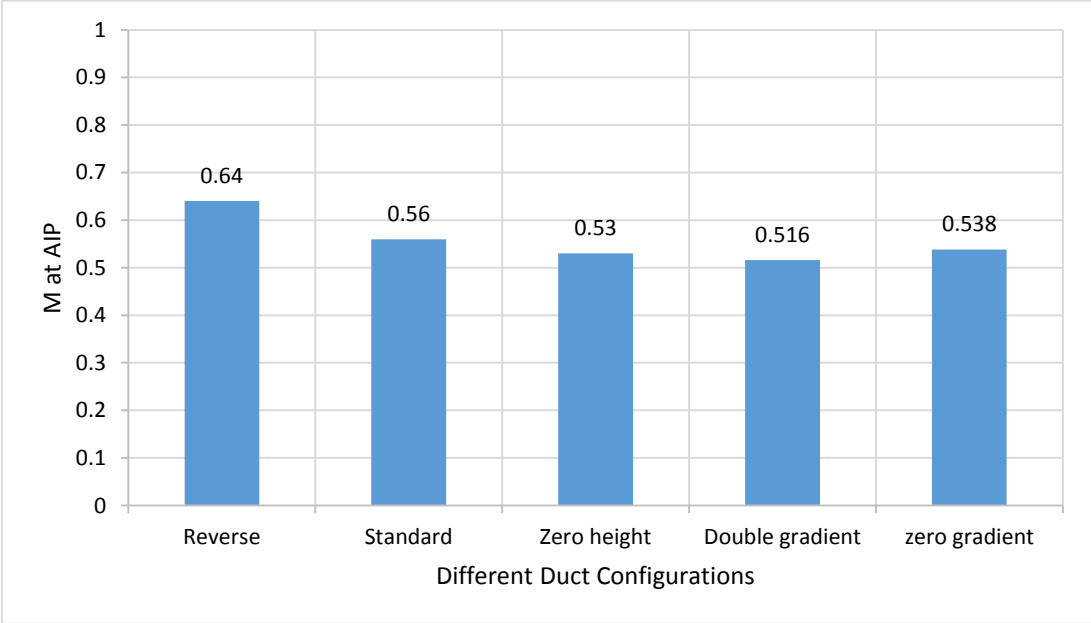


Figure 75: Mach number at the AIP for different configurations

6.6 Results for Nacelle Lip

As described in Section 5.3.1, the design of the internal nacelle lip depends on contraction ratio and semi major-to-minor axis ratio of the lip ellipse. Based on existing literature results [45] [48], 3 different contraction ratios were tested using a semi major-to-minor lip ellipse ratio of 2, widely used for transonic Mach numbers. These tests were carried out initially for the double-gradient case because at the time, the case with zero-gradient (flat bottom wall) had not been investigated yet. The change in contraction ratio has its main effect on pressure recovery value. Table 4 shows the pressure recovery values for the 3 different contraction ratios.

Table 4: Pressure Recovery Results for Different Contraction Ratios for double gradient case

Contraction Ratio (CR)	Lip ellipse axis ratio (m/n)	Pressure Recovery (PR)
1.01	2	97%
1.04	2	98.3%
1.07	2	95%

Based on the results shown in Table 4, contraction ratio 1.04 was chosen for further testing with the zero-gradient duct case, which in Section 6.5 showed most promising results. The length of the zero-gradient case was 4.85m. The testing for the contraction ratio 1.04 on this duct was done for both L=4.85m and L=4.03m. The lower length case was investigated in order to reduce wetted surface area. Figure 76 shows the results for these 2 cases.

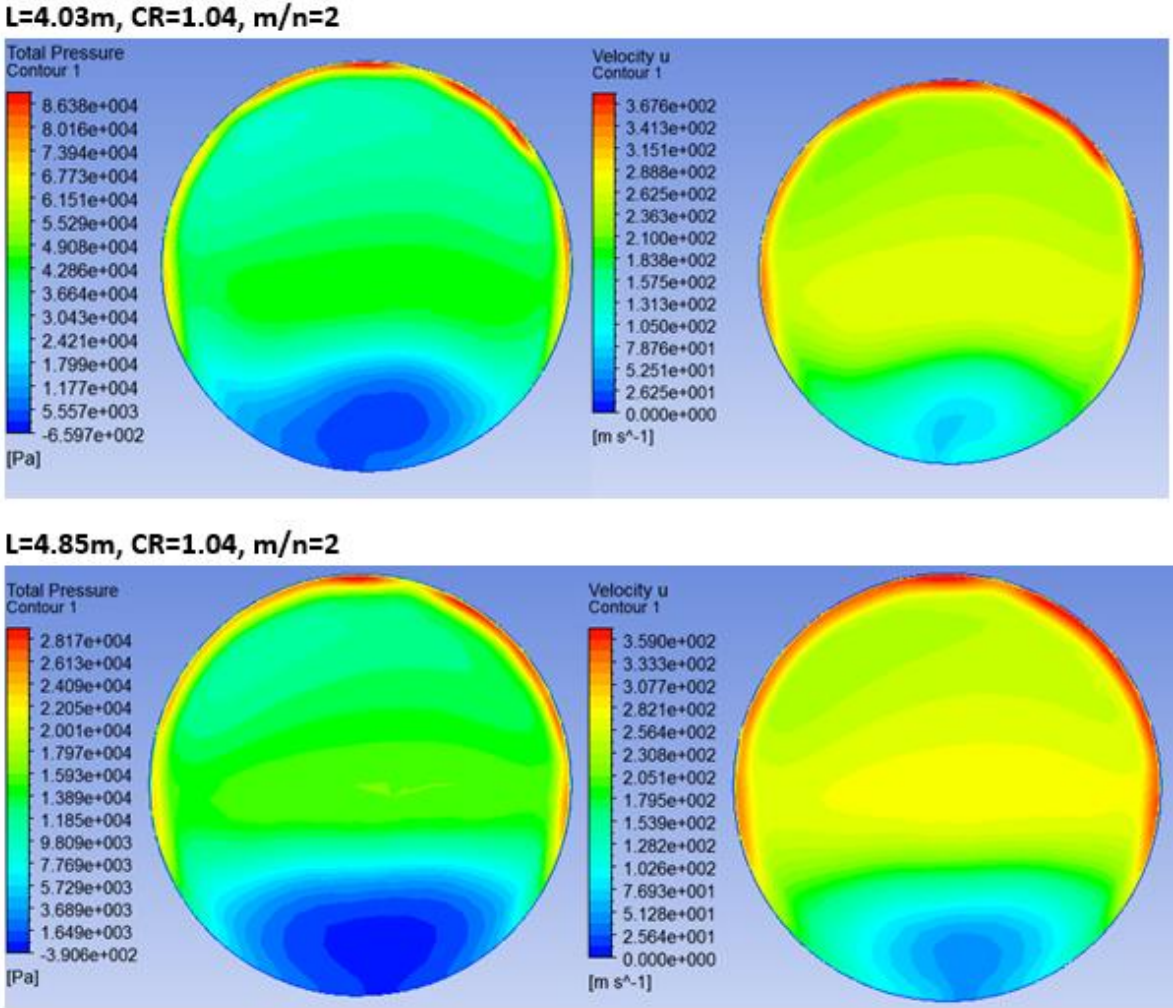


Figure 76: Total pressure and x-velocity contours at AIP for CR=1.04, m/n=2 and L=4.03m and 4.85m

Table 5: Pressure recovery and Mach number results for zero-gradient duct with lip CR=1.04, L=4.03m and 4.85m

L	PR	Mass averaged Mach Number (M) at AIP	Wetted Area
4.03m	99.69%	0.61	34.741 m ²
4.85m	98.04%	0.54	44.067m ²

From Table 5, it can be seen that a lower length has a lower wetted area and hence a higher pressure recovery value as compared to the duct with L=4.85m. However, the mass averaged Mach number at the AIP for the shorter duct is higher as compared to the longer duct. Table 4 shows that the pressure recovery increases slightly for the double-gradient case

(98.3% up from 97.96%). However for the zero-gradient case, which shows more promising results as compared to the double gradient case, the pressure recovery does not really vary. Even then, the zero-gradient case (flat bottom wall for duct) with $L=4.85\text{m}$, $AR=1.75$ and $H=1.615\text{m}$ is preferred because of its overall performance in terms of Mach number obtained at the outlet, distortion levels at the AIP and pressure recovery.

It has been observed from literature study [45] [46] [48] that NACA-1 series airfoils produce good performance for external nacelle design. External cowl design is out of the scope of the current thesis and it focuses only on the internal nacelle and inlet design and analysis. A NACA-1 series airfoil NACA16-021 is chosen to construct the cowl of the final inlet design based on the wide acceptance of NACA-1 series airfoils for providing near constant velocities along the cowl [46]. However, only aerodynamic testing and analysis of a complete BWB with integrated inlet consisting of the external nacelle can provide sufficient understanding of its performance.

6.6.1 Final Inlet Design

Figure 77 shows the final inlet design after testing and analysis of different inlet configurations, geometrical parameters and nacelle lip parameter variations.

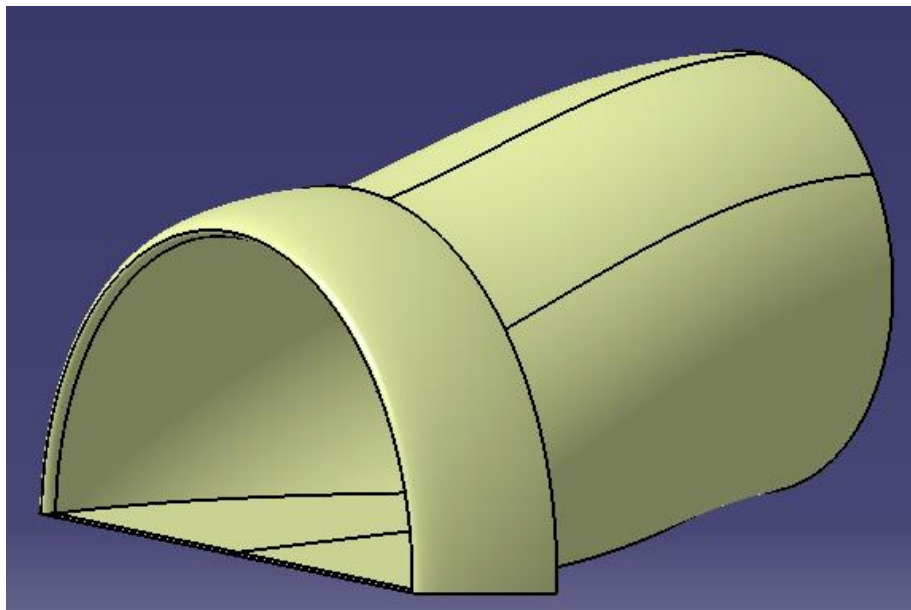


Figure 77: Final inlet design $AR=1.75$, $L=4.85\text{m}$, $H=1.615\text{m}$, $CR=1.04$, $m/n=2$, zero-pressure gradient for boundary layer, $PR=98.04\%$, $DC_{60}=20.55\%$

6.6.2 Final Inlet Design using ParaPy

The geometry obtained as final design (shown in Figure 77) was also created using ParaPy to compare the results. For this, a hybrid grid was generated using 800000 cells and 17 layers of prismatic boundary layer with an unstructured core region. This grid is shown in Figure C.

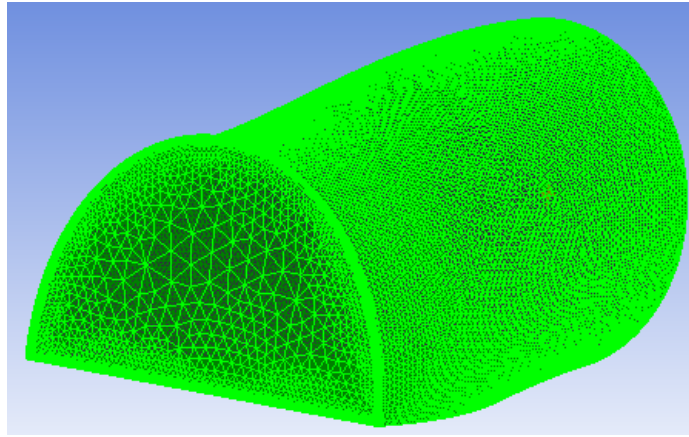


Figure C: Final design grid generated using ParaPy [50]

The ParaPy grid presented a better mesh quality based on aspect ratio of elements, prism thickness distribution, orthogonality and minimum angle (See Appendix G for Mesh Quality Comparison). The inlet face meshes for the grids generated using ICEM and ParaPy are shown in the following figures for comparison.

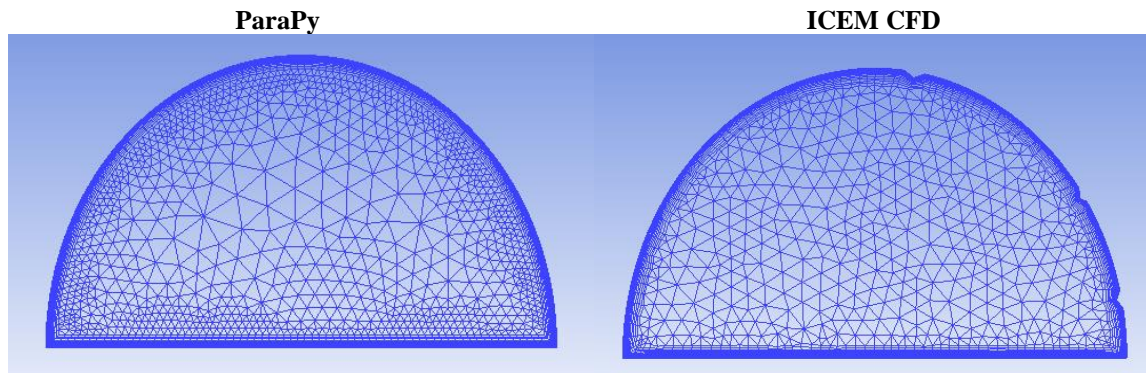


Figure D: Comparison of inlet face mesh; ParaPy and ICEM CFD

The irregularities (crevasses on the circumference) are evident in the ICEM grid as shown in Figure D. Boundary conditions were applied to the ParaPy grid and the solution presented the results shown in the following figures.

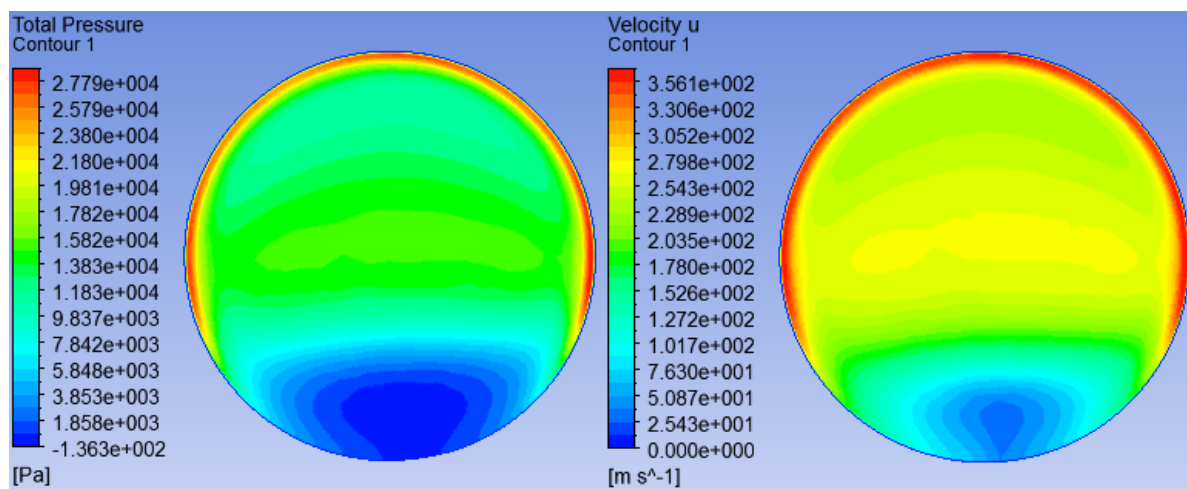


Figure E: Total Pressure and x-velocity contours at the AIP for the ParaPy model (PR=98.3% and DC₆₀=20.14%)

As shown in the previous figure, the results improved slightly. The pressure recovery obtained using CFX was 98.04%, which increased to 98.3% and the DC_{60} value for CFX was 20.55%, which reduced to 20.14%. The change in Mach number at AIP was not very significant ($M=0.539$). The ParaPy grid provides smoother curvature near the nacelle lip and hence allows for improved flow characteristics in this region. Because of this improvement, the pressure loss gets slightly reduced, which is why the pressure recovery value increases for the ParaPy model. In addition to this, the ParaPy grid provides more accuracy in the boundary layer region and is able to capture the boundary layer effect in higher detail (See Appendix G).

6.7 Results for Podded Inlet Configuration

Podded inlet configurations were tested in order to study and compare the results with the embedded inlet results and also to verify if BLI indeed makes sense. A number of podded inlets were tested with different geometrical variations. For a fair comparison, the idea was to determine a podded inlet area ratio that allows similar inlet mass flow rate and fan-face Mach number for the podded inlet as that of the embedded inlet. For the embedded inlet design shown in Figure 77 in Section 6.6.1, the inlet mass flow rate is 754.377 kg/s with an area ratio of 1.1 and a fan-face Mach number of 0.54. After a few tests, it was determined that an area ratio of 1.37 and a length of 6.46m for the podded case produces a similar mass flow rate (753.64 kg/s) and fan-face Mach number as that of embedded inlet. Similar contraction ratio was used for podded inlet (1.04) like the embedded case for internal nacelle lip construction and NACA 0012 airfoil was used to construct the external nacelle.

Hence a podded inlet configuration was created in CATIA with an area ratio of 1.37 and a length of 6.46m, with a pylon height of 0.8m above the fuselage surface to avoid any boundary layer being ingested. This is shown in Figure F.

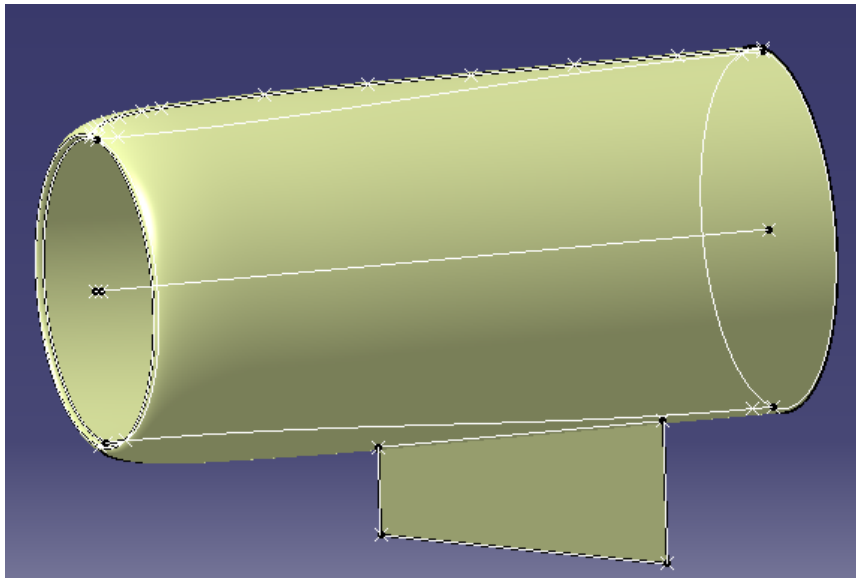


Figure F: Podded Inlet Configuration (L=6.46m, area-ratio = 1.37)

This model was meshed in ICEM CFD and solved in ANSYS CFX. The inlet Mach number for this case was 0.87. The results obtained from the analysis are shown in Figure G.

L=6.46m, Area-ratio=1.37, PR=90.2%, DC₆₀=2.6% approx., M at AIP=0.545

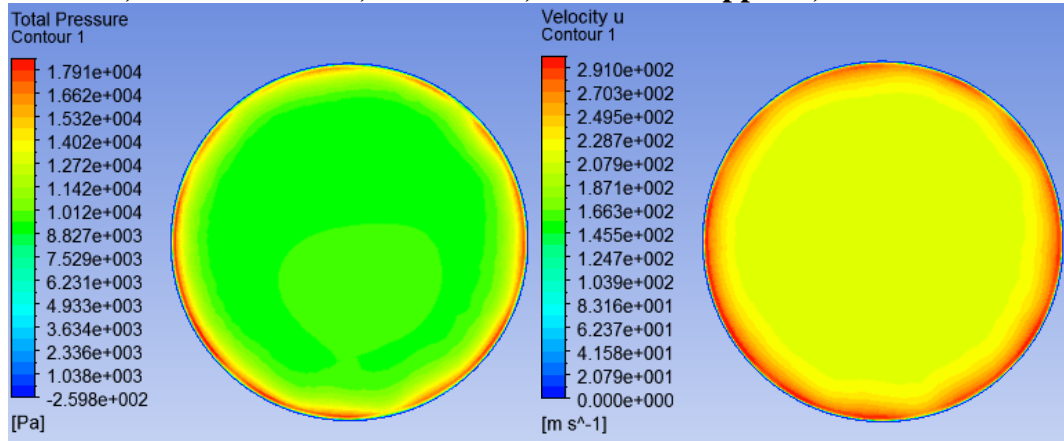


Figure G: Total Pressure and x-velocity contours at AIP for podded inlet with L=6.46m, area-ratio=1.37

Figure G shows that the DC₆₀ value improves significantly as expected, since the flow entering the podded inlet is mostly uniform. However, there is approximately a 10% loss in pressure recovery, which is still high. In addition to this, the wetted area for the podded inlet is 67.583 m² (as shown in Table 6), which is quite large and will cause larger drag than the embedded inlet.

These results show that for a similar inlet mass flow rate and fan-face Mach number, an embedded inlet produces more promising results in terms of pressure recovery and Mach number at the AIP. The podded inlet requires longer length to achieve the same fan-face Mach number as that of the embedded engine. However for the embedded inlet, the distortion needs to be lowered quite a bit.

Table 6 shows the results of the embedded and the podded inlets.

Configuration	Pressure Recovery (PR)	Distortion Coefficient (DC ₆₀)	Mach number at AIP (M)	Wetted Area
Embedded	98.3%	20.14%	0.54	44.067m ²
Podded	90.2%	2.6%	0.545	67.583m ²

6.8 Effect of BLI on Engine Performance

To understand the effect of BLI and compare it with a podded engine configuration, few simulations were carried out on a GE90 engine model using GSP (Gas Turbine Simulation software). The simulations produced some results which were used to understand the effect of BLI as compared to a podded engine on the engine efficiency.

3 major parameters were chosen for comparison:

- Specific Thrust
- Thrust Specific Fuel Consumption (TSFC)
- Ram Drag

a) Specific Thrust

Specific thrust is mathematically the ratio of thrust force and inlet mass flow rate and is given by equation (4.2):

$$\text{Specific Thrust} = \frac{F}{\dot{m}} \quad (4.2)$$

Here, F is the thrust force in Newton and \dot{m} is the inlet mass flow rate. Specific thrust is an indicator of engine efficiency. If we consider 2 engines with different values of specific thrust, then the engine with a higher value is more efficient. This is because the higher specific thrust engine produces more thrust for the same amount of airflow. Furthermore, a low specific thrust engine requires a larger engine diameter to net thrust it produces. Figure H shows the variation of Specific Thrust with varying inlet Mach number obtained from GSP simulation of a GE90 engine model.

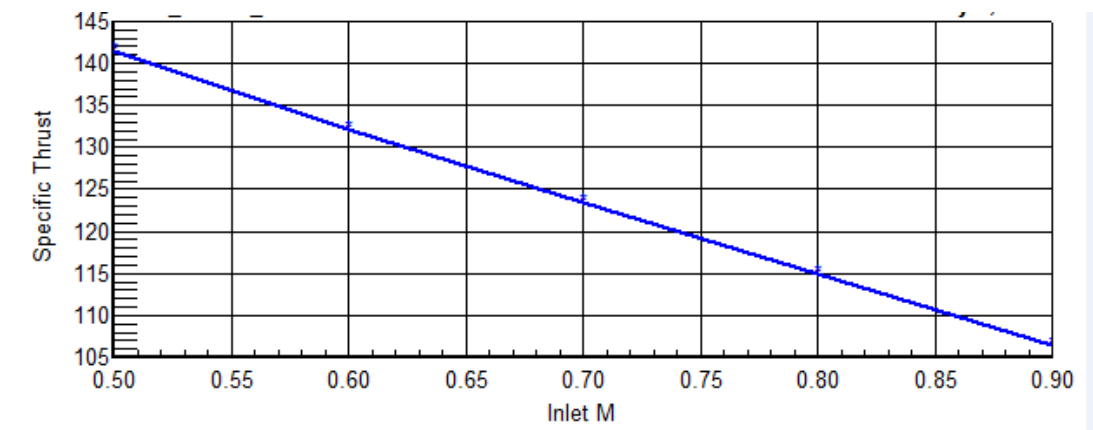


Figure H: Variation of Specific Thrust with inlet Mach number

From Figure H, it can be noticed that for the embedded engine (inlet $M=0.79$), the Specific Thrust value is higher (approx. 116 N-s/kg), whereas for the podded engine (inlet $M=0.87$), the Specific Thrust value is lower (approx. 109 N-s/kg). Therefore, the engine with BLI proves to be more efficient based on specific thrust since a BLI engine produces more thrust for the same mass flow.

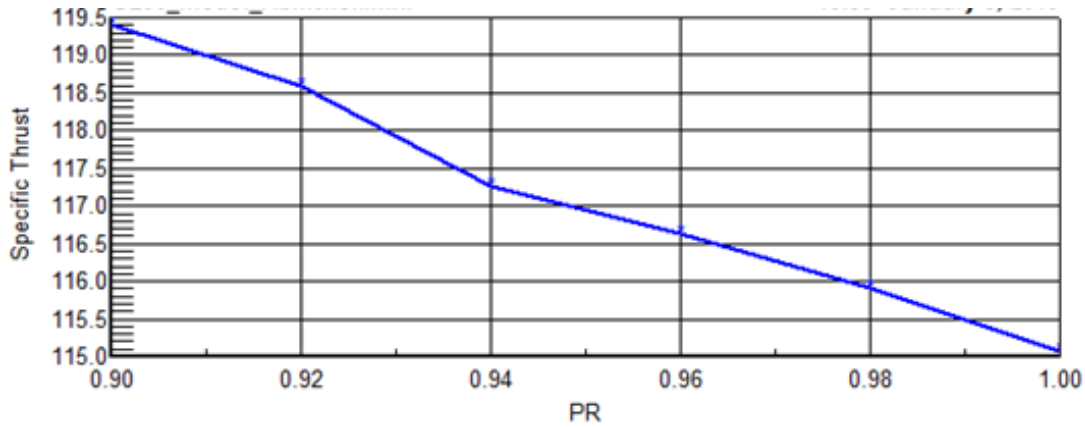


Figure I: Variation of Specific Thrust with pressure recovery for an embedded engine

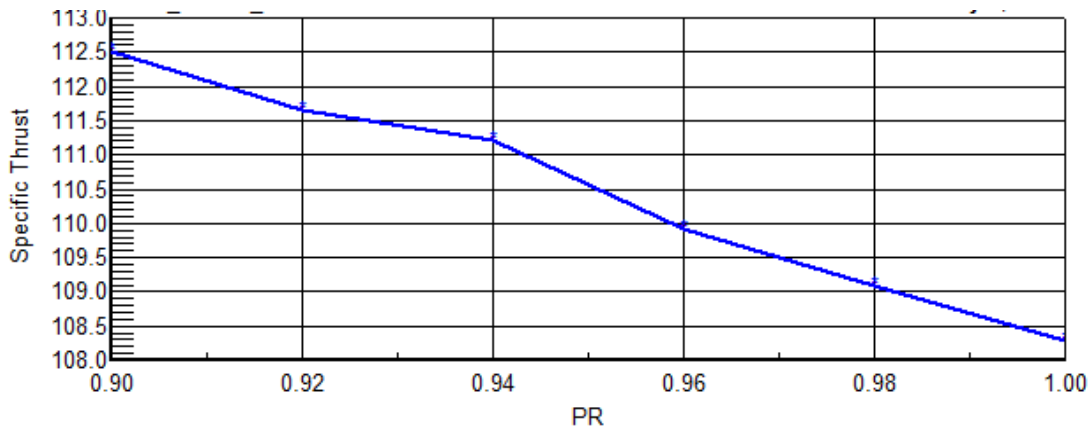


Figure J: Variation of Specific Thrust with pressure recovery for a podded engine

One of the drawbacks of BLI is high pressure loss due to secondary flows. However, the benefit of BLI can be observed from Figures I and J, which show that for an embedded engine, specific thrust is higher for the same value of pressure loss as compared to a podded engine. This is a direct indication of higher engine efficiency of a BLI engine.

b) Thrust Specific Fuel Consumption (TSFC)

Another parameter to measure the effect of BLI on engine performance is the TSFC. The fuel consumption of TSFC indicates how much fuel the engine burns each hour. Hence TSFC is an indicator of fuel efficiency of the engine. A low TSFC signifies high fuel efficiency and vice versa. This can also be seen through equation (4.3):

$$TSFC = \frac{\dot{m}_f}{F} \quad (4.3)$$

Here, \dot{m}_f is the fuel mass flow rate and F is the thrust force.

Figure K shows that for the embedded engine (inlet M=0.79), the TSFC (or 'sfc') is also low (approx. 15.5 g/kN-s). Whereas, for the podded engine (inlet M=0.87), the TSFC is slightly higher (approx. 16.5 g/kN-s). Even though the difference in TSFC between the embedded and podded engine is 1 g/kN-s, the embedded engine proves to be more fuel efficient based on the trend shown in Figure K that TSFC is increasing with increasing inlet Mach number. Since the inlet Mach number for an embedded engine is lower because of ingestion of slow

moving boundary layer, the TSFC is always lower as compared to a podded engine (with same mass flow rate and a uniform inlet velocity profile).

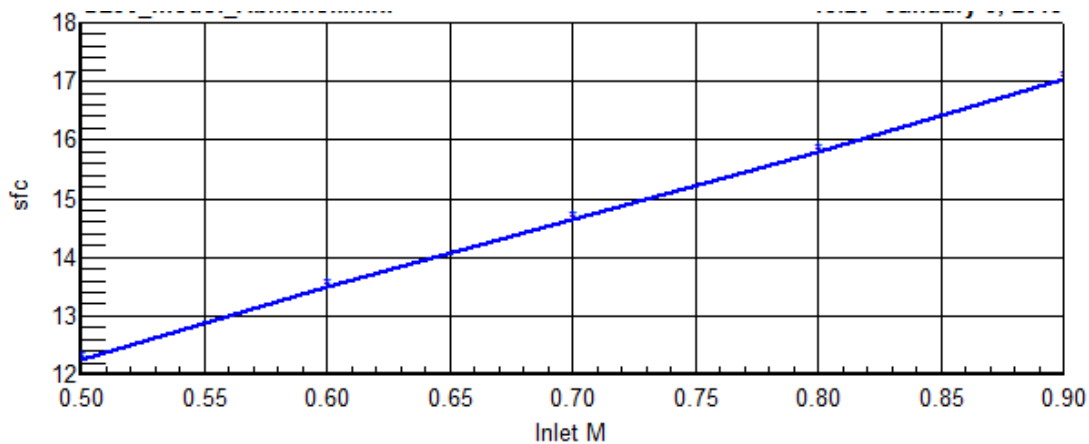


Figure K: Variation of TSFC with inlet Mach number

Based on pressure loss, it can be seen from Figures L and M that decreasing pressure loss decreases TSFC. However, the value of TSFC for a BLI engine is lesser for the same amount of pressure loss. Although the difference is small, but it shows that BLI achieves higher efficiency as compared to no-BLI for same pressure loss value.

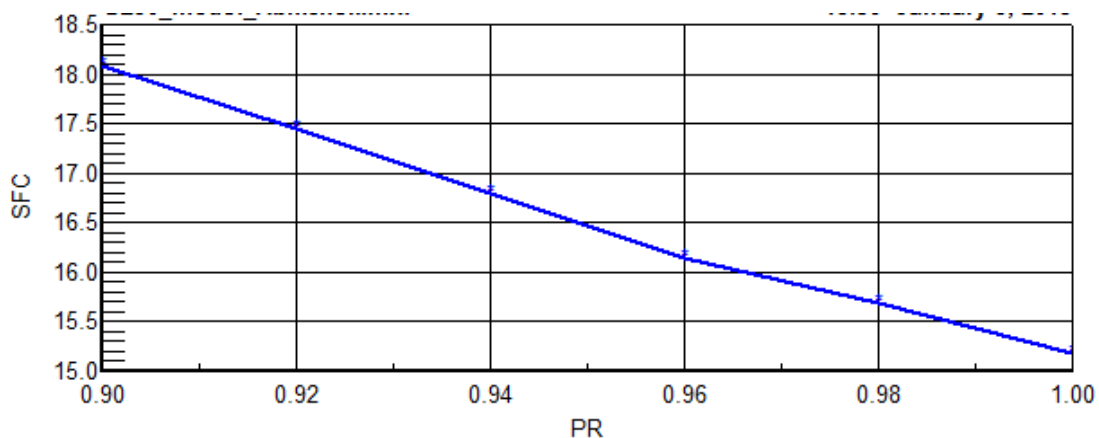


Figure L: Variation of TSFC with pressure recovery for an embedded engine

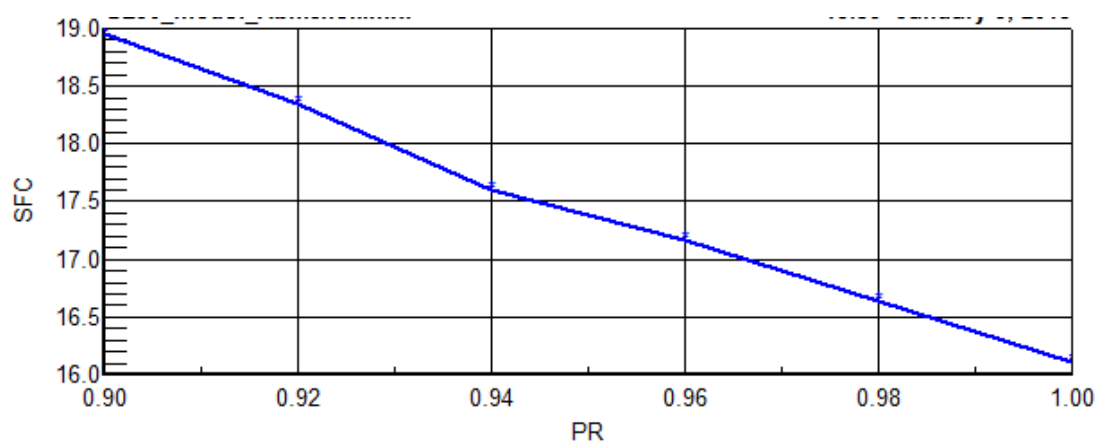


Figure M: Variation of TSFC with pressure recovery for a podded engine

c) *Ram Drag*

Ram drag is created due to the incoming free-stream flow in the inlet. It is mathematically the product of the inlet mass flow rate and the inlet velocity and is shown in equation (4.4). For embedded inlets, the inlet velocity is quite low as compared to the podded inlets, mainly due to the presence of a thick fuselage boundary layer, which is a low momentum flow. This low momentum boundary layer decreases the overall velocity at the entry of the inlet. In podded inlets however, the incoming flow is undisturbed uniform flow, which is higher in velocity.

$$\text{Ram Drag} = \dot{m}_0 V_\infty \quad (4.4)$$

Since ram drag is the product of mass flow rate and inlet velocity, for a similar mass flow rate for both podded and embedded inlets, an embedded inlet will produce a lower ram drag because of lower inlet velocity.

For the embedded engine, the inlet velocity in this thesis is 268.82 m/s ($M=0.79$) and for podded engine, the inlet velocity is 296.04 m/s ($M=0.87$). Since the mass flow rate is same in both cases (approx. 754 kg/s) for a valid comparison, the ram drag can be calculated using equation (4.4). The ram drag for the embedded engine is 202.69 kN and that for the podded engine is 223.214 kN. The podded engine produces a ram drag that is 20.52 kN more than that of the embedded engine. Hence BLI lowers ram drag and in turn increases fuel efficiency. This is because the engine has to burn lesser amount of fuel to produce the same amount of thrust. This is a direct benefit of BLI. A lower inlet velocity is also beneficial in terms of Mach number obtained at the fan. BLI inlets produce a much lower Mach number at the fan-face as compared to podded inlets. This was seen in Table 6, where the final design of the embedded inlet produced a fan Mach number of 0.54, whereas a podded inlet produced a fan Mach number of 0.66, which is detrimental to engine operability.

7

Conclusions and Recommendations

The main goal of the thesis was to understand the effects of Boundary Layer Ingestion (BLI) on the inlet performance on a Blended Wing Body (BWB) aircraft and obtain an inlet design that produces minimum total pressure distortion and maximum total pressure recovery at the Aerodynamic Interface Plane (AIP) or the engine fan-face. The thesis focussed on the internal duct performance of the inlet configurations tested for BLI. Past literature has shown that BLI has significant benefits in terms of wake recovery, fuel burnt and drag reduction. However, ingesting low momentum fuselage boundary causes losses inside the duct due to secondary flow formation, wall friction, etc., which results in increased distortion and reduced pressure recovery at the fan-face. Hence, an inlet design that effectively curtails these losses was required. Based on the geometrical parameterization of the duct, variations in the values of parameters like inlet aspect ratio, duct length, duct height, contraction ratio and nacelle lip major-to-minor axis ratio were chosen for testing different inlet configurations and understand their effects on the results.

7.1 BLI Effect on Inlet Performance

One of the major benefits of BLI is high wake recovery. In other words, ingesting larger portion of the airframe wake causes lesser wake dissipation as the ingested wake gets re-energized by the propulsor and converted into thrust. This means a high inlet aspect ratio is desired to ingest a larger percentage of boundary layer. However, too high an aspect ratio would cause high distortion at the fan-face. So, a balance between pressure recovery and distortion has to be met.

The results of the testing on different inlet aspect ratios showed that increasing the aspect ratio till $AR=1.75$ increased pressure recovery. For higher aspect ratios, the pressure recovery started to decrease. The inlet with $AR=1.75$ produced a pressure recovery value of 97.01% but a $DC(60)$ value of 41.59%, which was quite high for the engine to handle. The lowest $DC(60)$ value of approximately 33.48% was achieved by the inlet with $AR=1$ with a pressure recovery value of 96.28%. However, the mass averaged Mach number at the engine fan-face for the duct with $AR=1$ was 0.66, which is quite high. For $AR=1.75$, this value was 0.6. Furthermore, a higher value of aspect ratio produced lesser adverse pressure gradient on the upper wall of the duct due to smaller semi-major axis length of the inlet face (inlet wider and less high). Therefore, the inlet with $AR=1.75$ was chosen as the one with optimum aspect ratio value and selected for further testing.

7.2 Duct Height Effect on Inlet Performance

Duct height was defined as the vertical distance from center of the inlet face to center of the AIP. This meant increasing the duct height increased adverse pressure gradient for the bottom wall and favourable pressure gradient for the upper wall of the inlet. Results showed that increasing the duct height increased distortion at the AIP and decreased total pressure recovery. The inlet with the lowest duct height (0.3m) produced most optimum results with a pressure recovery value of 97.7% and a DC(60) value of 28.45%. Further investigation of other configurations was required to minimize the losses.

7.3 Duct Length Effect on Inlet Performance

Tests were conducted to find out the effect of increasing duct length on inlet performance. Increasing the length of the duct makes the flow more uniform inside the duct, however it causes pressure losses due to higher wetted area. It was noticed that increasing the duct length reduced the total pressure recovery value from 97.7% to 95.58%. It also increased the DC(60) value from 28.45% to 61.37% which is very significantly high and very unlikely for the engine to handle. Hence the inlet with the shortest length tested (4.85m) with PR=97.7% and DC(60)=28.45% was selected as the one with most optimal performance.

7.4 Effect of Other Configurations and Internal Nacelle Lip

Following the testing varying geometrical parameters, a conclusion on the aspect ratio, length and height was made (L=4.85m, AR=1.75, H=0.3m) with PR=97.7% and DC(60)=28.45%. So far, this inlet provided the best performance for an embedded engine on a BWB operating in transonic conditions. However, the results could be further improved, hence a number of other configurations of inlet were tested to understand their effects on inlet performance. Among all the configurations tested, the zero-gradient configuration (flat bottom wall) eradicated all separation regions and produced most optimum results with PR=98.04% and DC(60)=20.55%. This duct has a height of 1.615m, where the center of the fan face is vertically above the center of the inlet face. Length of duct is 4.85m and aspect ratio is 1.75. Even though the pressure recovery value obtained is quite high, the DC(60) value can be further reduced by the use of active or passive flow control techniques.

For the design of the internal nacelle lip, 3 different contraction ratio values were tested on the double-gradient duct geometry and a contraction ratio of 1.04 showed improvements in pressure recovery value (increased from 97.96% to 98.3%). This contraction ratio was also tested with the zero-gradient duct case (which is the most optimum duct configuration based on earlier parametric analysis). No major variations in pressure recovery or distortion was noticed with the added lip geometry for this inlet. Higher contraction ratios seemed to decrease pressure recovery values. Hence the final inlet design was obtained as the one with the following values for geometrical parameters: L=4.85m, AR=1.75, H=1.615m (flat bottom wall), CR=1.04, m/n=2. It produced a pressure recovery value of 98.04% and DC(60)=20.55%. The same model was also created using ParaPy and resulted in the following values: PR=98.3% and DC₆₀=20.14% and was chosen as the final design.

7.5 Podded Inlet Configuration

Podded inlets were also tested for comparison with the embedded case. Same mass flow rate (approx. 754 kg/s) and fan-face Mach number for both podded and embedded inlets were simulated. The results showed a pressure recovery value of 90.2% and DC_{60} value of 2.6% for the podded case. The wetted area for the podded case was also higher than that of the embedded case. The results indicated that for the same mass flow rate and AIP Mach number, the embedded inlet produced more promising results as compared to the podded inlet, however the distortion value is still significantly higher for the embedded inlet case.

7.6 Limitations and Future Scope

The research performed in this thesis shows the effects of BLI on inlet performance. It gives a detailed understanding of the effects of variations in geometrical parameters, other configurations and flow physics inside the inlet. However, there are certain limitations to the work carried out in the thesis (techniques used to evaluate the results and accuracy of the results).

Firstly, all of the CFD simulations were carried out using the RANS CFD package of ANSYS CFX. No studies were carried out to check the sensitivity of the solver algorithm in CFX. Some studies regarding error estimation can be conducted to verify the error range in the numerical results. Secondly, the validation of results in this thesis is based on the results of previous scientific studies carried out in the domain of BLI on a BWB in high subsonic conditions. For complete verification of the accuracy of results, a full 3D model of the BWB needs to be tested in a wind tunnel. This will help understand the magnitude of error between the CFD results and the experimental data. The current thesis does not focus on external nacelle design, so studies regarding design of the external nacelle and selection of appropriate airfoil for the cowl can be carried out based on full CFD analysis of the integrated engine on the BWB.

In addition to the requirement for sensitivity analysis and experimental studies, an investigation into the construction of the inlet geometries can further improve the results and make the total pressure and x-velocity contours at the AIP more symmetric about the vertical axis. The velocity profiles used as inlet for the ducts tested, were obtained from the CFD analysis of the BWB configuration. The velocity profiles chosen from aft fuselage locations were selected at locations with flattest boundary layer profiles in order to ingest as symmetric a boundary layer as possible. However, no studies have been performed to investigate the possible locations for engine integration on the fuselage. Follow-up studies regarding engine integration can be conducted, which will verify the accuracy of the ingested boundary layer topology.

Calculation of the distortion coefficient, DC_{60} , requires the values for area averaged total pressure on the entire fan-face, dynamic pressure over the entire fan-face and area averaged total pressure over the worst affected 60 degree sector on the fan face. The total pressure and dynamic pressure over the entire fan-face can be easily obtained from the post processor. However, area averaged pressure on the 60 degree sector cannot be calculated directly.

In this research, the worst affected 60 degree sector was usually at the bottom of the duct due to symmetry of contours about the vertical axis. To find out the area averaged pressure

at this sector, various lines were constructed in CFX-Post inside the sector and values of total pressures were calculated on these lines and then finally averaged to find P_{t60min} . This method is a very crude way of calculating P_{t60min} and may not produce accurate results. However, this research uses the DC_{60} values based on the explained method. An investigation into calculation of DC_{60} is required, possibly using coding in order to extract cell info from the post processor and writing a script to calculate exact value of P_{t60min} , which might differ from the values in this thesis.

Lastly, follow-up studies regarding effects of flow control on inlet performance can be carried out. Flow control has been shown to improve results significantly. It is therefore, important to investigate these effects. More number of different inlet configurations can also be tested, which might be better than the final design obtained in the current thesis work.

References

1. A.M. Ferrar and W.F. O'Brien, "*Progress in Boundary Layer Ingesting Embedded Engine Research*", 48th AIAA/ASME/SAE/ASEE, Joint Propulsion Conference and Exhibit, Georgia, USA, 2012.
2. P.N. Freuler, "*Boundary Layer Ingesting Inlet Design for a Silent Aircraft*", Master Thesis, Department of Aeronautics and Astronautics, Massachusetts Institute of Technology, Boston, USA, 2005.
3. L. Smith Jr., "*Wake Ingestion Propulsion Benefit*", AIAA/SAE/ASME/ASEE, 27th Joint Propulsion Conference, California, USA, 1991.
4. L.W. Hardin, G. Tillman and O.P. Sharma, "*Aircraft System Study of Boundary layer Ingesting Propulsion*", 48th AIAA/ASME/SAE/ASEE, Joint Propulsion Conference and Exhibit, Georgia, USA, 2012.
5. D.L. Daggett, R. Kawai and D. Friedman, "*Blended Wing Body System Studies: Boundary Layer Ingestion with Active Flow Control*", NASA Langley Research Center, vol. NASA/CR-2003-212670, Virginia, USA, 2003.
6. R.H. Liebeck, "*Design of the Blended Wing Body Subsonic Transport*", Journal of Aircraft, Vol. 41, No. 1, California, USA, 2004
7. S. Lemmens, "*A Feasibility Study on the Embedded Propulsion System with Boundary Layer Ingestion for the AeroCity*", Master thesis, Faculty of Aerospace Engineering, Delft University of Technology, Delft, The Netherlands, 2013.
8. A.P. Plas, M.A. Sargeant, V. Madani, D. Crichton, E.M. Greitzer and T.P. Hynes, "*Performance of a Boundary Layer Ingesting Propulsion System*", 45th AIAA Aerospace Sciences Meeting and Exhibit, Nevada, USA, 2007.
9. C.J. Hanlon, "*Engine Design Implications for a Blended Wing-Body Aircraft with Boundary Layer Ingestion*", Master Thesis, Department of Aeronautics and Astronautics, Massachusetts Institute of Technology, Boston, USA, 2003.
10. Q. Yang, Y. Zheng and T. Streit, "*Aerodynamic Design For Wing-Body Blended And Inlet*", 25th International Congress Of The Aeronautical Sciences, Hamburg, Germany, 2006.
11. A.J. Anabtawi, R. Blackwelder, R. Liebeck, P. Lissaman, "*Experimental Investigation of Boundary Layer Ingesting Diffusers of a Semi-Circular Cross Section*", 36th Aerospace Sciences Meeting and Exhibit, Nevada, USA, 1998.

12. K. Hunecke, “*Jet Engines; Fundamentals of Theory, Design and Operation*”, Motor Books International Publishers & Wholesalers, 2003.
13. L.R. Owens, B.G. Allan and S.A. Gorton,” *Boundary Layer Ingesting Inlet Flow Control*”, NASA Langley Research Center, Virginia, USA, 2006.
14. D.L. Rodriguez, “*A Multidisciplinary Design Optimization method For Designing Boundary Layer Ingesting Inlets*”, Phd. Thesis, Stanford University, Stanford, USA, 2001.
15. A.M. Ferrar, “*Measurements of Flow in Boundary Layer Ingesting Serpentine Inlets*”, Master Thesis, Faculty of The Virginia Polytechnic Institute and State University, Virginia, USA, 2011.
16. A.Rabe, S. Olcmen, J. Anderson, R. Burdisso and W. Ng, “*A Facility for Active Flow Control Research in Serpentine Inlets*”, 40th AIAA Aerospace Sciences Meeting & Exhibit, Nevada, USA, 2002.
17. B.L. Berrier and B.G. Allan, “*Experimental and Computational Evaluation of Flush-Mounted, S-Duct Inlets*”, 42nd AIAA Aerospace Sciences Meeting and Exhibit, Nevada, USA, 2004.
18. S.R. Wellborn, B.A. Reichert and T.H. Okiishi, “*An Experimental Investigation of the Flow in a Diffusing S-Duct*”, AIAA 27th Joint Propulsion Conference and Exhibit, USA, 1992.
19. S.E. Tournier, J.D. Paduano and D. Pagan, “*Flow Analysis and Control in a Transonic Inlet*”, Collection of Technical Papers, AIAA Applied Aerodynamics Conference, vol. 1, pp. 375-384, 2005.
20. S. Sun and K. Guo, “*Numerical Analysis and Experimental Validation of a Submerged Inlet on the Plane Surface*”, Chinese Journal of Aeronautics, vol. 18, no. 3, pp. 199-205, 2005.
21. B.G. Allan, L.R. Owens and B.L. Berrier, “*Numerical Modeling of Active Flow Control in a Boundary Layer Ingesting Offset Inlet*”, 2nd AIAA Flow Control Conference, AIAA-2004-2318, Oregon, USA, 2004.
22. B. H. Anderson, D. R. Reddy and K. Kapoor, “*A Comparative Study of Full Navier-Stokes and Reduced Navier-Stokes Analyses for Separating Flows Within a Diffusing Inlet S-Duct*”, 29th AIAA Joint Propulsion Conference and Exhibit, AIAA-93-2154, California, USA, 1993.
23. K.C. Weston, “*Energy Conversion*”, Pws Pub Co, 1992.

24. H.J.M. Kok, M. Voskuijl and M.J.L. van Tooren, “*Distributed Propulsion featuring Boundary Layer Ingestion Engines for the Blended Wing Body Subsonic Transport*”, 51st AIAA/ASME/ASCE/AHS/ASC Structures, Structural Dynamics and Materials Conference, Florida, USA, 2010.
25. A. Lundbladh and T. Grönstedt, “*Distributed Propulsion and Turbofan Scale Effects*”, 17th International Symposium on Air Breathing Engines, Munich, Germany, 2005.
26. S.A. Gorton, L.R. Owens, L.N. Jenkins, B.G. Allan and E.P. Schuster, “*Active Flow Control on a Boundary Layer Ingesting Inlet*”, 42nd AIAA Aerospace Sciences Meeting and Exhibit, Nevada, USA, 2004.
27. S. Klausmeyer, M. Papadakis and J. Lin, “*A Flow Physics Study of Vortex Generators on a Multi-Element Airfoil*”, AIAA Paper No.96-0548, 1996.
28. J.C. Lin, G.V. Shelby and E.G. Howard, “*Exploratory Study of Vortex-Generating Devices for Turbulent Flow Separation Control*”, AIAA Paper No.91-0042, 1991.
29. W.R. Pauley and J.K. Eaton, “*Experimental Study of the Development of Longitudinal Vortex Pairs Embedded in a Turbulent Boundary Layer*”, AIAA Journal, vol.26, No.7, pp.816-823, 1988.
30. B.J. Wendt, I. Breber and W. Hingst, “*The Structure and Development of Streamwise Vortex Arrays Embedded in a Turbulent Boundary Layer*”, AIAA Paper No.92-0551, 1992.
31. B.S. Stratford, “*The Prediction of Separation of the Turbulent Boundary Layer*”, Journal of Fluid Dynamics, vol .5, 1959.
32. B.J. Lee and M.S. Liou, “*Re-Design of Boundary-Layer-Ingesting Offset Inlet via Passive Flow Control*”, 48th AIAA Aerospace Sciences Meeting Including the New Horizons Forum and Aerospace Exposition, Florida, USA, 2010.
33. A.N. Gissen, B. Vukasinovic, M.L. McMillan and A. Glezer, “*Dynamics of Hybrid Flow Control in a Boundary-Layer-Ingesting Offset Diffuser*”, 41st AIAA Fluid Dynamics Conference And Exhibit, Hawaii, USA, 2011.
34. G. Godard and M. Stanislas, “*Control of a decelerating boundary layer. Part 1: Optimization of passive vortex generators*”, Aerospace Science and Technology vol. 10, Pg 181-191. 2006.
35. A.N. Gissen, B. Vukasinovic, M.L. McMillan and A. Glezer, “*Distortion Management in a BLI Inlet Diffuser using Synthetic-Jet Hybrid Flow Control*”, 49th AIAA Aerospace Sciences Meeting Including the New Horizons Forum and Aerospace Exposition, Florida, USA, 2011.

- 36.** V.M. Lugo, G. Doulgeris and R. Singh, “*Computational Analysis of the Effects of a Boundary Layer Ingesting Propulsion System in Transonic Flow*”, Proceedings of the Institution of Mechanical Engineers, Part G: Journal of Aerospace Engineering, UK, 2013.
- 37.** M.B. Carter, R.L. Campbell and O.C. Pendergraft Jr, “*Designing and Testing a Blended Wing Body with Boundary-Layer Ingestion Nacelles*”, Journal of Aircraft, vol. 43, No. 5, 2006.
- 38.** H. D. Ceron-Muñoz and F. M. Catalano, “*Aerodynamic Interference Of Power-Plant System On A Blended Wing Body*”, 27th International Congress of the Aeronautical Sciences, Nice, France, 2010.
- 39.** B.L. Berrier, M.B. Carter and B.G. Allan, “*High Reynolds Number Investigation of a Flush-Mounted, S-Duct Inlet With Large Amounts of Boundary Layer Ingestion*”, NASA Langley Research Center, Virginia, USA, 2005.
- 40.** H.D. Kim and J.L. Felder, “*Control Volume Analysis of Boundary Layer Ingesting Propulsion Systems With or Without Shock Wave Ahead of the Inlet*”, NASA Glenn Research Center, Ohio, USA, 2011.
- 41.** O. Atinault, G. Carrier, R. Grenon, C. Verbecke and P. Viscat, “*Numerical and Experimental Aerodynamic Investigations of Boundary Layer Ingestion for Improving Propulsion Efficiency of Future Air Transport*”, 31st AIAA Applied Aerodynamics Conference, California, USA, 2013.
- 42.** A.A. Elmiligui, W.J. Fredericks, M.D. Guynn and R.L. Campbell, “*Numerical Investigation of a Fuselage Boundary Layer Ingestion Propulsion Concept*”, AIAA Aviation Technology, Integration, and Operations Conference, California, USA, 2013.
- 43.** B.C. Johnson, R.S. Webster and K. Sreenivas, “*A Numerical Investigation of S-Duct Flows with Boundary-Layer Ingestion*”, 48th AIAA Aerospace Sciences Meeting Including the New Horizons Forum and Aerospace Exposition, Florida, USA, 2010.
- 44.** G. Behfarshad and S. Mahlou, “*Wind-Tunnel Study of a S-Shaped Air-Intake Performance*”, Aircraft Engineering and Aerospace Technology, Vol. 86 Iss: 2, pp.99 – 107, 2014.
- 45.** D. Reijnen, “*Design of Engine Inlet with S-Duct at $M_{cr}=0.50$ for J15D-1*”, Delft University of Technology, Delft, The Netherlands, 1992.
- 46.** F. Papadopoulos, I. Valakos and I.K. Nikolos, “*Design of an S-Duct Intake for UAV Applications*”, Aircraft Engineering and Aerospace Technology, Vol. 84, Greece, 2012.

- 47.** A. Bakker, “*Lecture 7 – Meshing - Applied Computational Fluid Dynamics (ANSYS)*”, <http://www.bakker.org/dartmouth06/engs150/07-mesh.pdf>, January 2002.
- 48.** R.J. Re and W.K. Abeyounis, “*A Wind Tunnel Investigation of 3 NACA-1 Series Inlets at Mach Numbers Up to 0.92*”, NASA Technical Memorandum 110300, Langley Research Center, National Aeronautics and Space Administration, Virginia, USA, November 1996.
- 49.** B.H. Anderson, H.D. Baust and J. Agrell, “*Management of Total Pressure Recovery, Distortion and High Cycle Fatigue in Compact Air Vehicle Inlets*”, NASA/TM-2002-212000, NASA, December 2002.
- 50.** van Dijk, R.E.C., “*Tools and Methods for Next-Generation Knowledge-Based Engineering Systems*”, Unpublished Doctoral Dissertation, Delft University of Technology, Delft, The Netherlands, 2015 (to be published).

APPENDIX – A

Operating Conditions

The Blended Wing Body (BWB) aircraft in this research is considered to operate at cruise conditions at a transonic Mach number of 0.82. Table 6 represents the operating conditions that the BWB operates at in this research work. These conditions were essential input parameters in the CFX setup.

Table 7: Operating Conditions

Flight Regime	Cruise
Mach Number	0.82
Free-stream Velocity	279 m/s
Altitude	10000m (or 32808.4 ft approx.) above sea level
Density of Air	0.41 kg/m ³
Temperature of Air	223.15 K (or – 50 °C)
Air Pressure	0.2615 atm or 26496.49 Pa
Dynamic Viscosity of Air	0.0000147 Pa-s
Heat Transfer	None
Molar Mass of Air	29 kg/kmol

APPENDIX – B

Calculation of ‘a’ and ‘b’ for Aspect Ratio

After the calculation of area ratio was complete, inlet area for an area ratio of 1.1 was found to be 7.45 m². Based on this area the dimensions of the inlet semi-elliptical face needed to be calculated. As explained in Section 5.3.1 and shown in Fig 36, ‘a’ is the major axis length of the ellipse and ‘b’ is the semi-minor axis length. Figure 78 shows the semi-elliptical inlet face with dimensions.

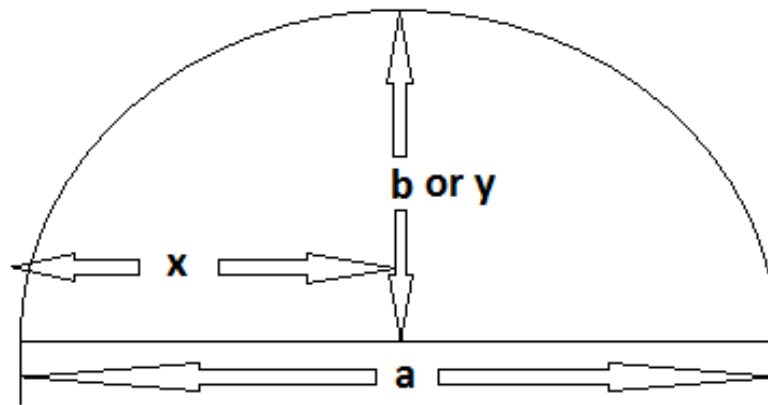


Figure 78: Semi-elliptical inlet face dimensions

The area of a semi-ellipse is given as:

$$A = \frac{1}{2} \pi xy$$

Here, ‘x’ is the semi-major axis length of the ellipse and ‘y’ is the semi-minor axis length of the ellipse. The area of the inlet is substituted on the left hand side of the equation shown above. On the right hand side, based on the aspect ratio desired, x and y is substituted accordingly. The following calculation shows an example of the calculation of ‘a’ and ‘b’ values for an aspect ratio of 1.75.

$$7.45 = \frac{1}{2} \pi xy$$

To get an aspect ratio of 1.75, $x=0.875y$

$$7.45 = \frac{1}{2} \pi \times 0.875 y \times y$$

Hence, **y = 2.328m and x = 2.037m**

Since x is the semi-major axis length and 'a' is the major axis length, 'a' will be twice the value of 'x'. Also, 'y' and 'b' are both semi-minor axis lengths.

Therefore, **a = 4.074m and b = 2.328m**

Similarly, values for 'a' and 'b' are calculated for all other aspect ratios.

APPENDIX – C

Separation Areas for Ducts with Varying AR and H

This appendix shows the figures containing the separation areas inside the S-Ducts for variations in aspect ratio and height. The similar figures for variation in length and other configurations are shown in Fig 69 and Fig 74 in Sections 6.4 and 6.5, respectively.

Figure 79 shows the separation region inside the S-Ducts with constant length (4.85m) and height (1.052m) and variation in inlet aspect ratio.

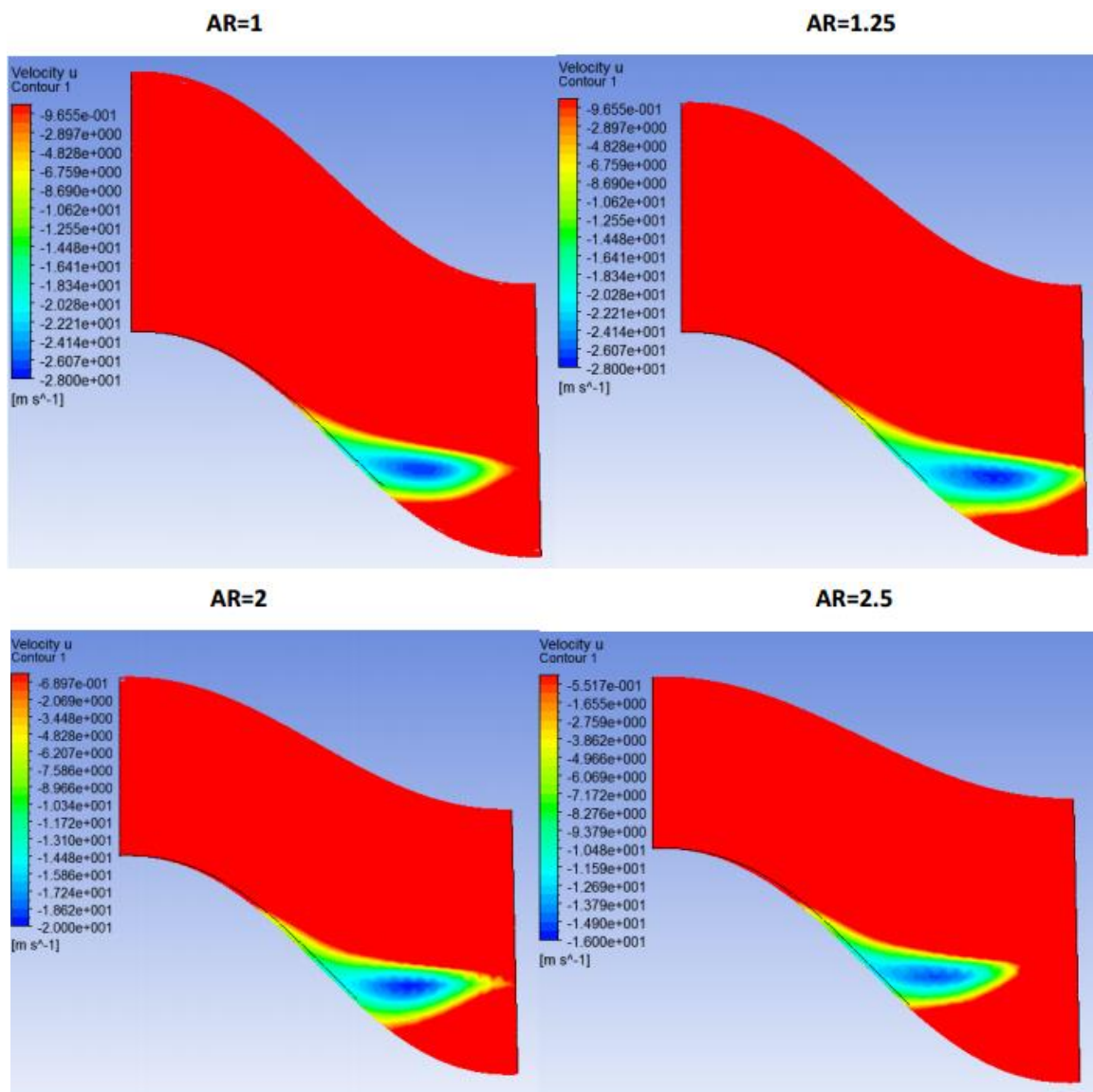


Figure 79: Separation areas inside S-Ducts with varying inlet aspect ratio

Figure 80 shows the separation region inside the S-Ducts with constant length (4.85m) and aspect ratio (1.75) and variation in duct height.

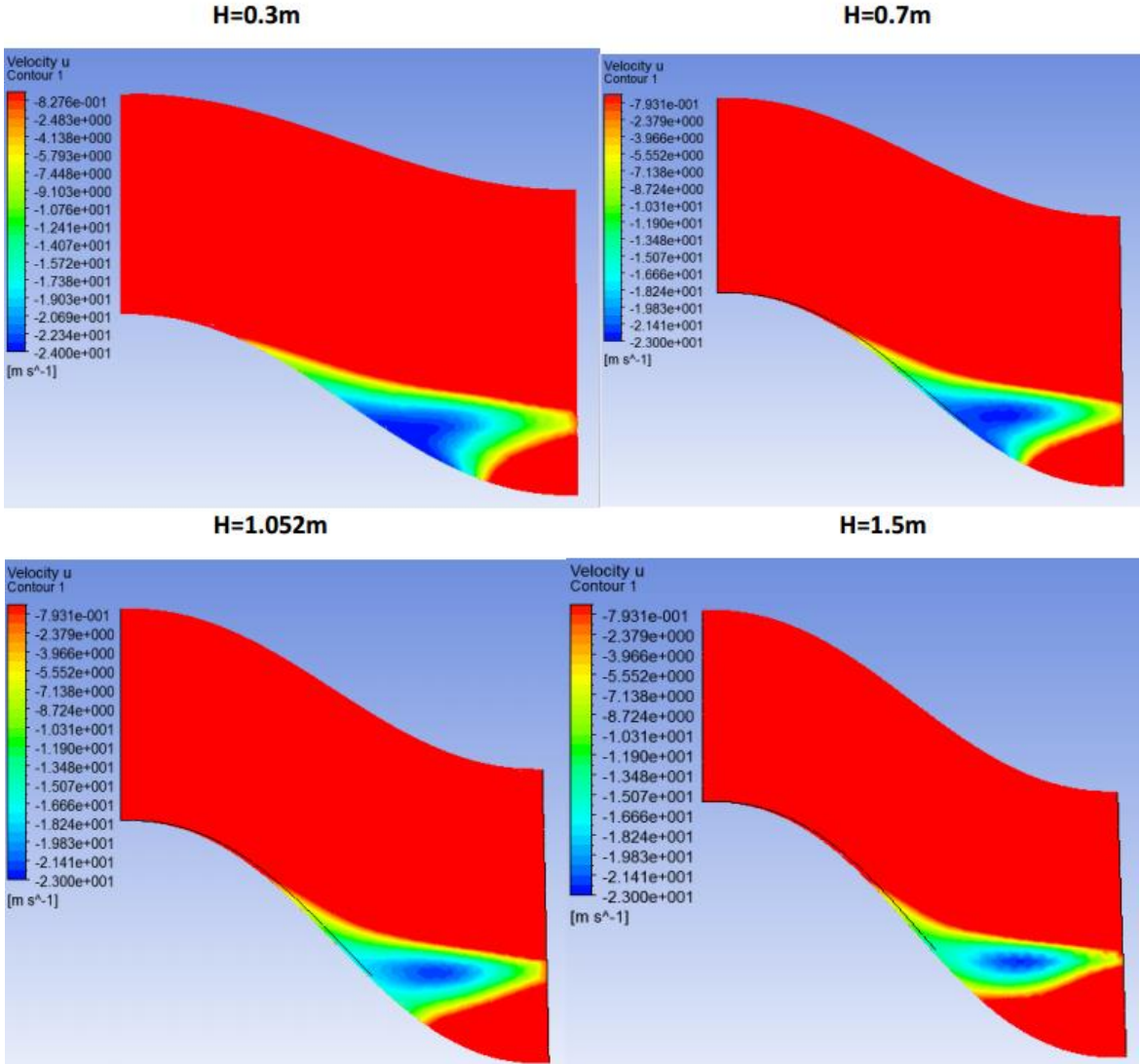


Figure 80: Separation areas inside S-Ducts with varying height

APPENDIX – D

Calculation of Distortion Coefficient

The calculation of the distortion coefficient, DC_{60} , requires the calculation of area-averaged total pressure over the entire fan face, the dynamic pressure over the entire fan face and the area-averaged total pressure over the worst affected 60 degree sector on the fan face (P_{t60min}). The formula for distortion coefficient and its description is shown in Figure 6 in Section 1.2.1. The calculation of the area-averaged total and dynamic pressures over the entire fan face can be easily obtained from post processing in FLUENT or CFX. So, the only parameter that requires calculation is P_{t60min} . Area-averaging essentially means the summation of the product of total pressures on each cell in the 60 degree sector and the corresponding cell area divided by the total area of the 60 degree sector.

It is not possible to export area of each cell in the 60 degree sector from CFX. Moreover, since the mesh is unstructured, if the 60 degree sector is created, some of the cells will lie on the boundary of the 60 degree sector not completely inside it. So, the values of the total pressure on these cells will be inaccurate. Some accurate ways to calculate P_{t60min} are meshing the geometry containing 60 degree sectors already created at the outlet or writing a script to evaluate the same. However, since majority of the tests were already complete by the time distortion calculation was required, the method of meshing again around 60 degree sectors was ruled out. Due to time constraints and the complexity of writing the script to evaluate P_{t60min} , this method was ruled out too.

At the end, a crude method of DC_{60} calculation was used. Since, the contours of total pressure are almost symmetric about the vertical axis on the outlet, the worst affected 60 degree sector was determined to be at the bottom of the outlet. This sector was created using line construction in CFX. A number of lines were constructed inside the 60 degree sector as this was possible in CFX. Then the total pressure were calculated on these lines and exported in .csv format to Excel. Then the average of these pressures was taken as P_{t60min} and DC_{60} was calculated from the formula shown in Figure 6 in Section 1.2.1. The 60 degree sector is shown in Fig 81.

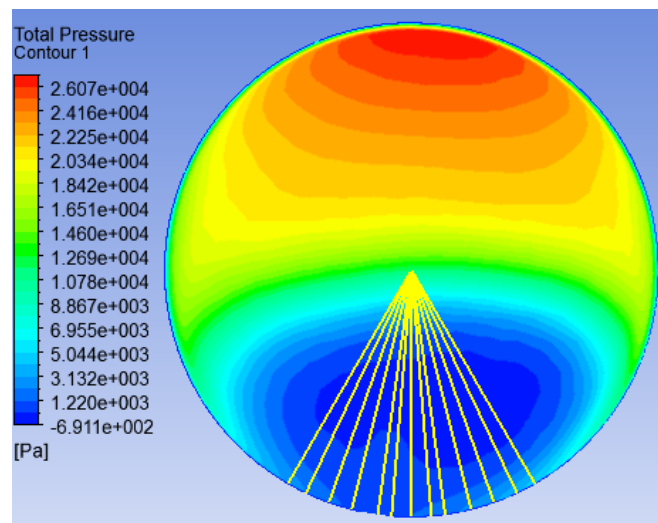


Figure 81: Total pressure contours and the 60 degree sector with lines at AIP

APPENDIX – E

General Modelling Approach

Figure 82 shows the general approach for modelling of a CFD case.

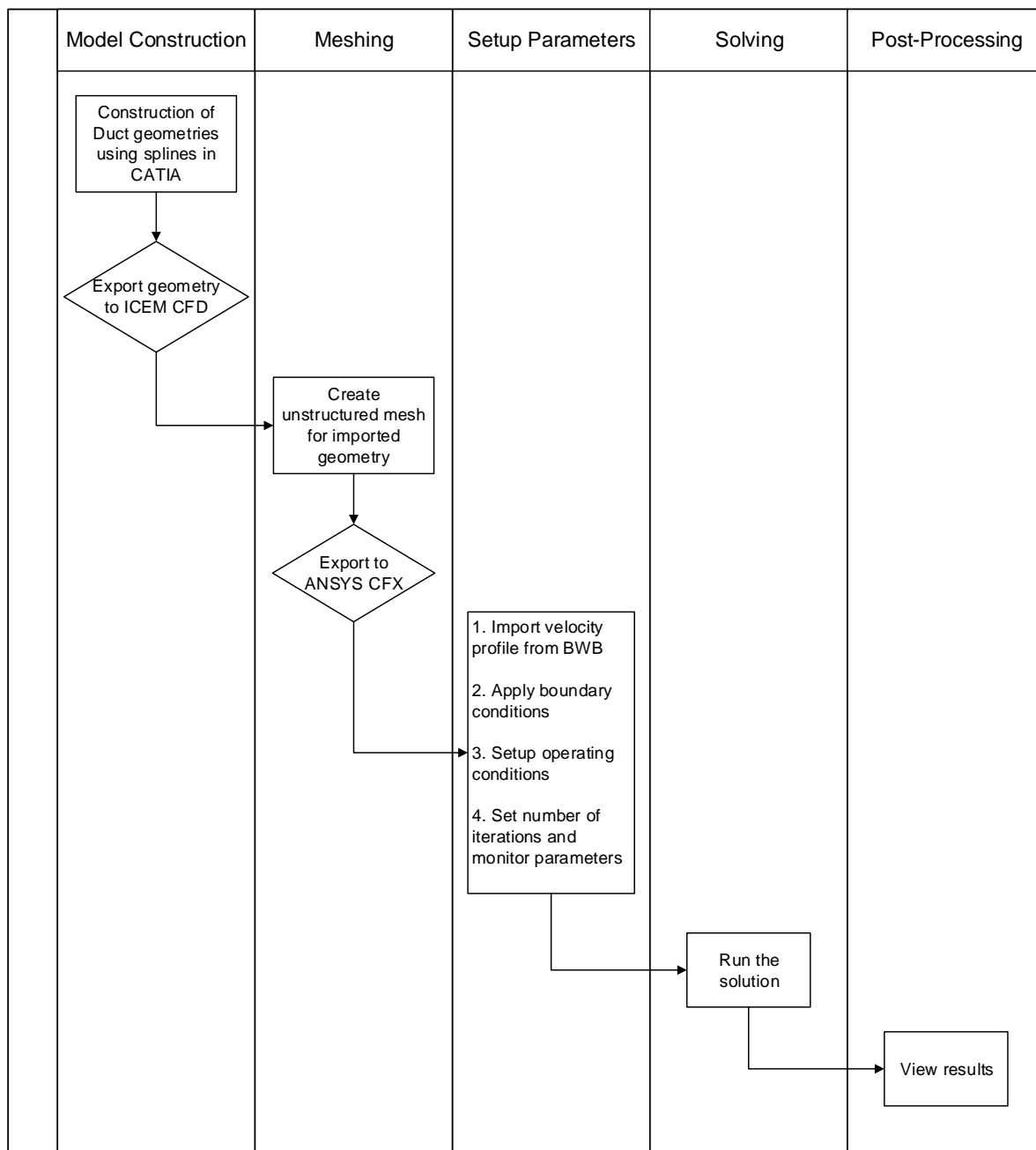


Figure 82: General approach for modelling of a CFD case

APPENDIX – F

ParaPy codes for S-Duct Geometry and Grid

General S-Duct Model

Effective Lines of Code (without annotation and blank lines): 81

```
001     from __future__ import division
002     from math import pi, radians
003     from parapy.core import * # @UnusedWildImport
004     from parapy.geom import * # @UnusedWildImport
005     from parapy.exchange import STEPWriter
006     from apps.sduct.mesh import SDuctMesh
007
008
009     class SDuct(GeomBase):
010
011
012         # Inputs
013
014         L = Input(4850, "length of the duct")
015         H = Input(300, "the height measured between center points of start and end profile")
016         angle1 = Input(180, "The top angle of the first cross section.")
017         angle2 = Input(270, "The top angle of the second cross section. Cannot be < 180.",
018                       validator = val.Range(180, float("inf"), min_incl=True))
019         minor_radius = Input(4074/2, "semi-minor axis of inlet (horizontal)")
020         major_radius = Input(2328, "semi-major axis of inlet (vertical)")
021         diameter = Input(3230, "diameter of outlet")
022
023
024         # Attributes
025
026         @Attribute
027         def ellipse_inverted(self):
028             return self.major_radius < self.minor_radius
029
030         @Attribute
031         def ellipse_limits(self):
032             angle = radians(self.angle1)
033             u1 = 0 if self.ellipse_inverted else 0.5*pi
034             limit1 = u1-(angle-pi)/2
035             limit2 = limit1 + angle
036             return [limit1, limit2]
037
038         @Attribute
039         def circle_limits(self):
040             angle = radians(self.angle2)
041             u1 = 0 if self.ellipse_inverted else 0.5*pi
042             limit1 = u1-(angle-pi)/2
043             limit2 = limit1 + angle
044             return [limit1, limit2, limit1]
045
046         @Attribute
047         def orientation_sections(self):
048             if self.ellipse_inverted:
049                 return Orientation(Vector(0,0,1), Vector(0,1,0))
050             else:
051                 return Orientation(Vector(0,-1,0), Vector(0,0,1))
052
053
```

```

054 #-----
055 # Basic skeleton of curves
#-----
056 @Part
057 def path(self):
058     return InterpolatedCurve([self.position, self.position(x=self.L, y=-self.H)],
059                             initial_tangent=Vector(0.1, 0, 0),
060                             final_tangent=Vector(0.1, 0, 0))
061
062 @Part
063 def ellipse(self):
064     return Ellipse(self.minor_radius if self.ellipse_inverted else self.major_radius,
065                  self.major_radius if self.ellipse_inverted else self.minor_radius,
066                  position=Position(self.center, self.orientation_sections))
067
068 @Part
069 def circle(self):
070     return Circle(self.diameter/2,
071                  position=self.position(x=self.L, y=-self.H).rotate_to(self.orientation_sections))
072
073 #-----
074 # Trimming the cross sections and making splines
075 #-----
076 @Part
077 def ellipse_trim(self):
078     return TrimmedCurve(self.ellipse, self.ellipse_limits[0], self.ellipse_limits[1])
079
080 @Part
081 def ellipse_line(self):
082     return LineSegment(self.ellipse_trim.end, self.ellipse_trim.start, color="RED")
083
084 @Part
085 def circle_trim1(self):
086     return TrimmedCurve(self.circle, self.circle_limits[0], self.circle_limits[1])
087
088 @Part
089 def circle_trim2(self):
090     return TrimmedCurve(self.circle, self.circle_limits[1], self.circle_limits[2])
091
092 #-----
093 # building the cross-sections and sweep
094 #-----
095 @Part
096 def section1(self):
097     return Wire([self.ellipse_trim, self.ellipse_line])
098
099 @Part
100 def section2(self):
101     return Wire([self.circle_trim1, self.circle_trim2])
102
103 @Part
104 def solid(self):
105     return MultiSectionSolid(self.path, [self.section1, self.section2])
106
107 #-----
108 # Capability modules
109 #-----
110 @Part
111 def salome(self):
112     return Salome(shape_to_mesh=self.solid, inlet=self.solid.bottom_face, outlet=self.solid.top_face)
113
114 @Part
115 def step_writer(self):
116     return STEPWriter(nodes=self.solid,
117                      default_directory=full_path("output"),
118                      filename=full_path("output/sduct.step"))

```

General S-Duct Mesh Model

Effective Lines of Code (without annotation and blank lines): 53

```
001     from parapy.core import * # @UnusedWildImport
002     from parapy.mesh import Controls, FaceGroups
003     from parapy.mesh.salome import Mesh, TriSimple, Tri, TetraViscous
004
005
006     class SDuctMesh(Base):
007
008         shape_to_mesh = Input()
009         inlet = Input()
010         outlet = Input()
011
012         @Attribute
013         def walls(self):
014             return list(set(self.shape_to_mesh.faces)-set([self.inlet, self.outlet]))
015
016         @Part
017         def controls(self):
018             return SDuctMeshControls()
019
020         @Part
021         def groups(self):
022             return FaceGroups({"inlet": {"shape": self.inlet,
023                                     "color": "green"},
024                               "outlet": {"shape": self.outlet,
025                                       "color": "red"},
026                               "walls": {"shape": self.walls,
027                                       "color": "blue"}})
028
029         @Part
030         def writer(self):
031             return Mesh(pass_down="controls, groups",
032                       default_directory=full_path("output"),
033                       filename=full_path("output/mesh.unv"))
034
035
036     class SDuctMeshControls(Controls):
037
038         local_length = Input(60, "length of edge segments")
039         y1 = Input(1, "length of initial boundary layer element")
040         g = Input(1.2, "growth rate of boundary layer elements")
041         N = Input(17, "number of BL layer elements")
042         fineness = Input("Fine")
043
044         @Attribute
045         def t_BL(self):
046             a, g, N = self.y1, self.g, self.N
047             return a * (g**N - 1) / (g - 1)
048
049         #=====
050         # Hypotheses
051         #=====
052         @Part
053         def faces_walls(self):
054             return TriSimple(shape=self.parent.walls,
055                             local_length = self.local_length,
056                             only_2d=False)
057
058         @Part
059         def faces_inlet_outlet(self):
060             return Tri(shape=[self.parent.inlet, self.parent.outlet],
061                       fineness = self.fineness)
062
063         @Part
064         def volume(self):
065             return TetraViscous(faces_to_include=self.parent.walls,
066                                t = self.t_BL,
067                                no_layers = self.N,
068                                stretch_factor = self.g,
069                                fineness = self.fineness)
```


APPENDIX – G

Mesh Quality Comparison: ParaPy and ICEM CFD

Mesh quality depends on a number of factors. 3 most important and relevant factors in this case are:

- Orthogonality
- Aspect Ratio
- Minimum angle

1. Quality assessment based on “Orthogonality”

The ParaPy grid was loaded into ICEM CFD to obtain the values for the factors that determine mesh quality. Various sources of available literature on CFD provide acceptable range of values, which determine the quality of a mesh to be ‘good’ or ‘bad’. The first of these factors is the orthogonality. In ICEM CFD, the measure of orthogonality is the dihedral angle. This angle should generally be greater than a minimum of 10 degrees and less than a maximum of 170 degrees. Figures 83 and 84 show the histograms obtained from ICEM CFD that display the range of dihedral angles on the x-axis and the number of elements on the y-axis for ParaPy grid and ICEM grid, respectively.

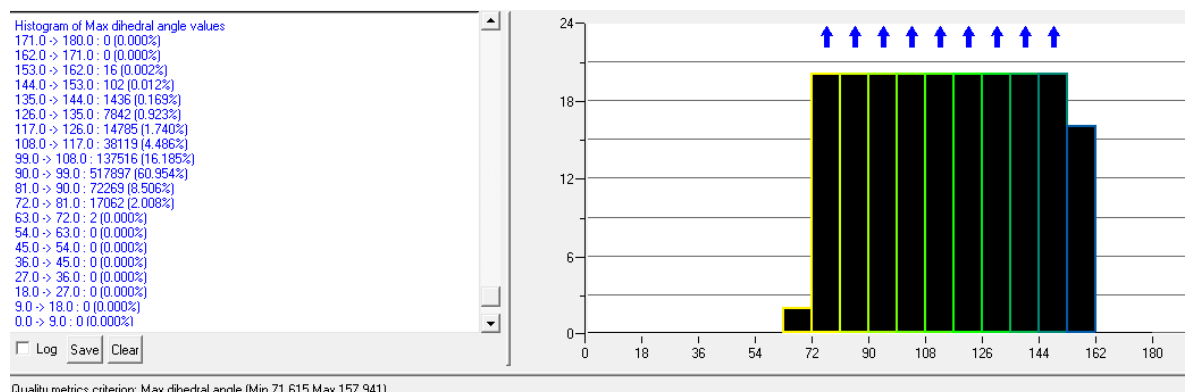


Figure 83: Histogram showing max dihedral angle values for ParaPy Grid

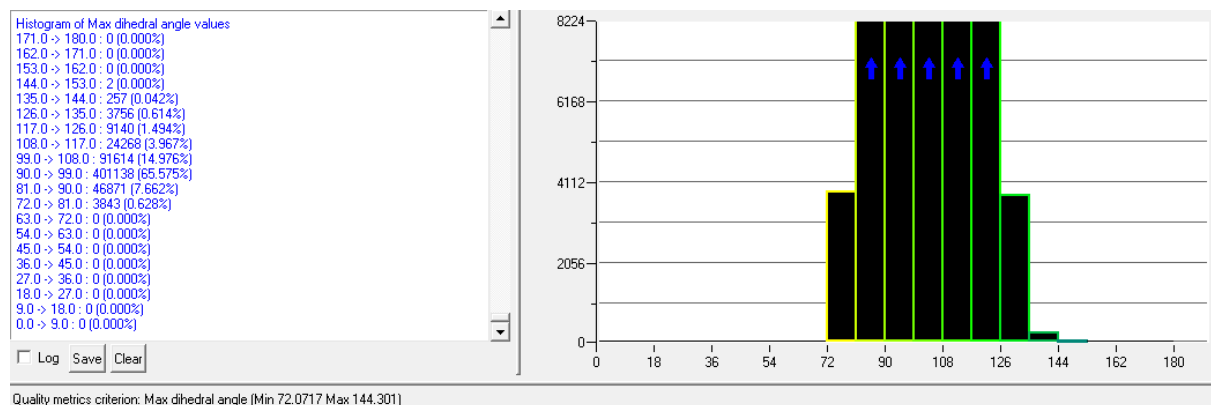


Figure 84: Histogram showing max dihedral angle values for ICEM Grid

It can be seen from Figures 83 and 84 that the mesh quality based on orthogonality is similar for both the grids. The minimum angle for the ParaPy grid is 71.615 degrees and for the ICEM grid is 72.071 degrees. The maximum angle for the ParaPy grid is 157.941 degrees and for the ICEM grid is 144.301 degrees. Hence, based on orthogonality, the mesh quality is similar for both the meshes, although maximum dihedral angle is a little better for the ICEM grid since it is much less closer to the upper limit 170 degrees as mentioned before.

2. Quality assessment based on “Aspect Ratio”

The acceptable range of values for the aspect ratio suggests aspect ratio < 100. Figures 85 and 86 show the aspect ratio values on the x-axis and the number of elements on the y-axis for ParaPy and ICEM grids, respectively.

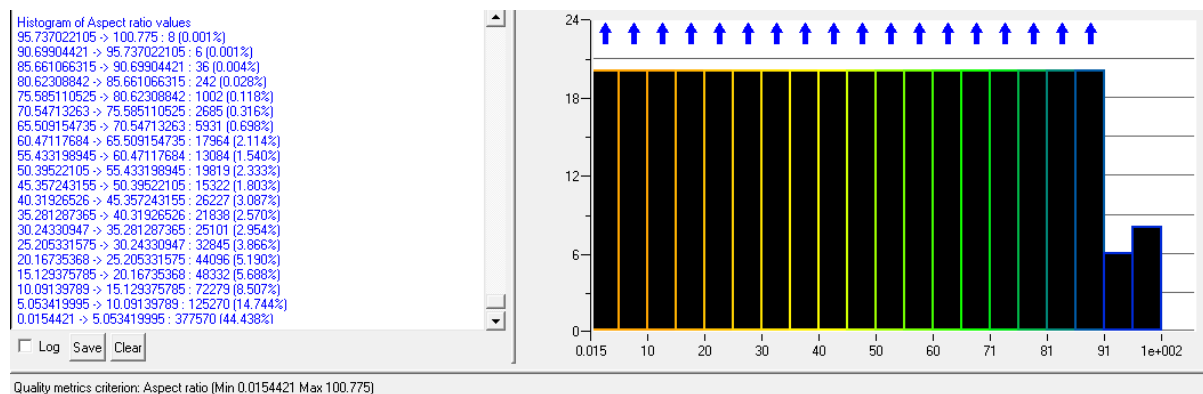


Figure 85: Histogram showing aspect ratio values for ParaPy Grid

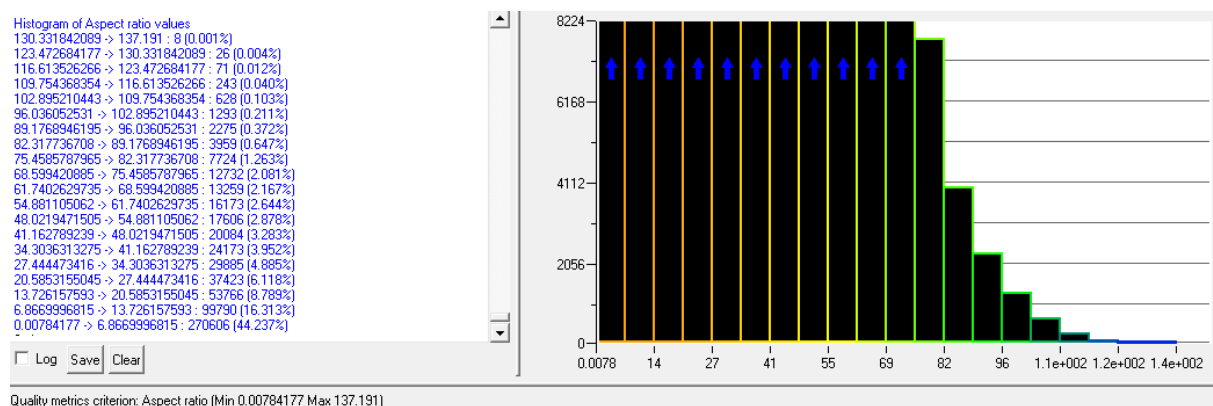


Figure 86: Histogram showing aspect ratio values for ICEM Grid

It is evident from Figure 85 that the maximum aspect ratio value for the ParaPy grid reaches up to a value of 100.775, whereas for the ICEM grid, this value reaches 137.191. Based on aspect ratio, the ICEM grid shows poor mesh quality as compared to the ParaPy grid. Hence, ParaPy grid clearly has a better mesh quality in terms of aspect ratio.

3. Quality assessment based on “Minimum angle”

The angle between the adjacent elements is found by determining the internal angle deviation from 90 degrees for each element as shown in Figure 87. If elements are distorted and internal angles are small, the accuracy of the solution will decrease.

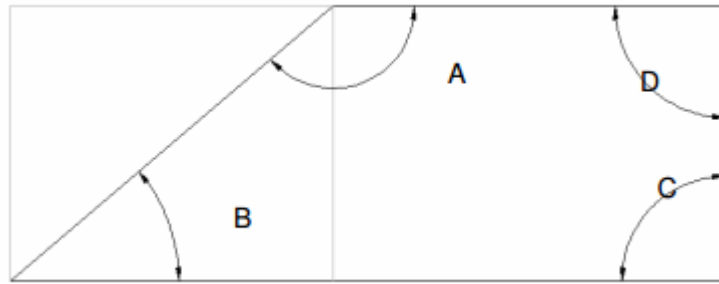


Figure 87: Minimum angle determination

For an acceptable mesh quality, the minimum angle value should be preferably greater than 18 degrees (definitely greater than 9 degrees).

Figures 88 and 89 show the minimum angle values on the x-axis and the number of elements on the y-axis for ParaPy and ICEM grids, respectively.

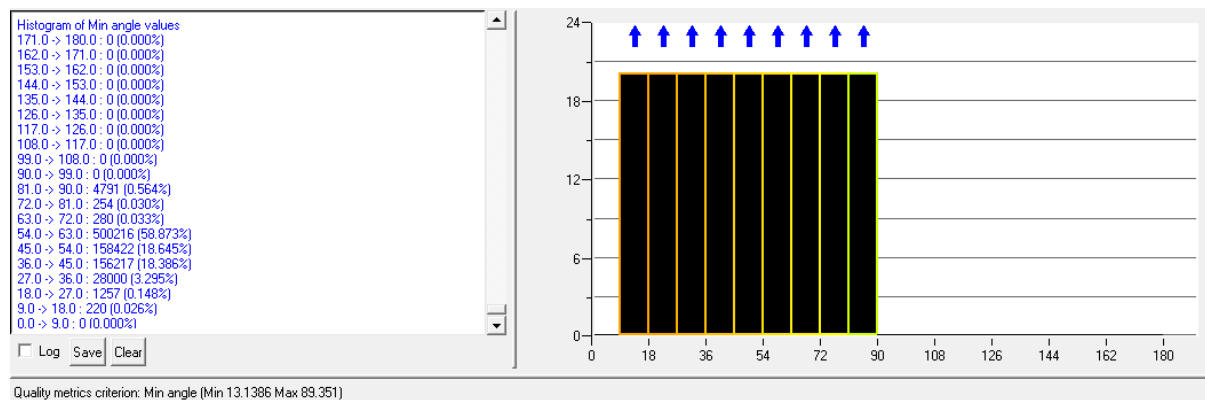


Figure 88: Histogram showing minimum angle values for ParaPy Grid

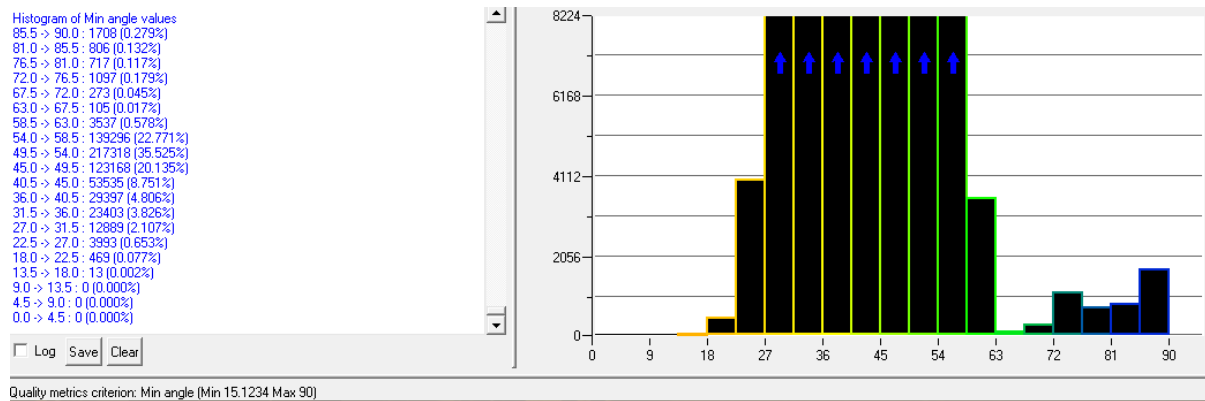


Figure 89: Histogram showing minimum angle values for ICEM Grid

It can be seen from Figures 88 and 89 that the minimum angle for the ParaPy grid is 13.138 degrees, whereas for the ICEM grid, the minimum angle is 15.123 degrees. The maximum angles are similar in both cases (89.35 degrees for ParaPy and 90 degrees for ICEM). It is evident that the ICEM grid shows somewhat better mesh quality in terms of minimum angle requirement (preferable above 18 degrees) since its value is closer to 18 degrees. However, the difference is not that significant. The distribution of angles is more uniform in the ParaPy grid.

4. Prism thickness and other details about ICEM grid

The ICEM mesh was created with 17 prism layers, an exponential growth law with growth factor of 1.2 and an initial wall spacing of 1 mm. Figures 90 and 91 show the distribution of “prism thickness” for ParaPy and ICEM grid, respectively. It can be noticed that the maximum prism thickness for the ICEM grid reaches a value of 0.036m, however the number of elements in this category are very few. Whereas for the ParaPy grid, a maximum prism thickness of 0.026m exists.

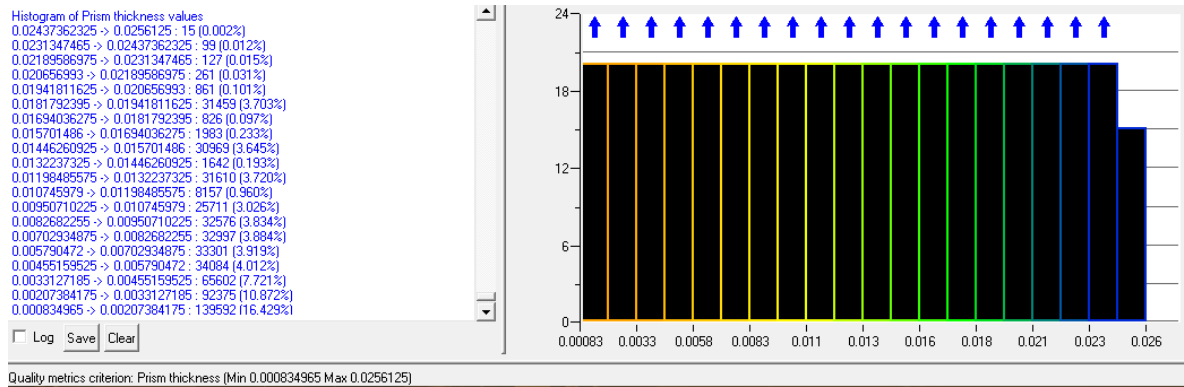


Figure 90: Prism thickness distribution for ParaPy grid

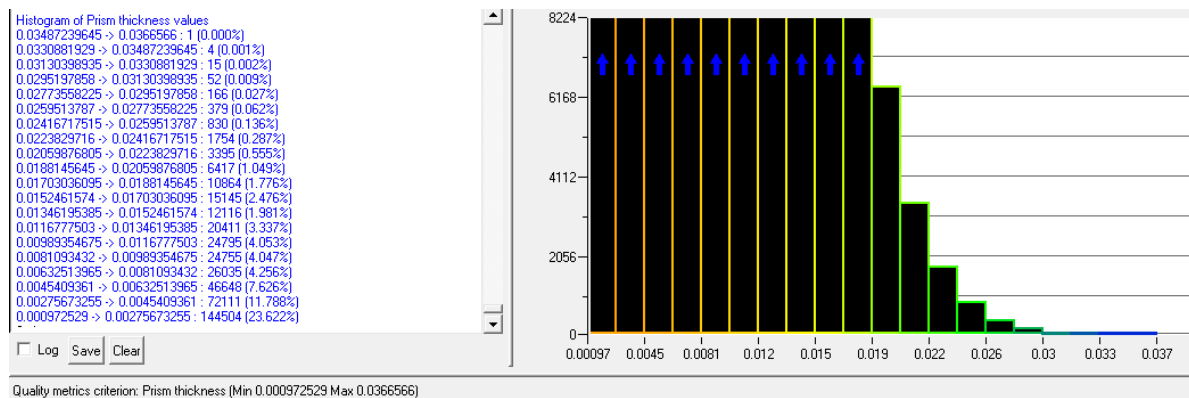


Figure 91: Prism thickness distribution for ICEM grid

The ParaPy grid allows more uniform distribution of prism thickness in the layers as compared to the ICEM grid, which also has some elements in the 0.03m prism thickness value. However again, the number of elements in this region are very less.

Figures 92 and 93 show the y-plus coverage on the walls for the ParaPy grid and the ICEM grid, respectively.

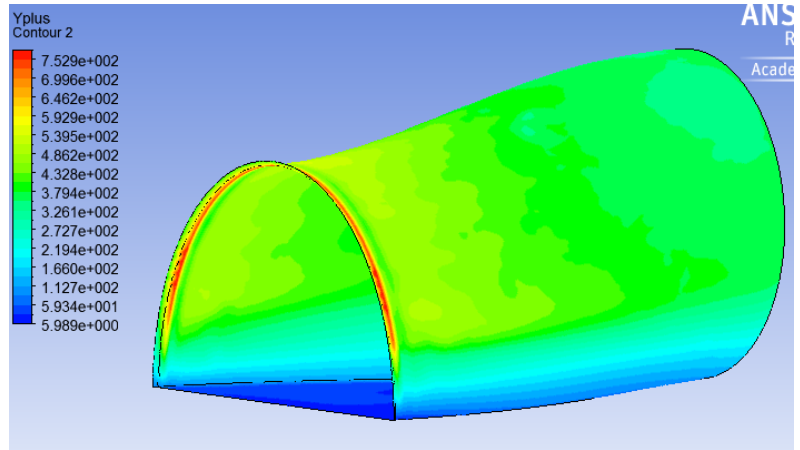


Figure 92: y-plus distribution on the walls (ParaPy)

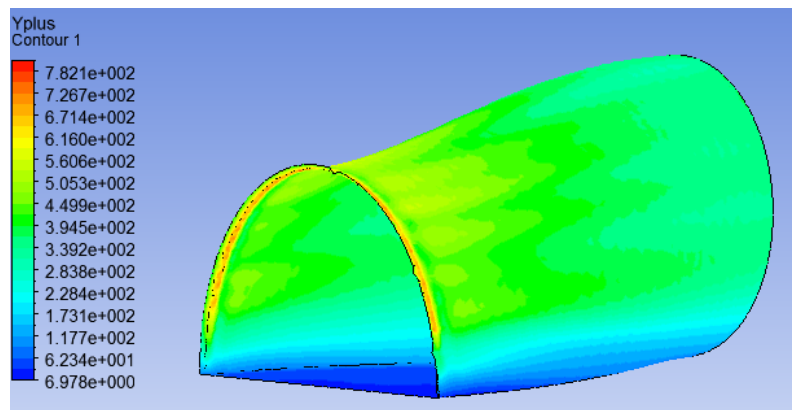


Figure 93: y-plus distribution on the walls (ICEM)